Spatial mapping of the hepatocellular carcinoma landscape identifies unique intratumoural perivascular-immune neighbourhoods

Felix Marsh-Wakefield[†1,2], Cositha Santhakumar[†1,2,3], Angela L. Ferguson[†1,2], Thomas M. Ashhurst[4,5], Joo-Shik Shin[6,7], Fiona H. X. Guan[3], Nicholas J. Shields[4], Barry J. Platt[2], Givanna H. Putri[8], Ruta Gupta[6,7], Michael Crawford[9], Carlo Pulitano[9,10], Charbel Sandroussi[9,10], Jerome M. Laurence[9,10], Ken Liu[1,3,4], Geoffrey W. McCaughan[‡1,3,4], Umaimainthan Palendira[‡2]

[†/‡]Authors contributed equally

[1]Liver Injury & Cancer Program, Centenary Institute

[2]Human Immunology Laboratory, School of Medical Sciences, Faculty of Medicine and Health, The University of Sydney

[3]A.W. Morrow Gastroenterology and Liver Centre, Royal Prince Alfred Hospital

[4]School of Medical Sciences, Faculty of Medicine and Health, The University of Sydney

[5]Sydney Cytometry Core Research Facility, The University of Sydney

[6]Central Clinical School, Sydney Medical School, The University of Sydney

[7]Department of Tissue Pathology and Diagnostic Oncology, Royal Prince Alfred Hospital, NSW Health Pathology

[8]The Walter and Eliza Hall Institute of Medical Research and The Department of Medical Biology, The University of Melbourne, Australia

[9]Australian National Liver Transplant Unit, Royal Prince Alfred Hospital

[10]Royal Prince Alfred Institute of Academic Surgery, University of Sydney

Author contributions

Felix Marsh-Wakefield, Cositha Santhakumar, and Angela L. Ferguson contributed substantially to the conception and design of the paper; acquisition of data; analysis and interpretation of data; drafting and revising the paper extensively and critically for important intellectual content. Thomas M. Ashhurst and Givanna H. Putri contributed substantially to the analysis and interpretation of data; revising the paper critically for important intellectual content. Joo-Shik Shin, Fiona H. X. Guan, Nicholas J. Shields, Barry J. Platt, Ruta Gupta,

Michael Crawford, Carlo Pulitano, Charbel Sandroussi, and Jerome M. Laurence contributed substantially to acquisition of data; revising the paper critically for important intellectual content. Ken Liu contributed substantially to the conception and design of the paper; interpretation of data; revising the paper extensively and critically for important intellectual content. Geoffrey W. McCaughan and Umaimainthan Palendira contributed substantially to the conception and design of the paper; interpretation of data; drafting and revising the paper extensively and critically for important intellectual content. All authors provided final approval of the version to be published.

Address of correspondence

Felix Marsh-Wakefield

f.marsh-wakefield@centenary.org.au

Centenary Institute, Camperdown 2050, NSW, Australia

Financial support and sponsorship

This work was funded by the Joan Krefft bequest to the A.W. Morrow Gastroenterology and Liver Centre (Royal Prince Alfred Hospital) and Cancer Institute NSW (2021/ATRG2028). Felix Marsh-Wakefield is supported by the International Society for the Advancement of Cytometry (ISAC) Marylou Ingram Scholars Program. Cositha Santhakumar is supported by the Sydney Cancer Partners PhD scholarship.

Conflicts of interest

Nothing to report.

Keywords

Tumour immunology

Spatial proteomics

Imaging mass cytometry

Human liver cancer

Perivascular macrophages

Highlights

- Imaging mass cytometry using 39 markers was used to map immune-infiltrating cells in hepatocellular carcinoma (HCC)
- Perivascular macrophages (PVM) were seen to form unique intratumoural neighbourhoods with immune cells
- PVM were identified as $VEGFA^{+}$ within HCC tumours

List of abbreviations

FFPE	Formalin-fixed paraffin embedded
H&E	Haematoxylin and eosin
HCC	Hepatocellular carcinoma
IHC	Immunohistochemistry
IMC	Imaging mass cytometry
LSEC	Liver sinusoidal endothelial cell
MAIT cells	mucosal-associated invariant T cells
mIHC	Multiplex immunohistochemistry
MRS	myeloid response score
MVI	Microvascular invasion
PCA	Principal component analysis
PERMANOVA	Permutational multivariate analysis of variance
PVM	perivascular macrophage

ROI	Region of interest
RT	Room temperature
scRNA-seq	Single-cell RNA-sequencing
sPLS-DA	Sparse partial least squares-discriminant analysis
TAM	tumour-associated macrophage
TGF-β	transforming growth factor-beta
TIL	Tumour-infiltrating lymphocyte
TMA	Tissue microarray
TME	Tumour immune microenvironment
TNM	Tumour-node-metastasis
TSA	Tyramide signalling amplification
VEGFA	Vascular endothelial growth factor A

Data availability

Data are available on Zenodo (DOI 10.5281/zenodo.10547481).

Abstract

Background & Aims: Hepatocellular carcinoma (HCC) develops in the context of chronic inflammation, however, the opposing roles the immune system plays in both the development and control of tumours is not fully understood. Mapping immune cell interactions across the distinct tissue regions could provide greater insight into the role individual immune populations have within tumours.

Methods: A 39-parameter imaging mass cytometry panel was optimised with markers targeting immune cells, stromal cells, endothelial cells, hepatocytes, and tumour cells. We mapped the immune landscape of tumour, invasive margin, and adjacent non-tumour regions across sixteen resected tumours comprising of 144 regions of interest. X-shift clustering and manual gating were used to characterise cell subsets, and Spectre quantified the spatial environment to identify cellular neighbourhoods. Ligand-receptor communication was quantified on two single-cell RNA-sequencing datasets and one spatial transcriptomic dataset.

Results: We show immune cell densities remain largely consistent across these three regions, except for subsets of monocyte-derived macrophages which are enriched within the tumours. Mapping cellular interactions across these regions in an unbiased manner identifies immune neighbourhoods comprised of tissue-resident T cells, dendritic cells, and various macrophage populations around perivascular spaces. Importantly, we identify multiple immune cells within these neighbourhoods interacting with VEGFA^{+} perivascular macrophages. *VEGFA* was further identified as a ligand for communication between perivascular macrophages and CD34^{+} endothelial cells.

Conclusions: Immune cell neighbourhood interactions, but not cell densities, differ between intratumoural and adjacent non-tumour regions in HCC. Unique intratumoural immune neighbourhoods around the perivascular space points to an altered landscape within tumours. Enrichment of VEGFA^{+} perivascular macrophages within these tumours could play a key role in angiogenesis and vascular permeability.

Impact and Implications

We investigated the landscape of immune cells within liver cancer. A unique perivascular neighbourhood of immune cells was identified. This is important as the interaction of immune cells and the vasculature in liver cancer is a therapeutic target of current systemic therapy. The

128 characterisation in detail of this neighbourhood may potentially identify additional targets for
129 future therapies.

130

131 **Introduction**

132 Liver cancer is the sixth most incident cancer and the third leading cause of cancer-related
133 death in the world [1] with hepatocellular carcinoma (HCC) accounting for approximately 90 %
134 of cases [2]. The five-year overall survival of HCC after diagnosis is approximately 20 % and
135 this statistic has not changed significantly over the past decade despite advancements in
136 treatment options [3]. This poor prognosis is attributable to its phenotypic and genetic
137 heterogeneity, its occurrence in patients with reduced liver reserve (cirrhosis), high rates of
138 tumour recurrence following curative treatments, and its predisposition to metastasise in
139 advanced stages [4]. Although immunotherapy has recently revolutionised the treatment of
140 advanced-stage disease in other malignancies such as melanoma and lung cancer, objective
141 response rates to systemic combination therapies in advanced HCC have been suboptimal (less
142 than 30 %) [5-7].

143

144 Being the prototypical cancer of inflammatory origin, immune responses in HCC are
145 implicated in both pro- and anti-tumoural activities [8]. Understanding the complex interplay
146 between immune cells and the tumour environment is therefore critical. Recent studies using
147 single-cell approaches have identified the diverse phenotype of immune cells within HCC
148 tumours and provided some insight into their possible functional roles [9]. However, several of
149 these single-cell methodologies lack spatial context, therefore limiting our ability to determine
150 the potential impact that specific cellular interactions have on clinical outcomes. Spatially
151 resolving these cellular interactions could provide greater insight into how various immune
152 populations contribute to tumour development, progression, and control.

153

154 Angiogenesis is also a key feature of HCC, wherein hypervascularisation and leaky vessels
155 pose challenges to the cellular immune control of tumours and influences responses to various
156 therapies [10-12]. Amongst many angiogenic factors, vascular endothelial growth factor A
157 (VEGFA) has been identified as the key driver of neovascularisation in HCC, with tumour cells
158 largely implicated in its production [13,14]. The importance of angiogenesis (and its interplay with

159 the tumour immune microenvironment, TME) is evident by recent data showing that
160 combination bevacizumab (anti-VEGFA) and atezolizumab (anti-PD-L1) antibodies improved
161 survival in patients with advanced unresectable HCC [5]. Interestingly, this strategy has been
162 found to have a synergistic effect [15,16].

163

164 HCC tumour cells are a well-known source of VEGFA [13,17], yet several immune cells have
165 been identified as alternate sources of VEGFA. *VEGFA*$^{+}$ mast cells are thought to be pro-
166 tumour across several cancer types, although they are largely absent in HCC [18]. In contrast,
167 high levels of *FOLR2*$^{+}$ macrophages, *PLVAP*$^{+}$ endothelial cells, and Notch/VEGF signalling
168 are associated with an immunosuppressive niche within HCC tumours [19].

169

170 High-dimensional imaging mass cytometry (IMC) has previously been utilised to investigate
171 the tumour microenvironment in HCC across several contexts, including hepatitis B virus
172 infection [20], response to immunotherapies [21], and macrophage characterisation [22]. The latter
173 study is important as several studies have implicated macrophages in HCC, including
174 neighbourhood interactions associated with immune cell activation [23,24] and response to
175 immunotherapies [21]. However, more work is needed to better understand the role of immune
176 cells – particularly macrophages – in angiogenesis and vascular permeability in HCC.

177

178 In this study, we interrogated the tumour and adjacent non-tumour immune microenvironment
179 in patients with resectable HCC using a high-dimensional tissue imaging platform known as
180 IMC. We spatially resolved cellular interactions in these regions to identify immune
181 neighbourhoods in intratumoural perivascular spaces that comprised of liver-resident CD4^{+}
182 and CD8^{+} T cells, dendritic cells, and phenotypically diverse macrophages. Importantly, we
183 showed enrichment of VEGFA^{+} perivascular macrophages (PVMs) within the tumour regions
184 that interact with these immune aggregates in the perivascular space that was absent in adjacent
185 non-tumour regions, suggesting these immune neighbourhoods could be important in the
186 development and/or progression of HCC.

187

188 **Methods**

189 **Patients**

190 Institutional human research ethics was obtained by the Sydney Local Health District Ethics
191 Review Committee (HREC 2020/ETH02093). Research was conducted in accordance with
192 both the Declarations of Helsinki and Istanbul, with written consent given in writing by all
193 subjects. Treatment naïve patients undergoing curative resection for HCC from 2019 until 2021
194 at a single tertiary institution were identified from the Royal Prince Alfred Liver Biobank.
195 Inclusion criteria was based on the availability of liver tissue (frozen or paraffin embedded)
196 from adult (>18 years old) males and females with HCC diagnosis. Patients also required
197 availability of clinical, imaging, and histopathology data. The formalin-fixed paraffin
198 embedded (FFPE) tissues were retrieved from the Department of Tissue Pathology and
199 Diagnostic Oncology and Royal Prince Alfred Hospital. Relevant clinicopathological data was
200 obtained from electronic medical records. Clinicopathological data included age, sex, aetiology
201 of liver disease, presence of cirrhosis, presence of microvascular invasion (MVI), and largest
202 tumour size. Of the sixteen HCC patients, two have since begun treatment with immune
203 checkpoint inhibitors, and one is now part of a placebo-controlled trial. Whole specimens of
204 HCC tissues from an additional eight patients were used to assess the intratumoural spatial
205 relationship of PVMs and endothelial cells. Further details are provided in Supplementary
206 Table 1.

207

208 **Tissue Microarray Preparation**

209 The haematoxylin and eosin (H&E) stained sections from the sixteen patients were reviewed
210 by a liver pathologist. One region of interest (ROI) was selected from the tumour, invasive
211 margin, and non-tumour regions. The tumour ROI was selected based on the high abundance
212 of tumour-infiltrating lymphocytes (TILs) on H&E stained sections. The invasive margin was
213 defined at the border of the malignant tumour and consisted of approximately 50 % malignant
214 and 50 % non-malignant tissue. The non-tumour region was selected away from the tumour.
215 The exact distance between the non-tumour and tumour was variable across patient samples
216 with no fixed diameter. In many patient samples, these areas were selected from different
217 blocks so we are unable to attain a fixed measurement for this distance. Three 1 mm diameter
218 (triplicate) cores were taken from each ROI for creation of the two tissue microarrays (TMAs)
219 (Figure 1A). Tonsils and hepatocellular adenoma were used as batch controls for the TMAs.

220 Both TMAs were sectioned at 7 µm onto charged slides. Figure 1 provides an overview of the
221 experimental design.

222

223 **Antibody Panel**

224 An antibody panel (Supplementary Table 2) was designed to identify various components of
225 the HCC TME and background liver tissue, including malignant and non-malignant
226 hepatocytes, immune cells, immune checkpoint inhibitors, cell signalling pathways, stromal
227 cells, and structural markers. Antibodies were selected based on clones previously validated in
228 our lab on human tissue [25]. Antibodies were then re-validated on FFPE liver and HCC tissue
229 (Supplementary Figure 1). Antibodies that were purchased unconjugated were all tested and
230 validated by conventional immunohistochemistry (IHC) prior to metal conjugation. Post-metal
231 conjugation antibodies were revalidated and titrated using IMC. Pre-conjugated antibodies
232 (Sydney Cytometry Reagent Bank) were tested and titrated for our tissue and staining
233 conditions prior to experimental use. Antibody-metal conjugations were done using the X8
234 Maxpar conjugation kit as per the manufacturer's protocol (Standard BioTools).

235

236 **Tissue staining for imaging mass cytometry**

237 TMA sections were baked at 60 °C for 60 minutes prior to deparaffinisation and rehydration.
238 Heat-induced antigen retrieval was performed by boiling the samples at 100 °C for 15 minutes
239 in pH 9.0 antigen retrieval buffer (10 mmol L^{-1} Tris base, 1 mmol L^{-1} EDTA, 0.05 % Tween
240 20, pH 9.0). The TMA slides were allowed to cool down to room temperature (RT) before
241 proceeding.

242 Sections were incubated with 3 % hydrogen peroxide prior to washing and blocking (Akoya
243 Biosciences, Antibody Diluent/Block). Slides were then stained with anti-CD69 (clone
244 EPR21814, Abcam) at RT before washing with TBS-T. Secondary OPAL-HRP (PerkinElmer)
245 was added to the slides at RT before washing in TBS-T. Slides were stained with TSA Plus
246 FITC (PerkinElmer) at RT before washing with TBS-T. Slides were microwave treated (as
247 described above) before letting them cool down to RT before proceeding.

248 Slides were then washed in TBS-T before blocking in blocking buffer (Akoya Biosciences) for
249 45 minutes at 37 °C. Slides were blocked with 20 % donkey serum (in DPBS) for 10 minutes

250 at RT. Slides were stained with anti-PD-L1 (clone E1L3N, CST) and anti-CK8/18 (clone 5D3,
251 Leica) for 45 minutes at RT before washing in TBS-T. Slides were then stained with Cy3 anti-
252 rabbit (711-166-152, Jackson ImmunoResearch Laboratories) for PD-L1 and Cy5 anti-mouse
253 (715-606-150, Jackson ImmunoResearch Laboratories) for CK8/18. Slides were washed in
254 TBS-T and DPBS. Slides were avidin/biotin blocked (Life Technologies). Slides were then
255 stained in anti-Foxp3 biotin (clone 236A/E7, eBioscience) before washing in TBS-T. TMA
256 sections were incubated overnight with a metal-tagged antibody cocktail (Supplementary
257 Table 2, including anti-FITC, anti-Cy3, anti-Cy5, and anti-biotin) at 4 °C.

258 TMA sections were washed in 0.1 % Triton-X (in DPBS) and DPBS. TMA sections were
259 stained with Cell-ID Ir-Intercalator in DPBS (Standard BioTools). TMA sections were washed
260 in deionised H_2O before being allowed to air dry at RT (Figure 1B).

261

262 **Imaging Mass Cytometry**

263 The Hyperion imaging mass cytometer (Standard BioTools) was used to acquire data from
264 both TMA slides. A pulsed laser scanned and laser ablated the tissue at 200 Hz. IMC data files
265 were analysed using MCD Viewer (version 1.0.560.6, Standard BioTools). MCD Viewer and
266 histoCAT++ (version 2.2)[26] were used for visualising the images, TIFF extraction, and creating
267 representative pseudo-colour images. (Figure 1C-D).

268

269 **Multiplex Immunohistochemistry**

270 FFPE tumour specimen blocks were sectioned at 4 µm and stained using OPAL multiplex IHC
271 (mIHC) staining kit (Akoya Biosciences) according to optimised in-house protocols as
272 previously described [27,28]. Tissue sections were baked at 60 °C for 60 minutes prior to
273 deparaffinisation and rehydration. Heat-induced antigen retrieval was performed by boiling the
274 samples at 100 °C for 15 minutes in pH 9.0 antigen retrieval buffer. Sections were incubated
275 with 3 % hydrogen peroxide prior to washing and blocking (Antibody Diluent/Block, Akoya
276 Biosciences). Sections were then incubated with a single purified primary antibody for 35
277 minutes at RT, washed, and then incubated with HRP (OPAL polymer HRP (Akoya
278 biosciences), sheep-HRP (Invitrogen), or MACH-3 mouse 2-step (Biocare, 10 minutes/step))
279 for 10 minutes at RT. Sections were washed prior to incubation with OPAL fluorochromes
280 diluted in tyramide signalling amplification (TSA) reagent (Akoya Biosciences). Antigen

281 retrieval was repeated, and subsequent antibodies stained for as described above. At completion
282 of all antibody staining, samples were counterstained for DAPI (Cell Signalling Technologies)
283 prior to mounting with Prolong Diamond (Life Technologies).

284 Primary antibodies used were anti-HLA-DR (TAL-1B5, Abcam), anti-FXIIIA (SAF13A,
285 Affinity Biologicals), anti-CD34 (QBEnd/10, Leica), and anti-VEGFA (VG1, Dako). Single
286 marker staining is shown in Supplementary Figure 2.

287 Images (20X for quantification and 20X or 40X for representative images) from 8 HCC
288 specimens within tumour regions were captured using the Mantra quantitative pathology
289 imaging system in combination with Mantra Snap (version 1.0.3, Akoya Biosciences) and
290 inForm (version 2.4.2, Akoya Biosciences) to spectrally process images. Multispectral images
291 were exported as TIFF single images and were then imported into Fiji (version 1.53c) [29] to
292 process representative images. HALO (version 3.6.4134, Indica Labs) was used to perform cell
293 segmentation, threshold markers for cell phenotyping, and spatial analysis. Proximity analysis
294 was performed within the HALO Spatial Analysis module (Indica Labs). Phenotyped cells
295 were registered and plotted together on a single plot. The Proximity Analysis tool was used to
296 identify the number of $VEGFA^{+/-}$ macrophages within a proximity range of 0-100 µm of
297 $CD34^{+}$ endothelial cells and non-endothelial cells in 20 µm increments.

298

299 **Spatial data Analysis**

300 Ilastik software (version 1.4.0b27) was used to segment single cells using the multicut method
301 [30], as this method does not rely on nuclei (Figure 1C). Masks were created to then quantify
302 marker expression levels for each single cell in R (version 4.2.0)[31] using 'Spectre' (version 1.0
303 and development version)[32] (Figure 1D).

304 Single cells were manually gated using FlowJo (version 10.8, BD Bioscience) to identify
305 conventional immune cell subsets (Supplementary Figure 3). The area of each section was
306 calculated using Fiji (version 1.53c) [29], which was then used to calculate the density of each
307 conventional subset. Spectre was then used to quantify, for every cell, the average number of
308 each cell subset within a 20 µm radius.

309 For unsupervised analysis, X-shift clustering (version 26-Apr-2018) was used [33], which
310 identified 238 clusters (Supplementary Figure 4A). The median signal intensity of CD45 was
311 calculated for each cluster before running z-score normalisation. Clusters with values below

312 zero were considered $CD45^{-}$, and values above zero were considered $CD45^{+}$. The latter were
313 divided into $CD45^{low}$ and $CD45^{hi}$ with a cut-off equal to the absolute value of the smallest value
314 (Supplementary Figure 4B). Cells then underwent X-shift clustering within each of the three
315 groups ($CD45^{-}$, $CD45^{low}$, and $CD45^{hi}$) resulting in 91, 36, and 18 clusters respectively. Similar
316 clusters were then combined using the function simprof as part of the 'clustsig' R package
317 (version 1.1)[34], generating 47 clusters (20 $CD45^{+}$ clusters and 27 $CD45^{-}$ clusters)
318 (Supplementary Figure 4C). The spatial data were then quantified using Spectre [32], including
319 cluster densities, average distance between each cluster and every other cluster, average
320 number of cells within 20 µm for each cluster, and the proportions of each cluster. As each
321 region was done in triplicate, the results were averaged so each patient tissue region had a
322 single value for each quantification.

323 When analysing the $CD45^{+}$ clusters, the number of clusters with ≥ 5 cells in each region were
324 calculated. Clusters with < 5 cells across less than a third of total regions were excluded, which
325 removed six clusters (Supplementary Figure 4D).

326 Heatmaps were generated using Spectre. The median signal intensity for each cluster was
327 calculated and then min-max scaled.

328 Each patient region contained thousands of parameters, so linear dimensionality reduction
329 algorithms were used to reduce the complexity. A principal component analysis (PCA) was
330 performed using Spectre to identify differences between the three tissue ROIs: non-tumour,
331 invasive margin, and tumour. A PCA reduced the dimensions based on the overall variance
332 within a given dataset, including human and experimental variability. In addition to a PCA, a
333 sparse partial least squares-discriminant analysis (sPLS-DA) was done [35]. An sPLS-DA
334 reduces the dimensions based on differences between groups and is not as strongly affected by
335 unwanted variability. The R package 'mixOmics' was used for the sPLS-DA (version 6.24.0)[36].
336 The sPLS-DA used leave-one-out validation, calculating the Mahalanobis distance with at least
337 three components generated. When using all clusters, up to ten variables were selected for each
338 component. For select immune cell neighbourhood interactions, there was no limit to the
339 number of variables assessed for each component.

340

341 **Ligand-receptor communication**

342 Single-cell transcriptomic analyses were done using the GSE149614 dataset
343 (https://www.ncbi.nlm.nih.gov/geo/query/acc.cgi?acc=GSE149614), which consisted of cells
344 from paired non-tumour and tumour (8/10 patients) from newly diagnosed HCC patients [37].
345 These patients were pathologically confirmed and proven to have no other cancers. 7/10
346 patients had viral infection (five with HBV, two with HCV), 3/10 had tumour-node-metastasis
347 (TNM) stage I, 1/10 had stage II, 2/10 stage IIIA, 2/10 stage IIIB, and 2/10 stage IV [37]. Pre-
348 processed and pre-annotated data were used. Ligand-receptor communication between cells
349 was calculated using the R package 'CellCall' (version 1.0.7)[38].

350

351 A second cohort of HCC patients were similarly analysed as a validation
352 (https://data.mendeley.com/datasets/skrx2fz79n/1), which similarly consisted of cells from
353 paired non-tumour and tumour regions from six HCC patients [39]. 6/6 had HBV infection.
354 Cluster annotations from the first cohort were transferred to this second cohort using 'scANVI'
355 as part of 'scvi-tools' (version 1.0.4) [40,41] (Supplementary Figure 5). Ligand-receptor
356 communication was then similarly calculated on the transferred clusters.

357

358 **Spatial transcriptomic analysis**

359 Further confirmation was undertaken using publicly available CosMx SMI data made available
360 by nanoString [42]. The data contained one HCC tumour (grade G3, stage II) and one normal
361 liver tissue. Data had undergone cell segmentation and cell annotation. Data were analysed in
362 R using vignette from nanoString [42].

363 Endothelial cells were defined based on pre-annotated data, consisting of central venous liver
364 sinusoidal endothelial cells (LSEC), periportal LSEC, and portal endothelial cells.
365 Macrophages consisted of non-inflammatory and inflammatory macrophages. *CD34*-
366 expressing endothelial cells and *VEGFA*-expressing macrophages were identified based on
367 transcript expression. Close cells were defined as being within 20 µm of each other. Ligand-
368 receptor communication was quantified as described above.

369

370 **Statistical tests**

371 Statistics were calculated using packages available within R [31], using Type III Sum of Squares,
372 unless stated otherwise. Plots were generated using R and GraphPad Prism (version 9.0.0). For
373 the PCA, a permutational multivariate analysis of variance (PERMANOVA) was done. The
374 data were scaled with the Euclidean distance calculated between datapoints. Permutational tests
375 are powerful non-parametric tests that do not assume homogeneity of variance or normality of
376 distribution [43]. 4,999 permutations (for a total of 5,000 tests) were done using all parameters to
377 compare between groups (non-tumour, invasive margin, and tumour regions). The R package
378 'vegan' was used for PERMANOVA calculations (version 2.6-4)[44]. To calculate paired p-
379 values between groups, the R package 'pairwiseAdonis' was used with Holm's correction for
380 multiple comparisons (version 0.4.1)[45]. A similar method was used for the sPLS-DA, but only
381 the parameters that were identified in the first two components were used in their calculation.

382 For the manually gated results, a Friedman test with Dunn's multiple comparison corrections
383 was done to compared between groups (non-tumour, invasive margin, and tumour regions).
384 For comparisons between non-tumour and tumour, a Wilcoxon test was used. These were
385 calculated in Graphpad Prism (version 9.0.0).

386 For comparisons between non-tumour and tumour, a PERMANOVA with Holm's correction
387 was used for the sPLS-DA (as above). For paired comparisons for individual parameters a
388 permutation student's t-test was done using the perm.t.test function as part of the
389 'RVAideMemoire' R package (version 0.9-83)[46].

390

391 **Results**

392 **Study design**

393 Sixteen treatment naïve HCC patients who underwent liver resections were included in this
394 study. Of these patients, twelve were male and the median age was 64.5 years (range 33-84
395 years). The aetiology of chronic liver disease was viral in seven patients, non-viral in eight
396 patients, and dual viral and non-viral pathology in one patient. Nine patients were cirrhotic,
397 and half the cases had evidence of microvascular invasion. The median largest tumour size was
398 36 mm (range 9-270 mm). Quantitative protein expression on single cells and spatial mapping
399 of cellular neighbourhood interactions were performed on patient tissue samples from selected
400 regions (non-tumour, invasive margin, and tumour) (Figure 1C-D).

401

402 **The spatial landscape differs between HCC tumour regions**

403 We mapped the full cellular landscape (immune cells, stromal cells, endothelial cells,
404 hepatocytes, and tumour cells) of HCC to identify any differences between non-tumour,
405 invasive margin, and tumour regions. X-shift clustering was initially performed on all cells.
406 This unbiased approach identified 47 clusters (Figure 2A). The spatial environment was
407 quantified for each patient and tissue region. A PCA was run on > 10,000 parameters, including
408 individual cluster levels (density, percentage of total cells, count), average distances between
409 clusters, and neighbour interactions across each region. Cellular neighbourhoods were inferred
410 based on the average number of one cluster within 20 µm of another (or same) cluster [47]. The
411 PERMANOVA revealed significant differences between the three regions (p=0.0030), which
412 was limited to a difference between non-tumour and tumour (p=0.0006) but not between
413 invasive margin and tumour or non-tumour (Figure 2B, p=0.2467). We then determined the
414 parameters that contribute most to the identified variance. This revealed the primary
415 differentiator as the distance between individual clusters, suggesting that the spatial distribution
416 of cells could be key in HCC (Figure 2C). Using a more targeted approach that provides greater
417 granularity to the parameters that potentially differentiate these regions, the sPLS-DA also
418 showed clear differences between each of the three regions (Figure 2D). The differentiating
419 parameters included not only distance between clusters, but also cell proportions and densities
420 (Figure 2E). Component 1 (represented by the x-axis) separated all regions. Cluster 37,
421 identified as endothelial cells, had differences in density, percentage, and count. Cluster 34,
422 another endothelial cell subset, differed in percentage and count. Cellular neighbourhood

interactions of cluster 44 (myeloid cells) to 16 (hepatocytes), cluster 12 (hepatocytes) to 34 (endothelial cells), and cluster 12 (hepatocytes) to 37 (endothelial cells) also differed between regions, particularly between non-tumour and tumour regions. Component 2 (y-axis) separated the invasive margin, with cellular neighbourhood interactions of cluster 3 (T cells) to 28 (endothelial cells). Together, these data show that our unbiased analytical approach to identify differences in HCC tissue regions demonstrates clear distinctions in the overall cellular landscape. We were particularly interested in the immune cell microenvironment within these regions. Thus, we specifically examined quantities and spatial relationships of immune cells.

Innate, but not adaptive, immune cell densities differ between HCC and adjacent tissue

Differences in the immune landscape of the tumour, invasive margin, and adjacent non-tumour regions were investigated to determine whether cell densities differentiated the three regions. Manual gating analysis was performed to identify conventional immune cell subsets, including both innate and adaptive immune populations (Figure 3). Surprisingly, the densities of these immune subsets were mostly similar across the three regions. T cells (particularly $CD4^+$ T cells) constituted the largest proportion of immune cells across all regions and their densities remained consistent (Figure 3A-B, Supplementary Figure 6A). Of the myeloid cells, macrophages constituted the largest proportion across regions (Figure 3A). There was a higher density of macrophages and dendritic cells within tumour compared to non-tumour regions (Figure 3B).

A more targeted analysis of innate immune cell subsets revealed subsets of macrophages ($CD16^+$ $CD68^+$ $CD206^+$ $CD11c^{+/-}$), possibly monocyte-derived (based on CD14 expression), were significantly higher within tumour compared with non-tumour regions (Figure 3C). In contrast, $CD11c^+$ and $CD11c^-$ macrophages that were $CD14^-$ were not different (Supplementary Figure 6B). These subsets were also higher (as a proportion of total cells) in the tumour compared with non-tumour regions, with the exception of monocyte-derived $CD206^+$ $CD11c^-$ macrophages (Supplementary Figure 6C). As a proportion of total immune cells, only the monocyte-derived $CD11c^+$ macrophages were higher in the tumour compared with non-tumour regions (Supplementary Figure 6C).

There were no significant differences in the density of T cell subsets between regions (Figure 3B). Most T cells were $CD4^+$ rather than $CD8^+$ across regions, with most $CD4^+$ T cells expressing CD69, consistent with tissue-resident $CD4^+$ T cells (Supplementary Figure 6A).

455 Together, these data demonstrate that innate immune cells, particularly monocyte-derived
456 macrophages, are significantly increased within tumour when compared to non-tumour
457 regions.

458

459 **Unique immune cell neighbourhood interactions exist within the HCC tumour**

460 As the densities and proportions of most conventional immune cell subsets were similar across
461 regions, we next spatially analysed these regions to investigate immune cell neighbourhood
462 interactions. When investigating $CD45^+$ clusters alone to focus on immune cells, six clusters
463 had < 5 cells in more than one third of the images, so were removed from further analysis
464 (Supplementary Figure 4D). Furthermore, certain clusters were phenotypically similar to each
465 other based on marker expression and were combined (Supplementary Figure 7). As a result,
466 ten $CD45^+$ clusters were included in the neighbourhood analysis (Figure 4A).

467 To identify immune cell interactions that differ between regions, an sPLS-DA was performed
468 that revealed differences in immune cell neighbourhood interactions between non-tumour and
469 tumour regions (Figure 4B). Multiple immune cell neighbourhood interactions were identified
470 (Figure 4C). The first component (x-axis) parameters were further investigated. Cluster 44 was
471 more commonly within 20 µm of other clusters (including 3, 8, 9, 35, 44) within tumour
472 compared to non-tumour regions. Likewise, cluster 35 was commonly within 20 µm of cluster
473 45, and cluster 9 within 20 µm of cluster 8 within HCC tumour regions. These seven immune
474 cell neighbourhood interactions were identified to be more common within tumour regions
475 when compared to non-tumour regions (Figure 4D). We then determined whether these
476 interactions could have been impacted by individual cell densities. The density of clusters 8, 9,
477 44, and 45 was higher within tumour compared to non-tumour whilst the opposite was true for
478 cluster 35 (Figure 4E). There was no difference in the density of cluster 3 when comparing
479 tumour and non-tumour regions. These data show that multiple immune cell neighbourhood
480 interactions are more frequent within HCC tumour regions when compared to non-tumour
481 regions. Some of these increased cellular neighbourhood interactions may be attributed to
482 increased densities of the cells involved.

483

484 **Increased immune cell interactions with $VEGFA^+$ perivascular macrophages in HCC**
485 **tumour tissue**

486 Having identified cluster 44 at the centre of multiple cellular neighbourhood interactions, this
487 cell cluster was investigated further. Closer examination of the expression markers associated
488 with cluster 44 revealed expression of both CD45 (indicating a haematopoietic cell) and tumour
489 endothelial marker CD34 (Figure 5A). This prompted us to closely examine all images to
490 determine potential close interactions between two different cell types (Supplementary Figure
491 8). We found that cluster 44 was in fact two discrete cells in close proximity: a tumour
492 endothelial cell characterised by CD34 expression, and a myeloid cell which on further
493 phenotyping also expressed CD14, CD16, CD45, CD68, CD86, CD206, FXIIIA, and HLA-
494 DR, but not CD11c (Figure 5B). Based on the close proximity of this myeloid cell to the tumour
495 endothelial cell with reference to the phenotypic markers expressed, including FXIIIA that is
496 expressed by macrophages [48-52], we hypothesised the myeloid cell to be a PVM. Further staining
497 using mIHC, which allowed for greater image resolution, showed that many of these PVM-like
498 cells also expressed VEGFA, suggesting they are indeed PVMs (Figure 5C) [53-55]. These cells
499 were also identified in additional specimens of HCC tissues from eight patients. Representative
500 images of mIHC staining of four of these HCC tumours are shown in Figure 6C. This staining
501 also showed $VEGFA^{-}$ macrophages in close association to $CD34^{+}$ endothelial cells indicating
502 that both $VEGFA^{+}$ and $VEGFA^{-}$ macrophages preferentially reside in close proximity to
503 $CD34^{+}$ endothelial cells (Figure 6A). Analysis of spatial interactions of $VEGF^{+/-}$ macrophages
504 to $CD34^{+}$ endothelial cells in HCC tumour tissue from these eight patients identified that
505 $VEGFA^{+}$ and $VEGFA^{-}$ macrophages preferentially reside 0-20 μm from $CD34^{+}$ endothelial
506 cells (Figure 6A). Although there was no significant difference in the number of $VEGFA^{+}$
507 macrophages compared to $VEGF^{-}$ macrophages in the proximity of $CD34^{+}$ endothelial cells,
508 significantly more $VEGFA^{+}$ and $VEGFA^{-}$ macrophages reside in close proximity (0-20 μm
509 from) to $CD34^{+}$ endothelial cells compared to those residing further away, 40-60, 60-80, 80-
510 100 μm (Figure 6A). In contrast, no significant difference in the number of $VEGFA^{+}$
511 macrophages residing close to non-endothelial cells (0-20 μm) was found when compared to
512 those residing further away (20-100 μm, 20 μm increments) (Figure 6B).

513

514 To determine whether any cell-cell communication was occurring between the $CD34^{+}$
515 endothelial cells and the $VEGFA^{+}$ PVM, publicly-available single-cell transcriptomic data
516 were analysed. The GSE149614 dataset consisted of tumour resections from newly diagnosed
517 HCC patients with paired non-tumour and tumour tissue cell dissociates [37]. The pre-annotated

518 data included endothelial cells expressing *CD34* (C48) and macrophages expressing *VEGFA*
519 (C21) that we considered to most closely resemble PVM. Ligand-receptor communication was
520 inferred using 'CellCall' [38]. When C48 (*CD34*$^+$ endothelial cells) acted as the ligand, several
521 chemokine ligands were predicted to interact with chemokine receptors on C21 in both non-
522 tumour and tumour regions (Figure 5D). When C21 (*VEGFA*$^+$ macrophages) acted as the
523 ligand, there was communication within the tumour but not non-tumour tissue with endothelial
524 cell (C48) receptors. Furthermore, *VEGFA* and *TGFB1* were predicted ligands from C21,
525 suggesting the VEGFA$^+$ macrophages are communicating with CD34$^+$ endothelial cells. To
526 expand upon these results, additional validation was done. Similar findings were observed in
527 two additional publicly available cohorts, including a second single-cell RNA-sequencing
528 (scRNA-seq) cohort and a sub-cellular spatial transcriptomic dataset using CosMx (Figure 7A).
529 *VEGFA*$^+$ macrophages within 20 µm of *CD34*$^+$ endothelial cells are visualised in normal and
530 cancerous liver (Figure 7B). The levels of *VEGFA*$^+$ macrophages and *CD34*$^+$ endothelial cells
531 are summarised in Figure 7C. Despite n = 1, there was a higher density and proportion of
532 *VEGFA*$^+$ macrophages and *CD34*$^+$ endothelial cells within cancerous liver compared to normal
533 liver, as well as a higher level of cellular neighbourhood interactions (Figure 7C). Together
534 these data reveal that tumour regions are not only highly enriched with CD34$^+$ tumour
535 endothelial cells, but also have VEGFA$^+$ PVM that potentially interact with these endothelial
536 cells in that region.

537

538 **Perivascular immune cell aggregates consist of liver-resident CD4$^+$ and CD8$^+$ T cells,**
539 **dendritic cells, and macrophages within HCC tumour tissue**

540 Having identified multiple clusters neighbouring with cluster 44, we then defined all clusters
541 that were found in close proximity of cluster 44. Clusters 3 (Figure 8A) and 9 (Figure 8B) were
542 T cells (CD45$^+$ CD3$^+$). Further phenotyping showed cluster 3 to be CD4$^+$ CD45RO$^+$ CD69$^+$,
543 suggestive of liver-resident memory CD4$^+$ T cells, and cluster 9 to be CD8A$^+$ CD45RO$^+$ CD69$^+$
544 Tbet$^+$ PD-L1$^+$, likely liver-resident memory CD8$^+$ T cells (Figure 8C). Both clusters had a
545 higher interaction with cluster 44 within the tumour, suggesting an interaction between CD4$^+$
546 and CD8$^+$ T cells with PVMs and tumour endothelium.

547 Clusters 8 (Figure 8D) and 35 (Figure 8E) were CD45$^+$ CD14$^+$ HLA-DR$^+$ myeloid cells.
548 Cluster 8 was also CD11c$^+$ CD16$^+$ CD68$^+$ CD206$^+$ FXIIIA$^+$, suggestive of a potential
549 macrophage, while cluster 35 was CD11c$^-$ CD16$^+$ CD68$^+$ CD206$^+$ FXIIIA$^-$, possibly

550 representing a dendritic cell population (Figure 8F). The increased cellular neighbourhood
551 interaction of these cells with PVM-endothelial cell cluster (cluster 44) in the HCC tumour
552 tissue points to an interaction between the tumour endothelium/PVM niche and other myeloid
553 cells within the TME.

554 Cluster 8, a macrophage subset, was also found to have a cellular neighbourhood interaction
555 with cluster 9, a memory $CD8^+$ T cell subset (Figure 9A, Supplementary Figure 9). Clusters 35
556 (a dendritic cell subset) and 45 were both $CD45^+$ $CD14^+$ HLA-DR^+. Cluster 45 had a
557 macrophage phenotype as $CD16^+$ $CD68^+$ $FXIIIA^+$ (Figure 9C). The cellular neighbourhood
558 interactions between these two myeloid cell populations were also higher in the tumour
559 compared to non-tumour regions (Figure 9B) despite the density of cluster 35 being lower in
560 the tumour compared to the non-tumour regions (Figure 4E). Together, these single cell maps
561 reveal that unique intratumoural immune aggregates (consisting of T cells, dendritic cells, and
562 macrophages) interact with PVM and may exert potential pro-tumoural and angiogenic
563 functions. These findings are summarised in Figure 10.

564

565 Clinical associations were assessed by correlating tumour cellular neighbourhood interactions
566 with prognostic and clinicopathological data. There were no associations between tumour
567 cellular neighbourhood interactions and cirrhosis, early recurrence (<2 years), MVI, or viral-
568 associated HCC (Supplementary Figure 10).

569

570

571 **Discussion**

572 The treatment of HCC remains a major challenge and novel therapeutic strategies are urgently
573 required. Irrespective of its aetiology, HCC mostly develops in diseased liver with concomitant
574 chronic inflammation, thus implicating the immune system in both the pathogenesis of the
575 disease as well as tumour control. Understanding the complex interactions between immune
576 cells and the TME is therefore paramount [56,57]. We used high-dimensional spatial analysis to
577 map multiple cellular neighbourhood interactions across three regions: the non-tumour,
578 invasive margin, and tumour regions. Mapping the immune landscape across these regions
579 showed that only innate cell densities, but not T cell or B cell densities, are increased within
580 tumour regions compared to non-tumour regions and that macrophages (likely monocyte-
581 derived) are enriched within tumour tissue. We further identified immune aggregates around
582 the perivascular space that are unique to the tumour region. Detailed analysis of this region
583 shows that PVMs are at the centre of these interactions and are closely associated with not only
584 the tumour endothelial cells, but also multiple immune populations, including liver-resident
585 $CD4^+$ and $CD8^+$ T cells, macrophages, and dendritic cells. Functionally, we show that these
586 PVMs were associated with VEGFA, which is known to be a key driver of angiogenesis and
587 hypervascularity within tumours. Mining publicly available scRNA-seq and spatial
588 transcriptomic datasets to interrogate potential ligand-receptor interactions between PVMs and
589 endothelial cells confirms VEGFA- VEGF receptor interactions and also suggests that other
590 potential pro-tumoural mechanisms involving transforming growth factor-beta (TGF-β) are
591 active within these unique immune aggregates.

592

593 How the tumour immune microenvironment and its composition is impacted by
594 hepatocarcinogenesis remains unclear. Our data show enrichment of phenotypically diverse
595 populations of macrophages within the tumour compared to non-tumour regions. Based on
596 CD14 expression, these populations were most likely monocyte-derived [58,59]. This is in-line
597 with the consensus in the field that tumour-associated macrophages (TAMs) are derived
598 primarily from circulating blood monocytes [60], and in human HCC, TAMs arise from $CCR2^+$
599 monocytes [61]. Interestingly, we found other $CD14^-$ macrophage populations were either
600 reduced within tumours or did not show any difference compared to adjacent non-tumour
601 tissue. This, together with no changes in $CD8^+$ T cell or $CD4^+$ T cell subset densities between
602 tumour and non-tumour regions, suggests that the tumour immune microenvironment may be

skewed by the recruitment of monocytes. Furthermore, our findings on several myeloid cell populations regarding their overall numbers and cell-cell interactions should be compared with the findings of Wu *et al.* who devised a myeloid response score (MRS) in using 244 resected human HCC samples [62]. Tumours with a high MRS score were enriched in CD11b$^+$, CD15$^+$, CD163$^+$, CD33$^+$, CD68$^+$, and CD204$^+$ cells. These were thought to be immunosuppressive in nature and associated with poor prognosis. In addition, Kurebayashi *et al.* found that macrophages were the most common immune cell detected in 919 regions from 158 resected HCC tumours [63]. CD68 is commonly used as a liver TAM marker [64] and this subset was found to be increased in our tumours. Similarly, CD206$^+$ CD14$^+$ monocyte-derived macrophages were also enriched within the tumour in our study. A dysregulated balance towards CD206$^+$ M2 polarised macrophages has also been associated with aggressive tumour phenotypes and worse prognosis in HCC [65].

Where these macrophages localise within tumour tissue is critical to our understanding of how the immune environment impacts tumour development, persistence, as well as tumour control. Many previous studies have interrogated the TME in HCC using various techniques including mIHC [62,63,66], IMC [22,67], and multimodal genomic analysis incorporating scRNA-seq and TCR receptor sequencing [68-70]. However, not all these techniques facilitate spatial analyses to identify cell-cell interactions between multiple different types of cells within the TME. Our study provides a comprehensive analysis of the composition of the tumour immune microenvironment of HCC and adjacent non-tumour tissue whilst further identifying novel cell-cell interactions between immune cells and the tumour vasculature. Through this spatial mapping we have identified a cellular neighbourhood around the endothelium and PVMs of potential importance.

The close physical association between tumour endothelial cells and macrophages prompted us to define them as PVMs. Currently, there is no consensus on the definition of PVMs as they can have different phenotypes across tissues. However, a unifying feature is that they lie in close proximity to blood vessels, either in direct contact or located within one cell thickness from it [55]. However, PVMs have not yet been described in healthy adult liver tissue. In diseased tissues such as cancer, these cells have been shown to express VEGFA [54,55]. We also show that these PVMs are indeed able to produce VEGFA. Importantly, pre-clinical models show that

635 PVMs are also largely derived from circulating monocytes [54]. In line with this, Matasubra *et*
636 *al.* found that the majority of angiopoietin (TIE2$^+$) expressing macrophages in liver cancer
637 were located in the perivascular areas of tumour tissue and their presence not only correlated
638 with the degree of angiogenesis, but also with the levels of their counterparts in blood [71].
639 Several other functions of PVMs have been described both in other healthy adult tissues
640 (phagocytosis, antigen presentation, and immune regulation), and in the progression of
641 pathological conditions (angiogenesis, metastasis, immunosuppression, recruitment of other
642 leukocytes, and post-therapy relapse) [55]. It is tempting to postulate that PVMs are critical not
643 only for angiogenesis and hypervascularity in HCC through the secretion of VEGFA but are
644 also responsible for the 'leaky' vessels seen in HCC that compromise immune control
645 mechanisms. There is evidence from pre-clinical models to support both these possibilities.
646 TIE2-expressing monocytes were found to be critical for tumour angiogenesis [72], supporting
647 the fact monocyte-derived cells within tumours are key for angiogenesis. In addition, in a
648 murine model of breast cancer, macrophage-specific depletion of VEGFA reduced both
649 vascular permeability and circulating tumour cells whilst restoring vascular junctions [53].

650

651 Our TMA selection criteria of highly abundant TILs on H&E suggest we have selected areas
652 that share features of the *Inflamed Class* of HCC [70,73]. This class represents approximately 35 %
653 of HCC tumours and is characterised by a microenvironment with increased interferon
654 signalling and higher immune infiltration (increased TILs, macrophages, tertiary lymphoid
655 structures, and elevated expression of checkpoint molecules) compared with non-inflamed
656 tumours [70]. The inflamed subclass exhibits a significantly higher fraction of CD8$^+$ T cells and
657 M1 macrophages when compared to the non-inflamed profiles. However, despite the presence
658 of high TILs, these tumours persist. There could be many factors that contribute to this tumour
659 persistence, including enrichment of clonally exhausted CD8$^+$ T cells and regulatory T cells
660 within HCC tissues [68]. Our finding of no difference in the T cell density between tumour and
661 non-tumour tissues is of interest. We also found that CD4$^+$ T cells were more abundant than
662 CD8$^+$ T cells within the HCC TME, consistent with previous studies [63]. Furthermore, CD4$^+$ T
663 cells expressing CD69 were the most common subset of CD4$^+$ T cells across all regions in our
664 study. Importantly, we found close interactions between these T cells and PVMs in the
665 perivascular space. This niche could facilitate regulatory interactions for effector and resident
666 T cells. We also identified multiple myeloid cells interacting with T cells within this niche,

667 although the functional role of these myeloid cells remains unknown. Further studies are
668 required to identify how and why T cells are potentially impaired within such tumour regions.

669

670 The findings from our study have several clinical implications. The identification of increased
671 TIL density within a perivascular-immune neighbourhood (consisting of tumour endothelial
672 cells and PVMs) warrants discussion of current therapeutic approaches that target immune-
673 vascular cross-talk and the role of vascular normalisation in HCC [74]. The tumour vasculature
674 in HCC is structurally and functionally abnormal, and the tumour vessels are excessively leaky
675 [75]. Immune-vascular cross-talk underpins the rationale for using bevacizumab, an anti-VEGFA
676 monoclonal antibody that normalises tumour vasculature, in conjunction with immune
677 checkpoint inhibitors in advanced unresectable HCC [5]. Advanced colorectal cancer patients
678 receiving combined FOLFOX and bevacizumab have decreased VEGFB-mediated
679 angiogenesis, including reduced myeloid cell-endothelial cell communication via VEGF as
680 identified by scRNA-seq [76]. In pre-clinical HCC models, anti-angiogenic therapy in
681 conjunction with anti-PD-1 therapy further promotes vascular normalisation mediated by $CD4^+$
682 T cells [16]. Recently, biomarkers for response to systemic therapies in advanced HCC have been
683 developed. Haber *et al.* found that tumours expressing high amounts of an 11-gene signature
684 (IFNAP) captured a unique immune microenvironment characterised by a high gene expression
685 of activated $CD4^+$ memory T cells, M1 macrophages, and plasma cells. This novel signature
686 predicted response and survival in patients treated in the first-line setting with anti-PD1
687 monotherapy [77]. However, this study did not incorporate spatial analyses to determine immune
688 cell interactions within the immune microenvironment captured by the IFNAP gene signature.

689

690 There are notable limitations to our study. Single-cell sequencing of TILs in HCC has identified
691 eleven unique subsets: five $CD8^+$ and six $CD4^+$ T cell clusters including naïve, effector, and
692 exhausted T cells, and mucosal-associated invariant T (MAIT) cells [68]. We were unable to
693 identify some of these subsets (undefined lymphocytes and undefined non-lymphocyte
694 immune cells) due to constraints on the number of markers that can be included in a single
695 IMC panel. Cell segmentation can become problematic when defining single cells sectioned
696 from a three-dimensional organ. As such, cluster 44 was first identified as a single cell rather
697 than two discrete closely interacting cells. This issue was resolved by examining representative
698 images to confirm the presence of two discrete cells. Functionality of the PVM population was

699 inferred by *in silico* analysis, rather than single cell analysis or cell isolation and culture
700 experiments *ex vivo*. Finally, our sample size was small. Correlations with prognostic and
701 clinicopathological data were performed but no associations were found, perhaps related to the
702 limited sample size.

703

704 In summary, our study has identified a novel myeloid population in HCC characteristic of
705 PVMs, and identified several immune cell and vascular neighbourhood interactions occurring
706 more commonly within HCC tumours. Using IMC, we were able to comprehensively
707 immunophenotype and spatially map the immune landscape of human HCC tumour and
708 adjacent non-tumour tissue. Further studies are required to evaluate the function of these
709 immune cells, their effect on immune-mediated tumour control and therapeutic responses, and
710 their role in hepatocarcinogenesis and HCC progression.

711

712 **Acknowledgements**

713 Assistance with the study: We gratefully acknowledge the subsidised access to Sydney
714 Cytometry and thank the support staff in this core facility for their assistance. We thank the
715 Australian Centre for Microscopy & Microanalysis at the University of Sydney for their
716 assistance with this work.

717 Presentations: Preliminary data were presented at the 2023 EASL Liver Cancer Summit
718 (Estoril, Portugal); 2023 CYTO (Montreal, Canada); and GESA AGW (Brisbane, Australia).

719

720 **References**

721 **Author names in bold designate shared co-first authorship**

722 1. Sung H, Ferlay J, Siegel RL, et al. Global Cancer Statistics 2020: GLOBOCAN Estimates of
723 Incidence and Mortality Worldwide for 36 Cancers in 185 Countries. *CA Cancer J Clin*. May
724 2021;71(3):209-249. doi:10.3322/caac.21660
725 2. Llovet JM, Kelley RK, Villanueva A, et al. Hepatocellular carcinoma. *Nat Rev Dis Primers*. Jan
726 21 2021;7(1):6. doi:10.1038/s41572-020-00240-3
727 3. Siegel RL, Miller KD, Fuchs HE, Jemal A. Cancer statistics, 2022. *CA Cancer J Clin*. Jan
728 2022;72(1):7-33. doi:10.3322/caac.21708
729 4. Amicone L, Marchetti A. Microenvironment and tumor cells: two targets for new molecular
730 therapies of hepatocellular carcinoma. *Transl Gastroenterol Hepatol*. 2018;3:24.
731 doi:10.21037/tgh.2018.04.05
732 5. Finn RS, Qin S, Ikeda M, et al. Atezolizumab plus Bevacizumab in Unresectable
733 Hepatocellular Carcinoma. *The New England journal of medicine*. May 14 2020;382(20):1894-1905.
734 doi:10.1056/NEJMoa1915745
735 6. Abou-Alfa GK, Lau G, Kudo M, et al. Tremelimumab plus Durvalumab in Unresectable
736 Hepatocellular Carcinoma. *NEJM Evidence*. 2022;1(8)doi:10.1056/EVIDoa2100070
737 7. Ren Z, Xu J, Bai Y, et al. Sintilimab plus a bevacizumab biosimilar (IBI305) versus sorafenib in
738 unresectable hepatocellular carcinoma (ORIENT-32): a randomised, open-label, phase 2–3 study. *The*
739 *Lancet Oncology*. 2021;22(7):977-990. doi:10.1016/s1470-2045(21)00252-7
740 8. Ringelhan M, Pfister D, O'Connor T, Pikarsky E, Heikenwalder M. The immunology of
741 hepatocellular carcinoma. *Nature immunology*. Mar 2018;19(3):222-232. doi:10.1038/s41590-018-
742 0044-z
743 9. **Aliya S**, **Lee H**, Alhammadi M, Umapathi R, Huh YS. An Overview on Single-Cell Technology
744 for Hepatocellular Carcinoma Diagnosis. *International journal of molecular sciences*. Jan 26
745 2022;23(3)doi:10.3390/ijms23031402
746 10. Yamaguchi S, Tomomatsu N, Kagoshima M, Okumoto T, Komatsu H. Effects of Y-24180, a
747 receptor antagonist to platelet-activating factor, on allergic cutaneous eosinophilia in mice. *Life*
748 *sciences*. 1999;64(11):PL139-44. doi:10.1016/s0024-3205(99)00024-7
749 11. Morse MA, Sun W, Kim R, et al. The Role of Angiogenesis in Hepatocellular Carcinoma. *Clin*
750 *Cancer Res*. Feb 1 2019;25(3):912-920. doi:10.1158/1078-0432.CCR-18-1254
751 12. Liu K, Dennis C, Prince DS, et al. Vessels that encapsulate tumour clusters vascular pattern in
752 hepatocellular carcinoma. *JHEP Rep*. Aug 2023;5(8):100792. doi:10.1016/j.jhepr.2023.100792
753 13. Yamaguchi R, Yano H, Iemura A, Ogasawara S, Haramaki M, Kojiro M. Expression of vascular
754 endothelial growth factor in human hepatocellular carcinoma. *Hepatology*. Jul 1998;28(1):68-77.
755 doi:10.1002/hep.510280111
756 14. Kaseb AO, Hanbali A, Cotant M, Hassan MM, Wollner I, Philip PA. Vascular endothelial
757 growth factor in the management of hepatocellular carcinoma: a review of literature. *Cancer*. Nov 1
758 2009;115(21):4895-906. doi:10.1002/cncr.24537
759 15. Tian L, Goldstein A, Wang H, et al. Mutual regulation of tumour vessel normalization and
760 immunostimulatory reprogramming. *Nature*. Apr 13 2017;544(7649):250-254.
761 doi:10.1038/nature21724
762 16. **Shigeta K**, **Datta M**, **Hato T**, et al. Dual Programmed Death Receptor-1 and Vascular
763 Endothelial Growth Factor Receptor-2 Blockade Promotes Vascular Normalization and Enhances
764 Antitumor Immune Responses in Hepatocellular Carcinoma. *Hepatology*. Apr 2020;71(4):1247-1261.
765 doi:10.1002/hep.30889
766 17. **Shen H**, **Yu H**, **Li QY**, et al. Hepatocyte-derived VEGFA accelerates the progression of non-
767 alcoholic fatty liver disease to hepatocellular carcinoma via activating hepatic stellate cells. *Acta*
768 *Pharmacol Sin*. May 4 2022;doi:10.1038/s41401-022-00907-5

18. **Cheng S**, **Li Z**, Gao R, et al. A pan-cancer single-cell transcriptional atlas of tumor infiltrating myeloid cells. *Cell*. Feb 4 2021;184(3):792-809 e23. doi:10.1016/j.cell.2021.01.010

19. Sharma A, Seow JJW, Dutertre CA, et al. Onco-fetal Reprogramming of Endothelial Cells Drives Immunosuppressive Macrophages in Hepatocellular Carcinoma. *Cell*. Oct 15 2020;183(2):377-394 e21. doi:10.1016/j.cell.2020.08.040

20. Traum D, Wang YJ, Schwarz KB, et al. Highly multiplexed 2-dimensional imaging mass cytometry analysis of HBV-infected liver. *JCI Insight*. Apr 8 2021;6(7):e146883. doi:10.1172/jci.insight.146883

21. **Ho WJ**, **Zhu Q**, Durham J, et al. Neoadjuvant cabozantinib and nivolumab convert locally advanced hepatocellular carcinoma into resectable disease with enhanced antitumor immunity. *Nature Cancer*. 2021;doi:10.1038/s43018-021-00234-4

22. **Sheng J**, **Zhang J**, Wang L, et al. Topological analysis of hepatocellular carcinoma tumour microenvironment based on imaging mass cytometry reveals cellular neighbourhood regulated reversely by macrophages with different ontogeny. *Gut*. Jun 2022;71(6):1176-1191. doi:10.1136/gutjnl-2021-324339

23. Ramachandran P, Dobie R, Wilson-Kanamori JR, et al. Resolving the fibrotic niche of human liver cirrhosis at single-cell level. *Nature*. Nov 2019;575(7783):512-518. doi:10.1038/s41586-019-1631-3

24. Ruf B, Bruhns M, Babaei S, et al. Tumor-associated macrophages trigger MAIT cell dysfunction at the HCC invasive margin. *Cell*. Aug 17 2023;186(17):3686-3705 e32. doi:10.1016/j.cell.2023.07.026

25. Ferguson AL, Sharman AR, Allen RO, et al. High-Dimensional and Spatial Analysis Reveals Immune Landscape-Dependent Progression in Cutaneous Squamous Cell Carcinoma. *Clin Cancer Res*. Nov 1 2022;28(21):4677-4688. doi:10.1158/1078-0432.CCR-22-1332

26. Catena R, Montuenga LM, Bodenmiller B. Ruthenium counterstaining for imaging mass cytometry. *The Journal of pathology*. Apr 2018;244(4):479-484. doi:10.1002/path.5049

27. **Hewavisenti R**, **Ferguson A**, Wang K, et al. CD103+ tumor-resident CD8+ T cell numbers underlie improved patient survival in oropharyngeal squamous cell carcinoma. *J Immunother Cancer*. Jun 2020;8(1)doi:10.1136/jitc-2019-000452

28. Hewavisenti RV, Ferguson AL, Gasparini G, et al. Tissue-resident regulatory T cells accumulate at human barrier lymphoid organs. *Immunology and cell biology*. Sep 2021;99(8):894-906. doi:10.1111/imcb.12481

29. Schindelin J, Arganda-Carreras I, Frise E, et al. Fiji: an open-source platform for biological-image analysis. *Nat Methods*. Jun 28 2012;9(7):676-82. doi:10.1038/nmeth.2019

30. Berg S, Kutra D, Kroeger T, et al. ilastik: interactive machine learning for (bio)image analysis. *Nat Methods*. Dec 2019;16(12):1226-1232. doi:10.1038/s41592-019-0582-9

31. *R: A language and environment for statistical computing*. R Foundation for Statistical Computing; 2021. https://www.R-project.org/

32. **Ashhurst TM**, **Marsh-Wakefield F**, **Putri GH**, et al. Integration, exploration, and analysis of high-dimensional single-cell cytometry data using Spectre. *Cytometry Part A : the journal of the International Society for Analytical Cytology*. Mar 2022;101(3):237-253. doi:10.1002/cyto.a.24350

33. Samusik N, Good Z, Spitzer MH, Davis KL, Nolan GP. Automated mapping of phenotype space with single-cell data. *Nat Methods*. Jun 2016;13(6):493-6. doi:10.1038/nmeth.3863

34. Clarke KR, Somerfield PJ, Gorley RN. Testing of null hypotheses in exploratory community analyses: similarity profiles and biota-environment linkage. *Journal of Experimental Marine Biology and Ecology*. 2008;366(1-2):56-69. doi:10.1016/j.jembe.2008.07.009

35. Marsh-Wakefield F, Juillard P, Ashhurst TM, et al. Peripheral B-cell dysregulation is associated with relapse after long-term quiescence in patients with multiple sclerosis. *Immunology and cell biology*. Jul 2022;100(6):453-467. doi:10.1111/imcb.12552

818 36. Rohart F, Gautier B, Singh A, Le Cao KA. mixOmics: An R package for 'omics feature selection
819 and multiple data integration. *PLoS Comput Biol*. Nov 2017;13(11):e1005752.
820 doi:10.1371/journal.pcbi.1005752
821 37. **Lu Y**, **Yang A**, **Quan C**, et al. A single-cell atlas of the multicellular ecosystem of primary and
822 metastatic hepatocellular carcinoma. *Nat Commun*. Aug 6 2022;13(1):4594. doi:10.1038/s41467-
823 022-32283-3
824 38. Zhang Y, Liu T, Hu X, et al. CellCall: integrating paired ligand-receptor and transcription factor
825 activities for cell-cell communication. *Nucleic Acids Res*. Sep 7 2021;49(15):8520-8534.
826 doi:10.1093/nar/gkab638
827 39. **Liu Y**, **Xun Z**, **Ma K**, et al. Identification of a tumour immune barrier in the HCC
828 microenvironment that determines the efficacy of immunotherapy. *Journal of hepatology*. Jan 25
829 2023;doi:10.1016/j.jhep.2023.01.011
830 40. **Xu C**, **Lopez R**, **Mehlman E**, Regier J, Jordan MI, Yosef N. Probabilistic harmonization and
831 annotation of single-cell transcriptomics data with deep generative models. *Mol Syst Biol*. Jan
832 2021;17(1):e9620. doi:10.15252/msb.20209620
833 41. Luecken MD, Buttner M, Chaichoompu K, et al. Benchmarking atlas-level data integration in
834 single-cell genomics. *Nat Methods*. Jan 2022;19(1):41-50. doi:10.1038/s41592-021-01336-8
835 42. nanoString. CosMx SMI Human Liver FFPE Dataset. Accessed 02/09/2023,
836 https://nanostring.com/products/cosmx-spatial-molecular-imager/ffpe-dataset/human-liver-rna-
837 ffpe-dataset/
838 43. Anderson MJ. A new method for non-parametric multivariate analysis of variance. *Austral*
839 *Ecol*. Feb 2001;26(1):32-46. doi:DOI 10.1046/j.1442-9993.2001.01070.x
840 44. *vegan: Community Ecology Package*. 2019. https://CRAN.R-project.org/package=vegan
841 45. *pairwiseAdonis: Pairwise Multilevel Comparison using Adonis*. 2017.
842 https://github.com/pmartinezarbizu/pairwiseAdonis
843 46. *RVAideMemoire: Testing and Plotting Procedures for Biostatistics*. 2021. https://CRAN.R-
844 project.org/package=RVAideMemoire
845 47. Gide TN, Silva IP, Quek C, et al. Close proximity of immune and tumor cells underlies
846 response to anti-PD-1 based therapies in metastatic melanoma patients. *Oncoimmunology*.
847 2020;9(1):1659093. doi:10.1080/2162402x.2019.1659093
848 48. Henriksson P, Becker S, Lynch G, McDonagh J. Identification of intracellular factor XIII in
849 human monocytes and macrophages. *Journal of Clinical Investigation*. 1985;76(2):528-534.
850 doi:10.1172/jci112002
851 49. Muszbek L, Adany R, Szegedi G, Polgar J, Kavai M. Factor XIII of blood coagulation in human
852 monocytes. *Thromb Res*. Feb 1 1985;37(3):401-10. doi:10.1016/0049-3848(85)90069-6
853 50. Muszbek L, Yee VC, Hevessy Z. Blood coagulation factor XIII: structure and function. *Thromb*
854 *Res*. Jun 1 1999;94(5):271-305. doi:10.1016/s0049-3848(99)00023-7
855 51. Adany R, Bardos H. Factor XIII subunit A as an intracellular transglutaminase. *Cell Mol Life*
856 *Sci*. Jun 2003;60(6):1049-60. doi:10.1007/s00018-003-2178-9
857 52. Torocsik D, Bardos H, Hatalyak Z, et al. Detection of factor XIII-A is a valuable tool for
858 distinguishing dendritic cells and tissue macrophages in granuloma annulare and necrobiosis
859 lipoidica. *J Eur Acad Dermatol Venereol*. Aug 2014;28(8):1087-96. doi:10.1111/jdv.12290
860 53. Harney AS, Arwert EN, Entenberg D, et al. Real-Time Imaging Reveals Local, Transient
861 Vascular Permeability, and Tumor Cell Intravasation Stimulated by TIE2hi Macrophage-Derived
862 VEGFA. *Cancer Discov*. Sep 2015;5(9):932-43. doi:10.1158/2159-8290.CD-15-0012
863 54. Lewis CE, Harney AS, Pollard JW. The Multifaceted Role of Perivascular Macrophages in
864 Tumors. *Cancer cell*. Jul 11 2016;30(1):18-25. doi:10.1016/j.ccell.2016.05.017
865 55. Lapenna A, De Palma M, Lewis CE. Perivascular macrophages in health and disease. *Nature*
866 *reviews Immunology*. Nov 2018;18(11):689-702. doi:10.1038/s41577-018-0056-9

867 56. Marsh-Wakefield F, Ferguson AL, Liu K, Santhakumar C, McCaughan G, Palendira U.
868 Approaches to spatially resolving the tumour immune microenvironment of hepatocellular
869 carcinoma. *Ther Adv Med Oncol*. 2022;14:17588359221113270. doi:10.1177/17588359221113270
870 57. Wang Y, Wang P, Zhang Z, Zhou J, Fan J, Sun Y. Dissecting the tumor ecosystem of liver
871 cancers in the single-cell era. *Hepatol Commun*. Sep 1
872 2023;7(9)doi:10.1097/HC9.0000000000000248
873 58. Haniffa M, Ginhoux F, Wang XN, et al. Differential rates of replacement of human dermal
874 dendritic cells and macrophages during hematopoietic stem cell transplantation. *The Journal of*
875 *experimental medicine*. Feb 16 2009;206(2):371-85. doi:10.1084/jem.20081633
876 59. **McGovern N**, **Schlitzer A**, **Gunawan M**, et al. Human dermal CD14(+) cells are a transient
877 population of monocyte-derived macrophages. *Immunity*. Sep 18 2014;41(3):465-477.
878 doi:10.1016/j.immuni.2014.08.006
879 60. Yang L, Zhang Y. Tumor-associated macrophages: from basic research to clinical application.
880 *J Hematol Oncol*. Feb 28 2017;10(1):58. doi:10.1186/s13045-017-0430-2
881 61. Li X, Yao W, Yuan Y, et al. Targeting of tumour-infiltrating macrophages via CCL2/CCR2
882 signalling as a therapeutic strategy against hepatocellular carcinoma. *Gut*. Jan 2017;66(1):157-167.
883 doi:10.1136/gutjnl-2015-310514
884 62. Wu C, Lin J, Weng Y, et al. Myeloid signature reveals immune contexture and predicts the
885 prognosis of hepatocellular carcinoma. *The Journal of clinical investigation*. Sep 1 2020;130(9):4679-
886 4693. doi:10.1172/JCI135048
887 63. Kurebayashi Y, Ojima H, Tsujikawa H, et al. Landscape of immune microenvironment in
888 hepatocellular carcinoma and its additional impact on histological and molecular classification.
889 *Hepatology*. Sep 2018;68(3):1025-1041. doi:10.1002/hep.29904
890 64. Donne R, Lujambio A. The liver cancer immune microenvironment: Therapeutic implications
891 for hepatocellular carcinoma. *Hepatology*. May 1 2023;77(5):1773-1796. doi:10.1002/hep.32740
892 65. **Dong P**, **Ma L**, Liu L, et al. CD86(+)/CD206(+), Diametrically Polarized Tumor-Associated
893 Macrophages, Predict Hepatocellular Carcinoma Patient Prognosis. *International journal of*
894 *molecular sciences*. Mar 1 2016;17(3):320. doi:10.3390/ijms17030320
895 66. Sia D, Jiao Y, Martinez-Quetglas I, et al. Identification of an Immune-specific Class of
896 Hepatocellular Carcinoma, Based on Molecular Features. *Gastroenterology*. Sep 2017;153(3):812-
897 826. doi:10.1053/j.gastro.2017.06.007
898 67. Mi H, Ho WJ, Yarchoan M, Popel AS. Multi-Scale Spatial Analysis of the Tumor
899 Microenvironment Reveals Features of Cabozantinib and Nivolumab Efficacy in Hepatocellular
900 Carcinoma. *Frontiers in immunology*. 2022;13:892250. doi:10.3389/fimmu.2022.892250
901 68. **Zheng C**, **Zheng L**, **Yoo JK**, et al. Landscape of Infiltrating T Cells in Liver Cancer Revealed by
902 Single-Cell Sequencing. *Cell*. Jun 15 2017;169(7):1342-1356 e16. doi:10.1016/j.cell.2017.05.035
903 69. **Zhang Q**, **He Y**, **Luo N**, et al. Landscape and Dynamics of Single Immune Cells in
904 Hepatocellular Carcinoma. *Cell*. Oct 31 2019;179(4):829-845 e20. doi:10.1016/j.cell.2019.10.003
905 70. **Montironi C**, **Castet F**, **Haber PK**, et al. Inflamed and non-inflamed classes of HCC: a revised
906 immunogenomic classification. *Gut*. Jan 2023;72(1):129-140. doi:10.1136/gutjnl-2021-325918
907 71. Matsubara T, Kanto T, Kuroda S, et al. TIE2-expressing monocytes as a diagnostic marker for
908 hepatocellular carcinoma correlates with angiogenesis. *Hepatology*. Apr 2013;57(4):1416-25.
909 doi:10.1002/hep.25965
910 72. **De Palma M**, **Venneri MA**, Galli R, et al. Tie2 identifies a hematopoietic lineage of
911 proangiogenic monocytes required for tumor vessel formation and a mesenchymal population of
912 pericyte progenitors. *Cancer cell*. Sep 2005;8(3):211-26. doi:10.1016/j.ccr.2005.08.002
913 73. Galon J, Bruni D. Approaches to treat immune hot, altered and cold tumours with
914 combination immunotherapies. *Nat Rev Drug Discov*. Mar 2019;18(3):197-218. doi:10.1038/s41573-
915 018-0007-y

916 74. Liu K, Zhang X, Xu W, et al. Targeting the vasculature in hepatocellular carcinoma treatment:
917 Starving versus normalizing blood supply. *Clin Transl Gastroenterol*. Jun 15 2017;8(6):e98.
918 doi:10.1038/ctg.2017.28
919 75. Santhakumar C, Gane EJ, Liu K, McCaughan GW. Current perspectives on the tumor
920 microenvironment in hepatocellular carcinoma. *Hepatol Int*. Dec 2020;14(6):947-957.
921 doi:10.1007/s12072-020-10104-3
922 76. Yang M, Yang C, Ma D, Li Z, Zhao W, Yang D. Single-cell analysis reveals cellular
923 reprogramming in advanced colon cancer following FOLFOX-bevacizumab treatment. *Front Oncol*.
924 2023;13:1219642. doi:10.3389/fonc.2023.1219642
925 77. Haber PK, Castet F, Torres-Martin M, et al. Molecular Markers of Response to Anti-PD1
926 Therapy in Advanced Hepatocellular Carcinoma. *Gastroenterology*. Jan 2023;164(1):72-88 e18.
927 doi:10.1053/j.gastro.2022.09.005

928

929

930 **Figure legends**

931 **Figure 1 – Experimental overview**. A) Sixteen HCC patients underwent liver resections.
932 1 mm diameter regions of non-tumour, invasive margin, and tumour were selected from each
933 patient in triplicate to create a tissue microarray. B) Sections were stained with antibodies
934 conjugated to heavy metals which were then ablated by a Helios imaging mass cytometer to
935 quantify regions. C) Ilastik software was used to define cell borders to create a mask of single
936 cells. D) R package Spectre quantified marker expression for each segmented cell across
937 regions.

938

939 **Figure 2 – Spatial environment differs between liver regions**. A) X-shift clustering was
940 used to identify 47 clusters represented by a heatmap. Each row is a different cluster, each
941 column a different marker. B) Principal component analysis (PCA) of all spatial data. Symbols
942 and colours represent a different region from individual patients. 95 % confidence interval
943 shown. A PERMANOVA with Holm's correction was performed on all parameters. C) The
944 parameters that contributed most to the variance across the first two components are shown.
945 Horizontal red dashed line represents the value if all parameters contributed equally. D) A
946 sparse partial least squares-discriminant analysis (sPLS-DA) generated a similar plot, with the
947 selected parameters for the first two components shown. A PERMANOVA with Holm's
948 correction was performed on select parameters from the first two components. E) The
949 parameters that contribute most to the differences between regions across the first two
950 components are shown. n = 16 HCC patients, each with non-tumour, invasive margin, and
951 tumour regions.

952

953 **Figure 3 – Tumour has higher densities of monocyte-derived CD11c$^+$ and CD11c$^-$**
954 **macrophage subsets compared to non-tumour regions**. A) Proportion of conventional
955 immune cells across regions. B) The density of conventional immune subsets across regions.
956 Friedman test with Dunn's multiple comparison corrections was performed. C) Log_2 fold
957 change comparing densities of monocyte-derived CD11c$^+$ and CD11c$^-$ macrophages between
958 tumour and non-tumour regions. Wilcoxon test was used. *$p<0.05$, **$p<0.01$, ***$p<0.001$.
959 n = 16 HCC patients.

960

961 **Figure 4 – Immune cell neighbours differ between non-tumour and tumour regions**. A)
962 Heatmap of CD45$^+$ clusters. Each row is a cluster, each column is a marker. B) sPLS-DA
963 comparing non-tumour to tumour regions. Symbols and colours represent a different region
964 from individual patients. 95 % confidence interval shown. C) Selected parameters for the first
965 two components are shown. Select comparisons between non-tumour and tumour cellular
966 neighbourhood interactions (D) and densities (E). n = 16 HCC patients, each with non-tumour,
967 invasive margin, and tumour regions. A permutation student's t-test was done, p-values ≤0.1
968 are shown, mean is shown.

969

970 **Figure 5 – Cluster 44 consists of endothelial and VEGFA$^+$ perivascular macrophages**. A)
971 Cluster 44 (green) location indicated between non-tumour and tumour regions from the same
972 patient. Yellow arrows point towards the location of HLA-DR$^+$ CD34$^+$ cells (yellow). B)
973 Histograms showing relative marker expression for cluster 44 (red) compared to total cells
974 (grey). C) OPAL multiplex immunohistochemistry of tumour regions. HLA-DR (red), FXIIIA
975 (green), VEGFA (cyan), CD34 (purple), and DAPI (dark blue). Yellow arrows pointing to
976 white cells expressing HLA-DR, FXIIIA, and VEGFA. D) Ligand-receptor communication
977 between *CD34*$^+$ endothelial cells and *VEGFA*$^+$ macrophages. 10 patients with HCC and paired
978 non-tumour and tumour regions were used.

979

980 **Figure 6 – VEGFA$^+$ and VEGFA$^-$ perivascular macrophages preferentially reside in close**
981 **proximity to CD34$^+$ endothelial cells intratumourally in HCC**. A) Waterfall plot of number
982 of VEGFA$^+$ and VEGFA$^-$ macrophages proximity to CD34$^+$ endothelial cells, 20 µm
983 increments, range 0-100 µm. B) Number of VEGFA$^+$ macrophages in proximity to CD34$^+$
984 endothelial cells compared to non-endothelial cells (CD34$^-$ VEGFA$^-$), 20 µm increments,
985 range 100 µm. C) 4/8 HCC patients representative images of OPAL mIHC of HCC tumour
986 tissue stained for HLA-DR (red), FXIIIA (green), VEGFA (cyan), CD34 (magenta), and DAPI
987 (blue). Scale bar= 50 µm. 2-way ANOVA with Uncorrected Fisher's test was used, *$p<0.05$,
988 **$p<0.001$.

989

990 **Figure 7 – *VEGFA*$^+$ macrophages and *CD34*$^+$ endothelial cells have a ligand-receptor**
991 **communication via *VEGFA* within tumours**. A) Ligand-receptor communication between

992 *VEGFA*$^{+}$ macrophages (C48, ligand) and *CD34*$^{+}$ endothelial cells (C21, receptor) within
993 tumour. The single-cell RNA-sequencing (scRNA-seq) dataset consisted of paired non-tumour
994 and tumour regions from six HCC patients. The spatial transcriptomic dataset consisted of one
995 liver section from one HCC patient. B) Visualisation of the spatial transcriptomic data for
996 normal and HCC liver. *CD34*$^{+}$ endothelial cells are red, *VEGFA*$^{+}$ macrophages are blue. Close
997 cells (within 20 µm) are solid, whilst non-close cells are translucent. Other cell types are grey.
998 C) Quantification of relative levels of *CD34*$^{+}$ endothelial cells and *VEGFA*$^{+}$ macrophages in
999 the spatial transcriptomic dataset (n = 1).

1000

1001 **Figure 8 – Cluster 44 has a higher number of cellular neighbourhood interactions with**
1002 **clusters 9, 3, 8, and 35 within tumour compared to non-tumour**. A) Cluster 3 (CD3^{+} CD4^{+}
1003 cells, white arrows) and cluster 44 (CD34^{+} HLA-DR^{+} cells, yellow arrows) location indicated
1004 between non-tumour and tumour regions. B) Cluster 9 (CD8A^{+} cells, white arrows) and cluster
1005 44 (CD34^{+} HLA-DR^{+} cells, yellow arrows) location indicated between non-tumour and tumour
1006 regions. C) Histograms representing marker expression of cluster 3 (blue), cluster 9 (red), and
1007 total cells (grey). D) Cluster 8 (CD11c^{+} HLA-DR^{+}, yellow arrows) and cluster 44 (CD34^{+}
1008 HLA-DR^{+}, white arrows) location indicated between non-tumour and tumour regions. E)
1009 Cluster 35 (CD68^{+}, white arrows) and cluster 44 (CD34^{+} HLA-DR^{+}, yellow arrows) location
1010 indicated between non-tumour and tumour regions. F) Histograms representing marker
1011 expression of cluster 8 (blue), cluster 35 (red), and total cells (grey). Representative non-
1012 tumour and tumour regions are from the same patient.

1013

1014 **Figure 9 – Cellular neighbourhood interactions between clusters 8 and 9, and clusters 35**
1015 **and 45 are higher in tumour than non-tumour**. A) Cluster 8 (CD11c^{+} HLA-DR^{+}, yellow
1016 arrows) and cluster 9 (CD8A^{+}, white arrows) location indicated between non-tumour and
1017 tumour regions. B) Cluster 35 (CD14^{+} CD68^{+}, yellow arrows) and cluster 45 (CD14^{+} CD68^{+}
1018 FXIIIA^{+}, white arrows) location indicated between non-tumour and tumour regions. C)
1019 Histograms representing marker expression of cluster 45 (red) and total cells (grey).
1020 Representative non-tumour and tumour regions are from the same patient.

1021

1022 **Figure 10 – Summary figure**. Liver resections were collected from 16 patients with HCC to
1023 create a tissue microarray. Regions include non-tumour, invasive margin, and tumour, each
1024 collected in triplicate. Imaging mass cytometry was done on sections with a representative
1025 image shown. Within the tumour, a unique intratumoural perivascular-immune neighbourhood
1026 was identified, featuring cells as described.

1027

1028

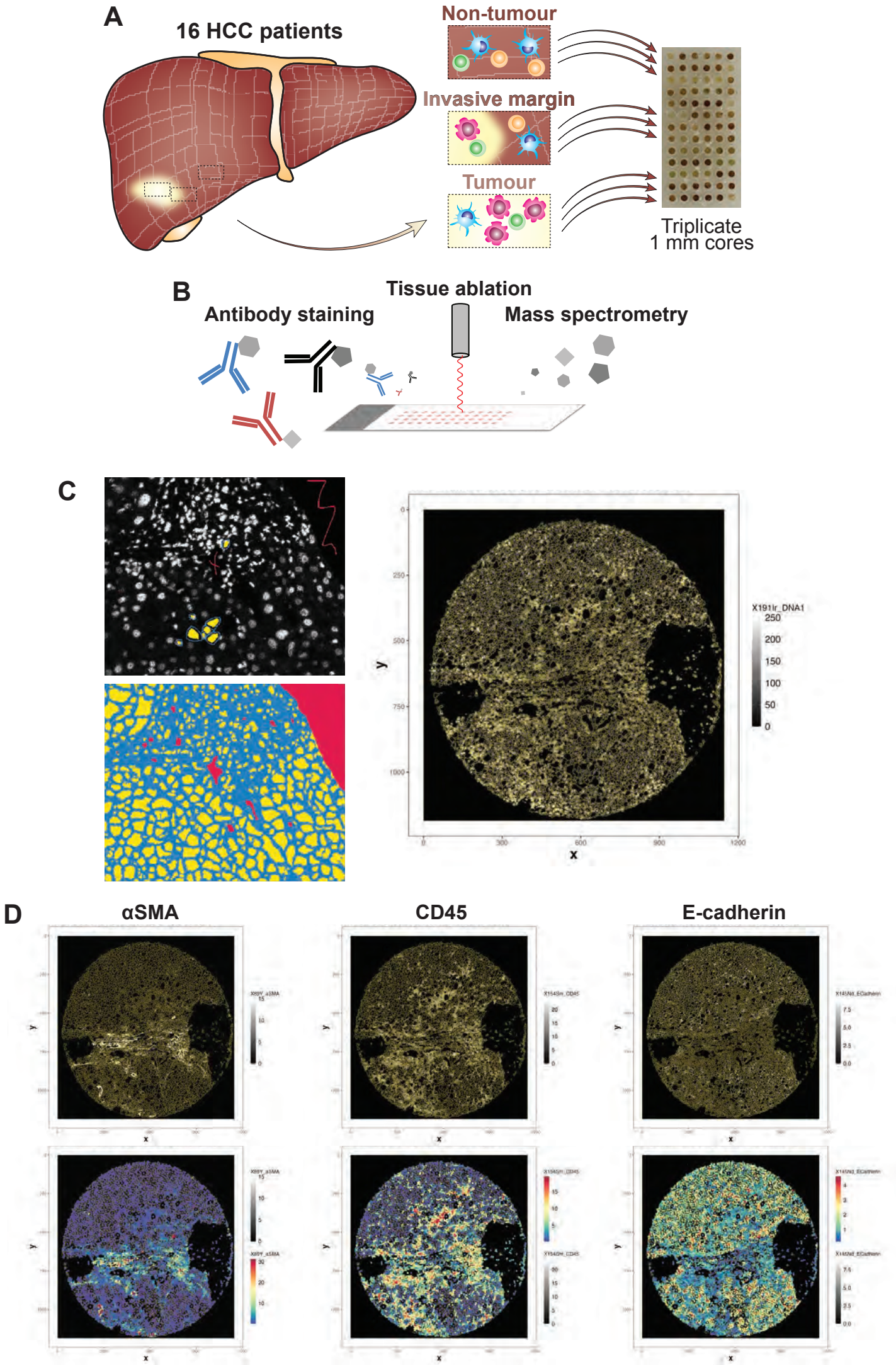
A
16 HCC patients
Non-tumour
Invasive margin
Tumour
Triplicate
1 mm cores
B
Antibody staining
Tissue ablation
Mass spectrometry
C
X191Ir_DNA1
250
200
150
100
50
0
y
x
D
αSMA
CD45
E-cadherin

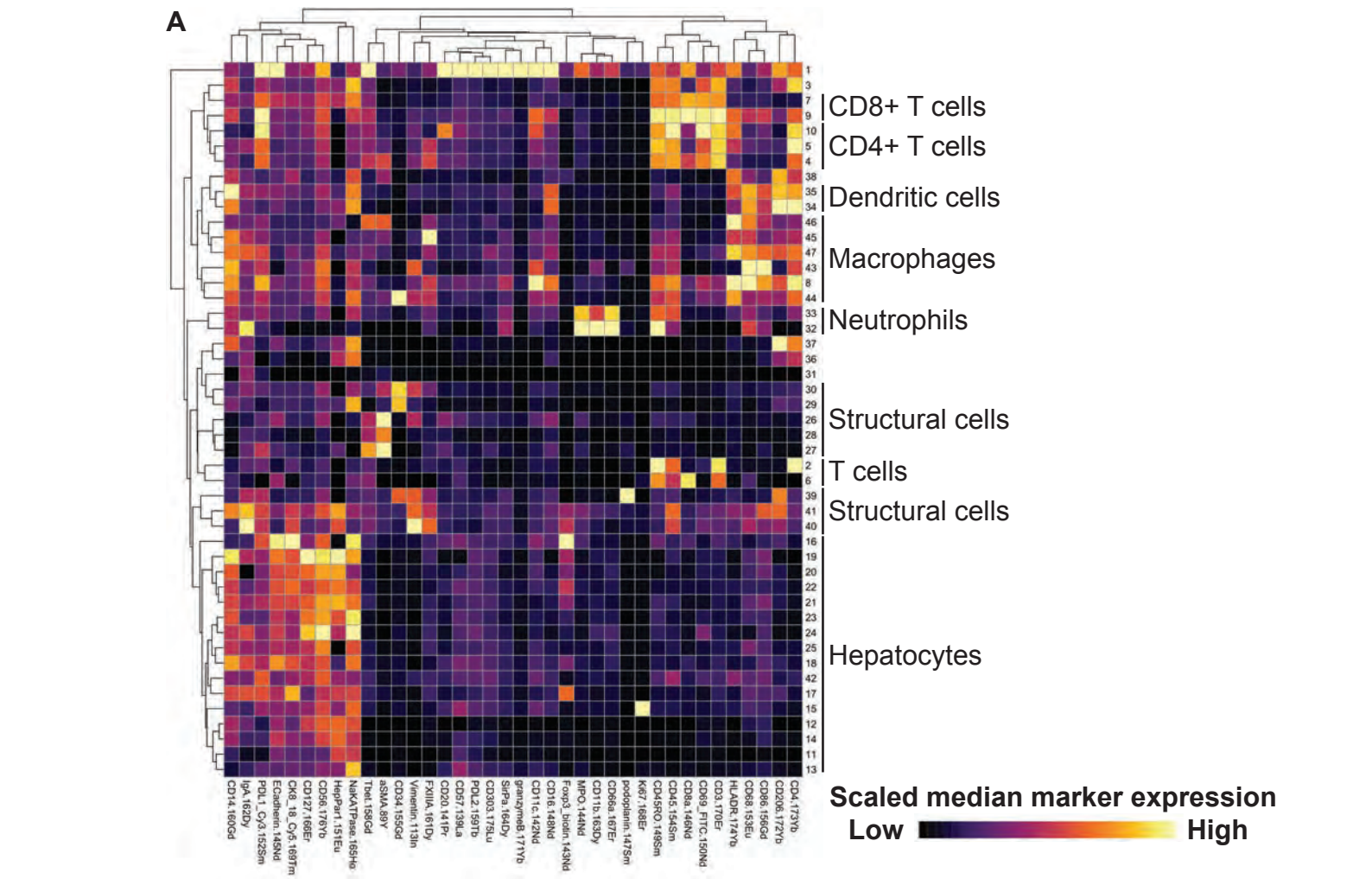

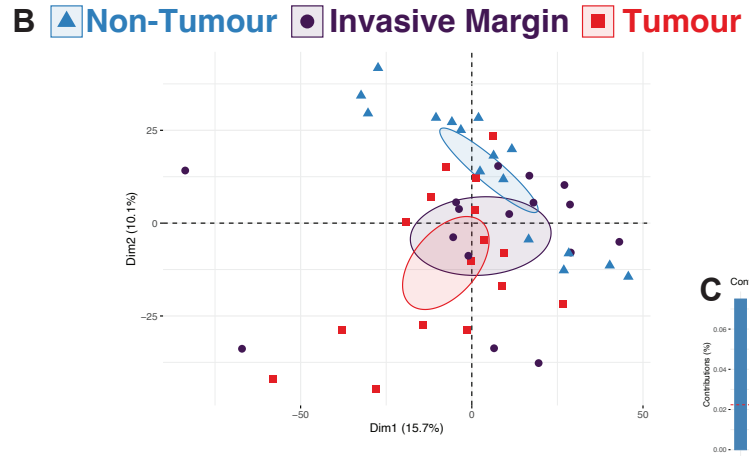

Group comparison	R^2	*P*-value
PERMANOVA	0.0700	***0.0030***
Invasive Margin vs Tumour	0.0393	0.2476
Non-Tumour vs Invasive Margin	0.0416	0.2476
Non-Tumour vs Tumour	0.0812	***0.0006***

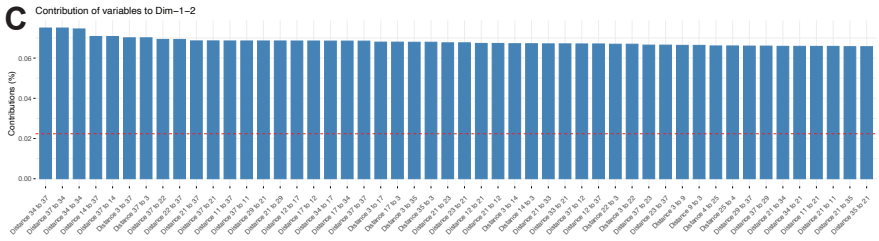

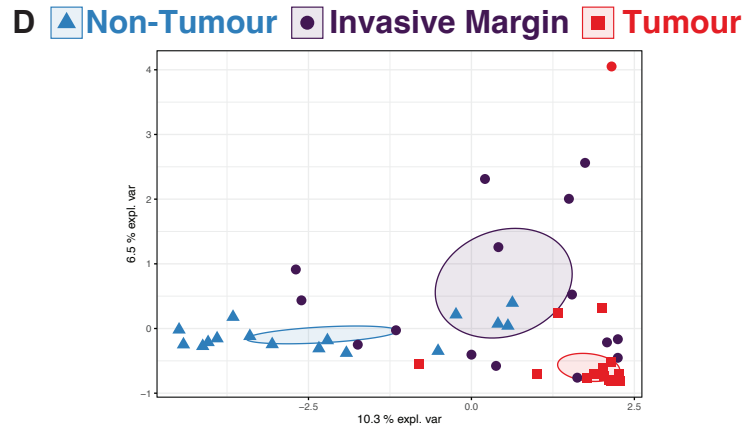

Group comparison	R^2	*P*-value
PERMANOVA	0.4362	***0.0004***
Invasive Margin vs Tumour	0.1957	***0.0008***
Non-Tumour vs Invasive Margin	0.2785	***0.0008***
Non-Tumour vs Tumour	0.5417	***0.0006***

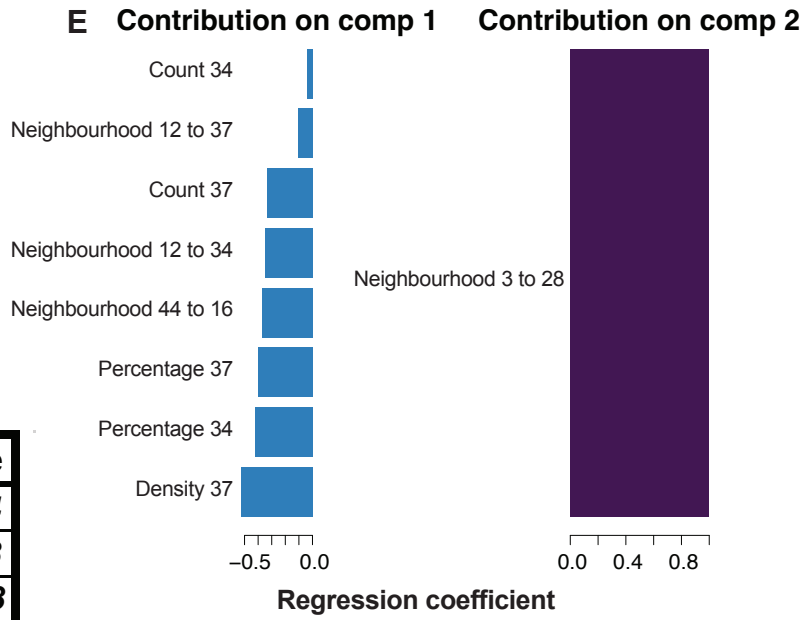

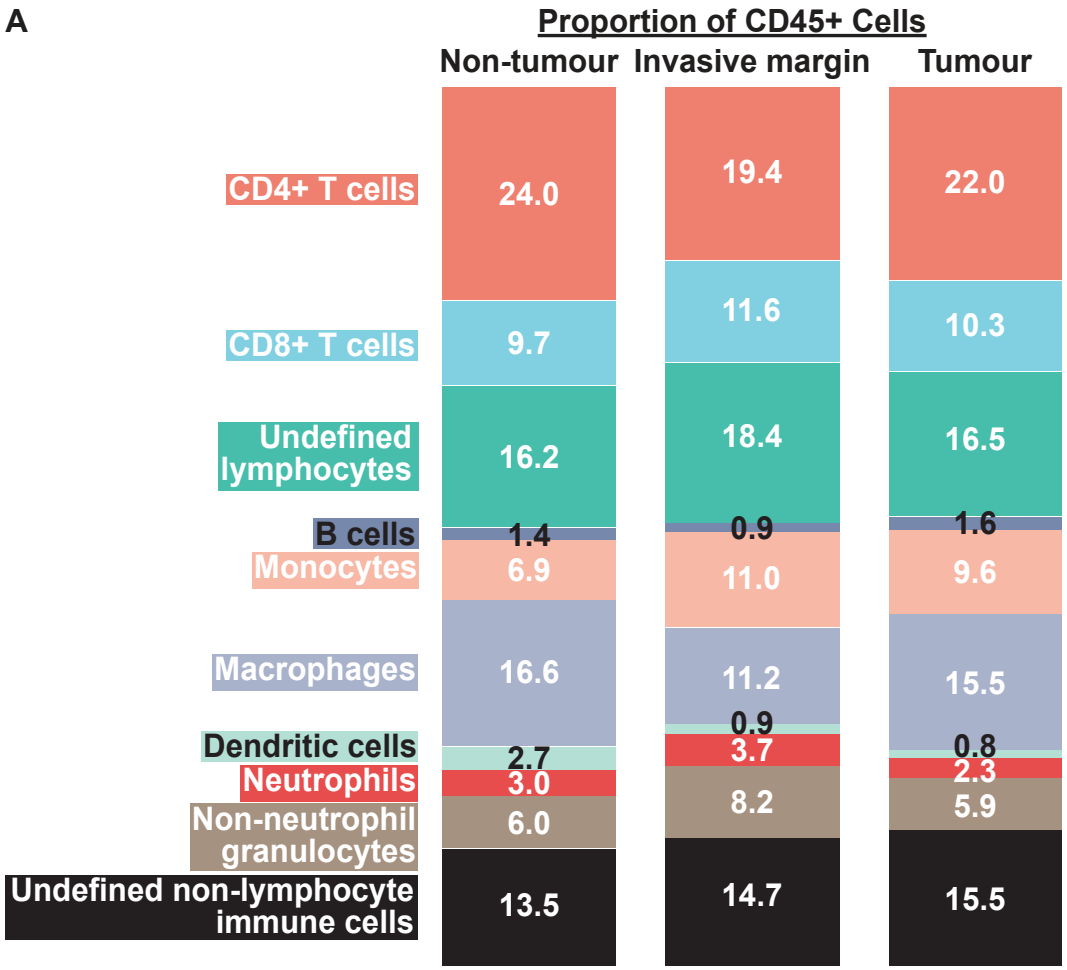
A
Proportion of CD45+ Cells
Non-tumour
Invasive margin
Tumour
CD4+ T cells
24.0
19.4
22.0
CD8+ T cells
9.7
11.6
10.3
Undefined lymphocytes
16.2
18.4
16.5
B cells
1.4
0.9
1.6
Monocytes
6.9
11.0
9.6
Macrophages
16.6
11.2
15.5
Dendritic cells
2.7
0.9
0.8
Neutrophils
3.0
3.7
2.3
Non-neutrophil granulocytes
6.0
8.2
5.9
Undefined non-lymphocyte immune cells
13.5
14.7
15.5

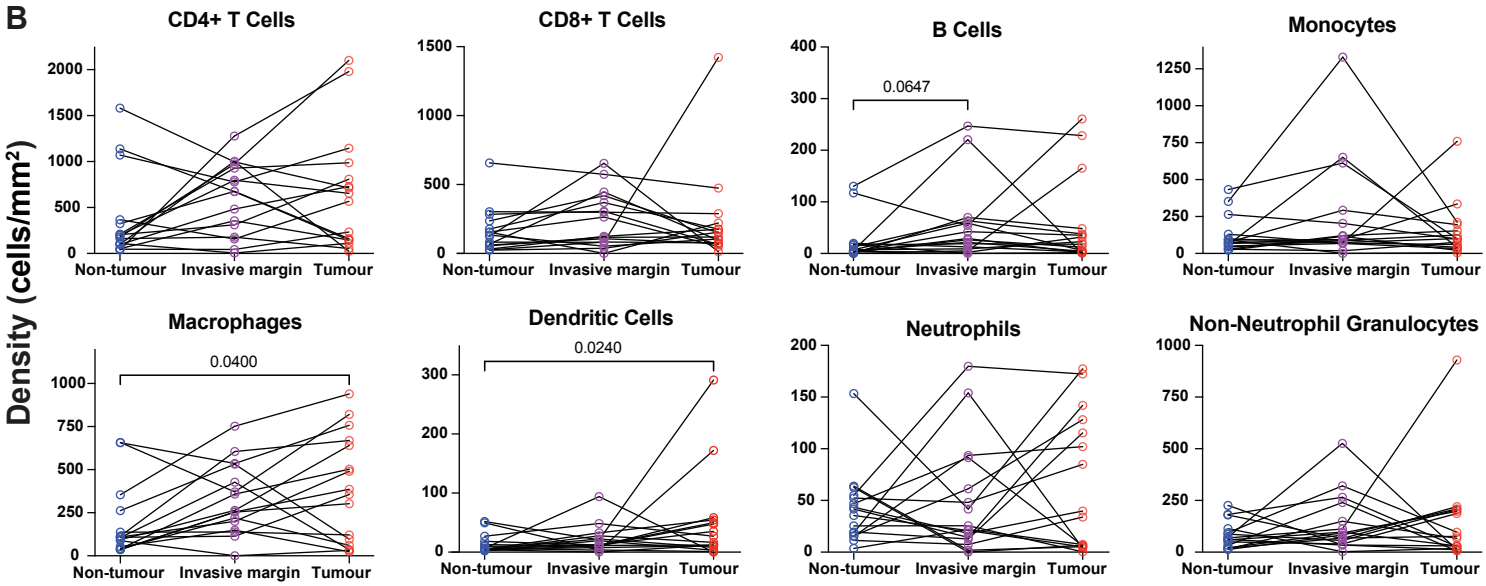
B
Density (cells/mm²)
CD4+ T Cells
CD8+ T Cells
B Cells
0.0647
Monocytes
Macrophages
0.0400
Dendritic Cells
0.0240
Neutrophils
Non-Neutrophil Granulocytes
Non-tumour
Invasive margin
Tumour

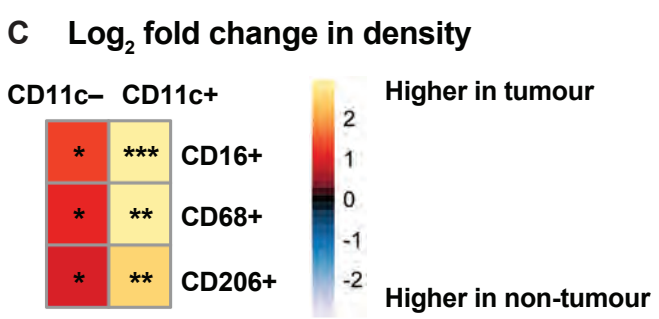
C
Log2 fold change in density
CD11c–
CD11c+
CD16+
CD68+
CD206+
*
***
**
Higher in tumour
Higher in non-tumour
2
1
0
-1
-2

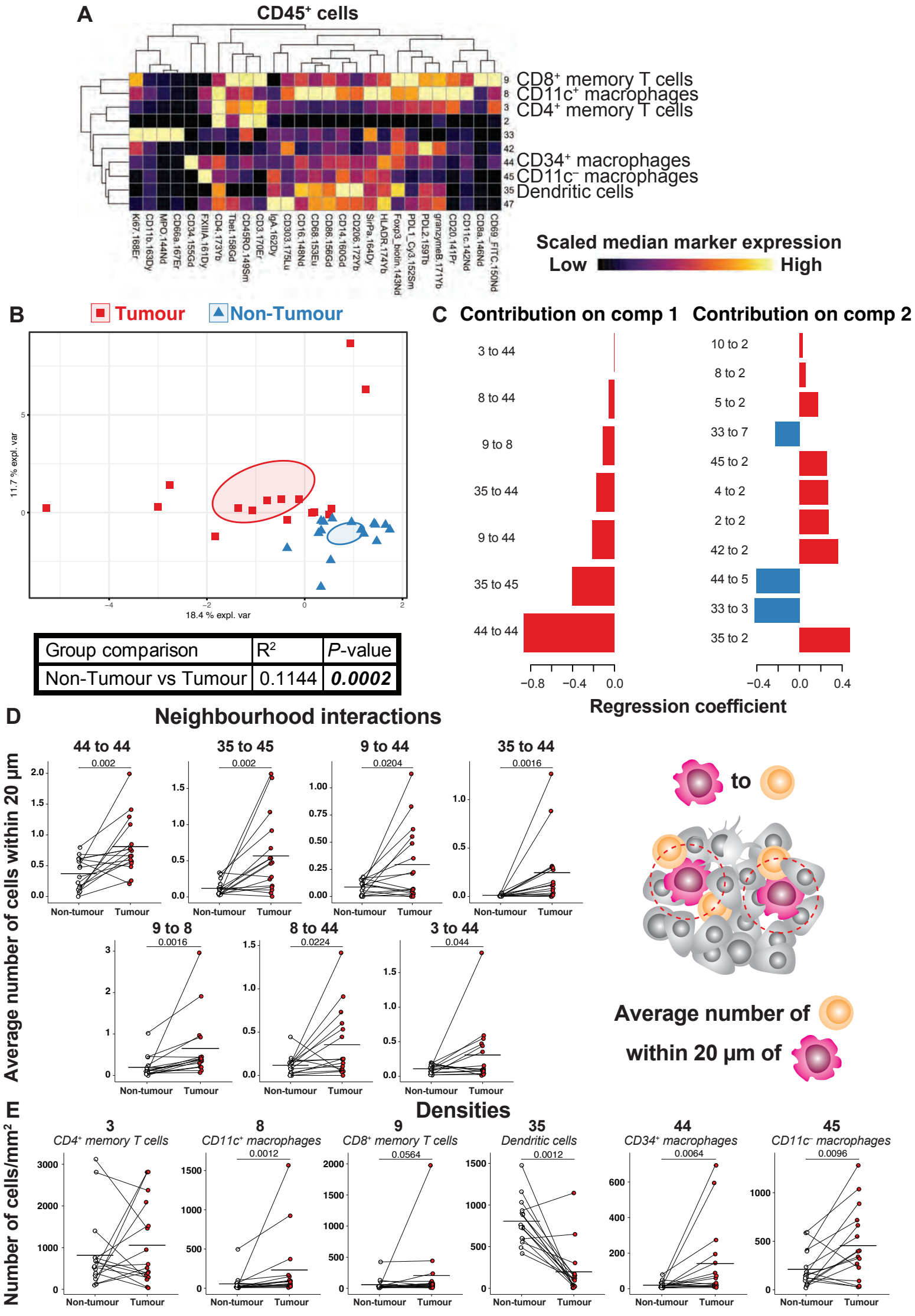

Group comparison	R^2	*P*-value
Non-Tumour vs Tumour	0.1144	***0.0002***

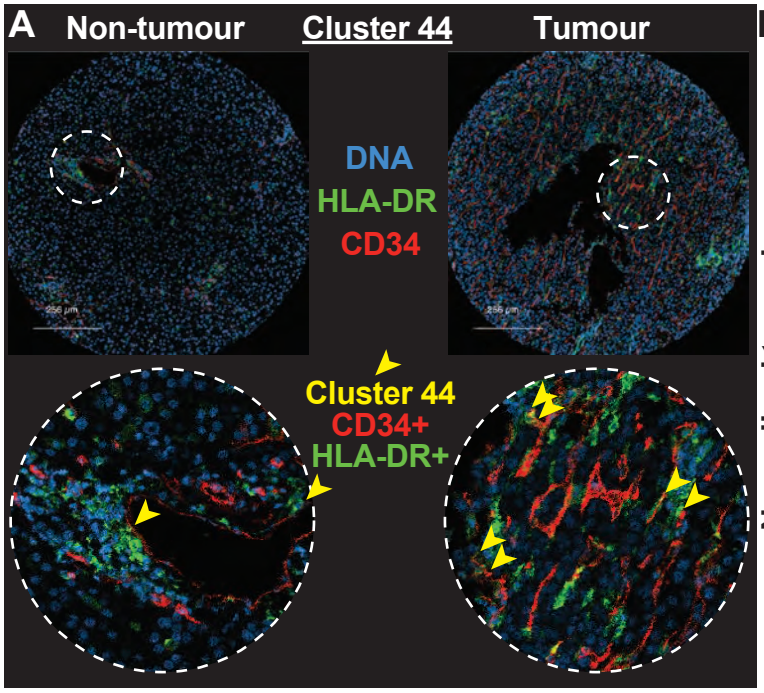

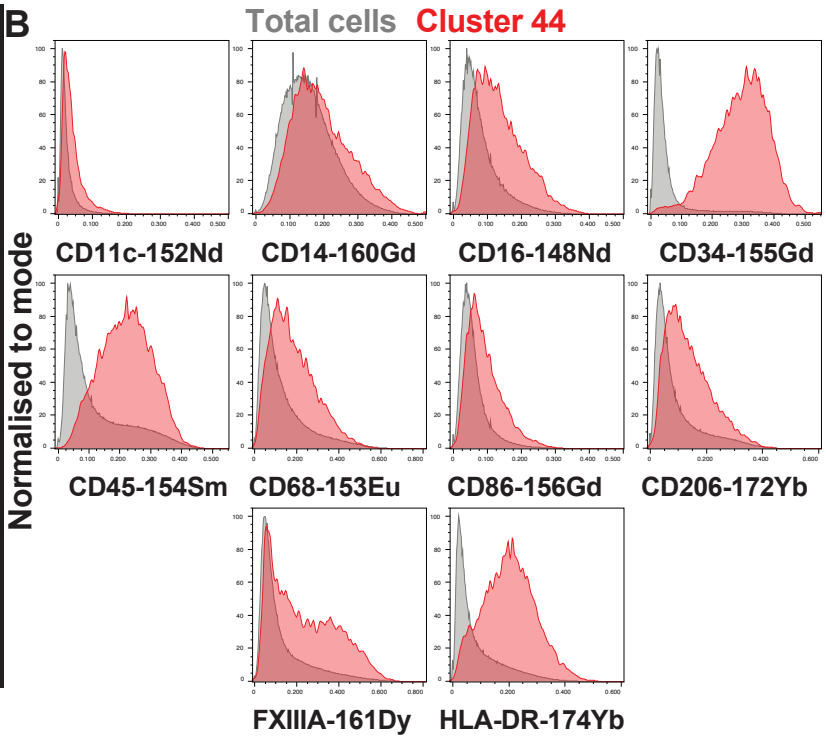

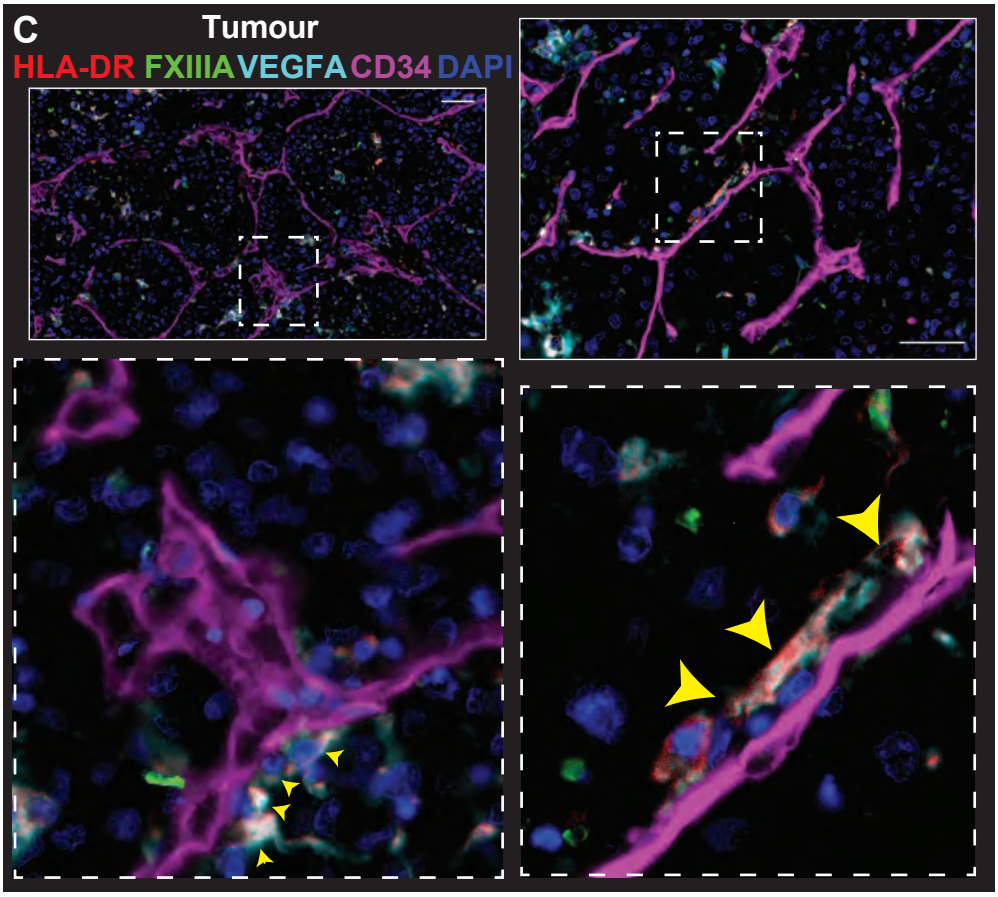

D *CD34*⁺ endothelial cell (C48) as ligand

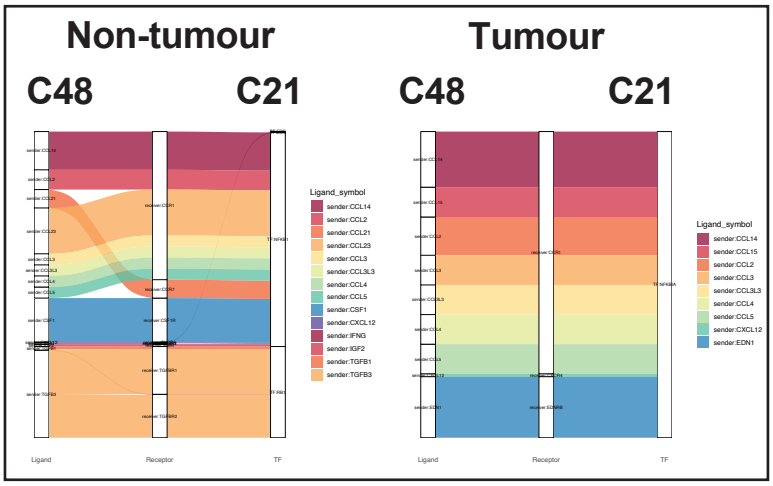

VEGFA⁺ macrophage (C21) as ligand

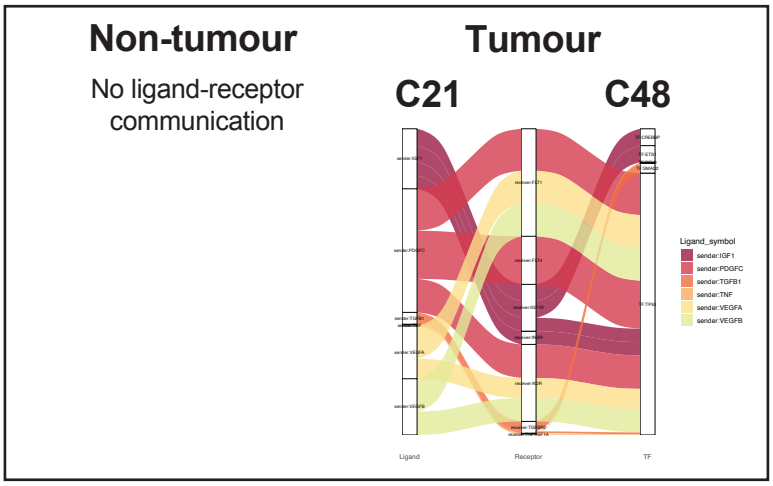

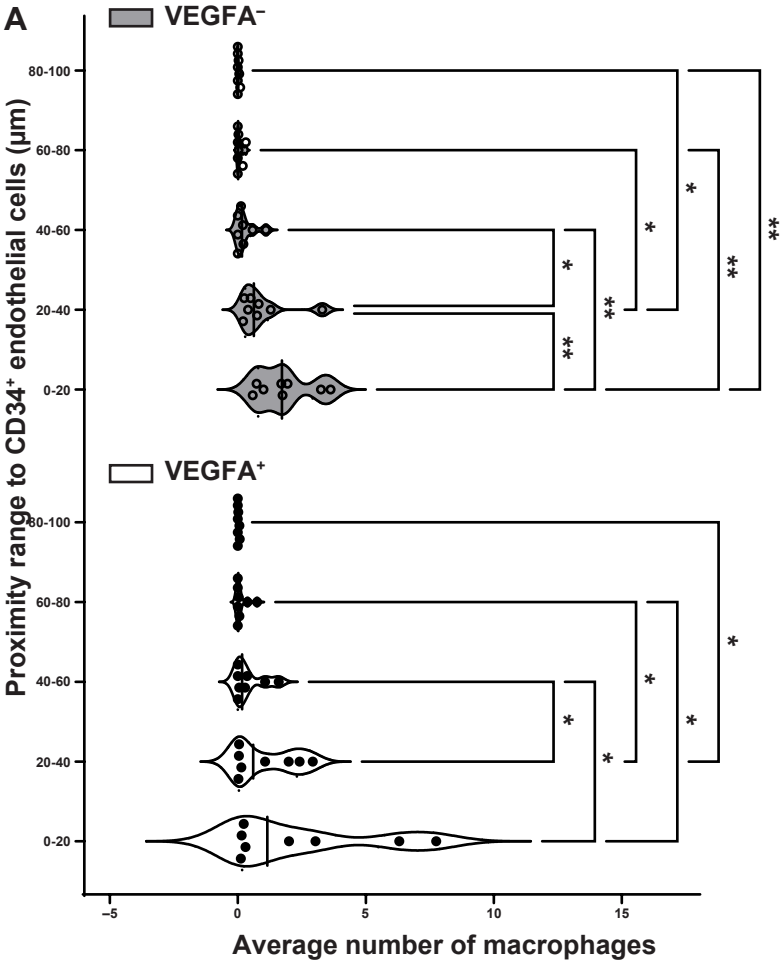
A
VEGFA⁻
VEGFA⁺
Proximity range to CD34⁺ endothelial cells (µm)
80-100
60-80
40-60
20-40
0-20
−5
0
5
10
15
Average number of macrophages
*
**

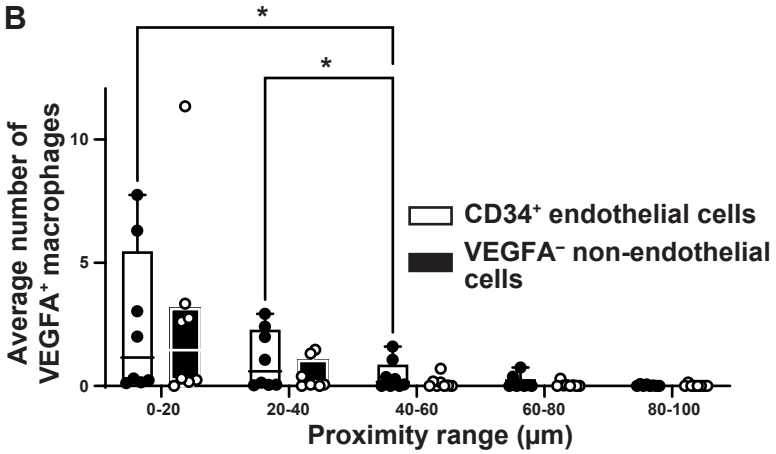
B
Average number of VEGFA⁺ macrophages
0
5
10
0-20
20-40
40-60
60-80
80-100
Proximity range (µm)
CD34⁺ endothelial cells
VEGFA⁻ non-endothelial cells
*

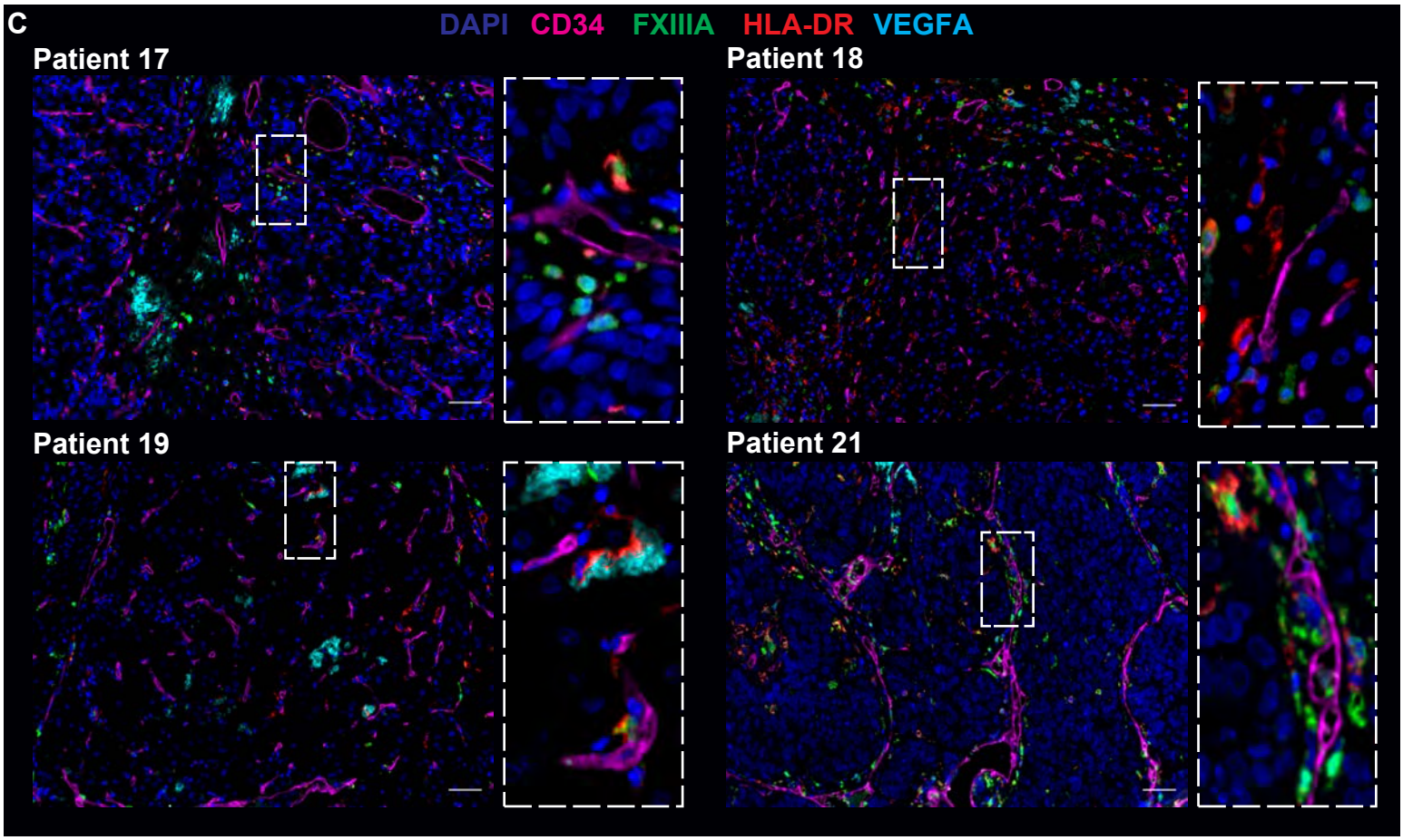
C
DAPI CD34 FXIIIA HLA-DR VEGFA
Patient 17
Patient 18
Patient 19
Patient 21

A **Tumour**

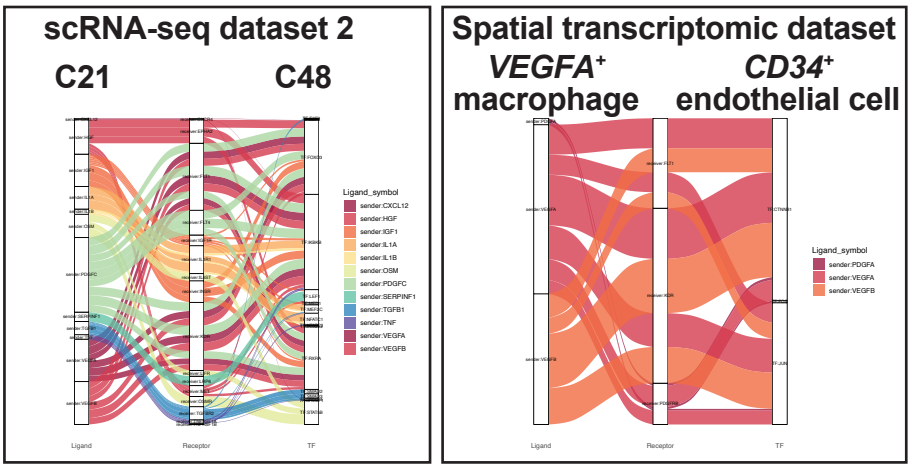

B Cell coordinates in XY space

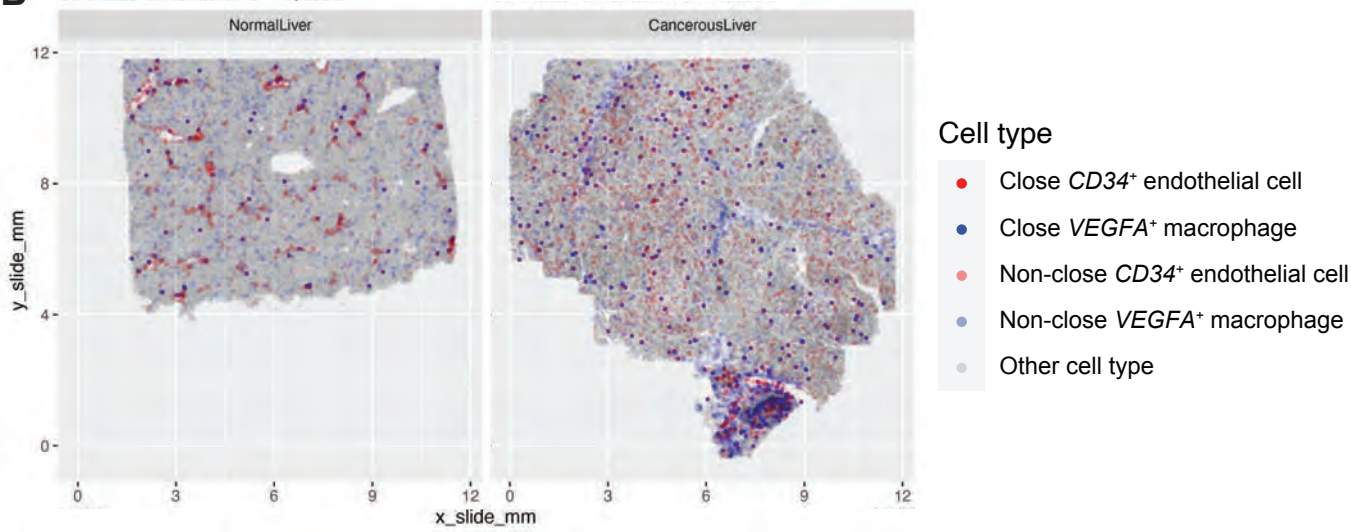

C

Subset density (cells/mm^2)	Normal	HCC
VEGFA$^+$ macrophages	26.34	36.27
Close *VEGFA*$^+$ macrophages	1.26	3.65
CD34$^+$ endothelial cells	26.75	46.61
Close *CD34*$^+$ endothelial cells	1.51	4.04

Subset proportions	Normal	HCC
Close *VEGFA*$^+$ macrophages (%*VEGFA*$^+$ macrophages)	4.80%	10.1%
Close *CD34*$^+$ endothelial cells (%*CD34*$^+$ endothelial cells)	5.66%	8.67%

Average number within 20 μm	Normal	HCC
Macrophage to endothelial cell	0.060	0.132
Endothelial cell to macrophage	0.055	0.088

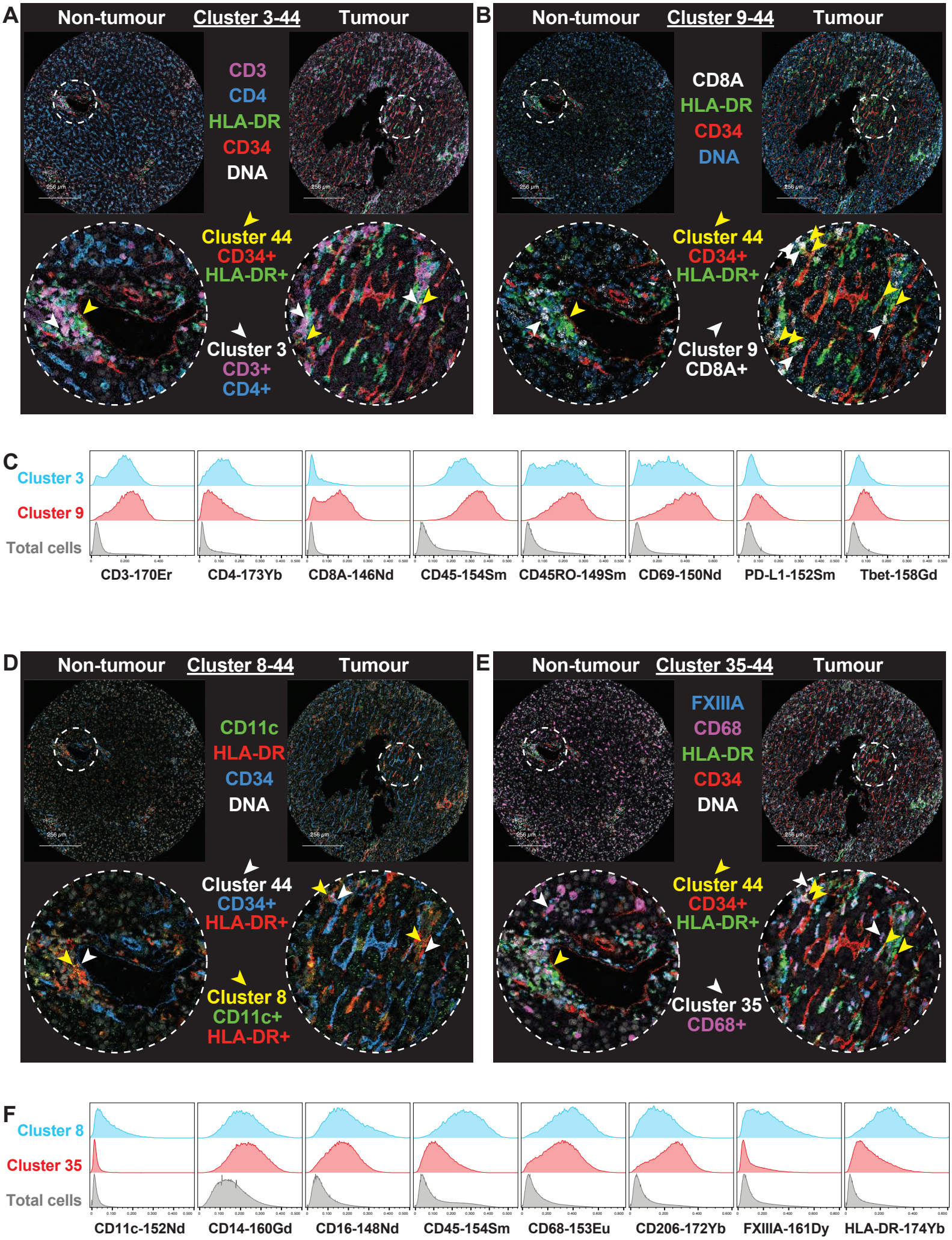
A
Non-tumour
Cluster 3-44
Tumour
CD3
CD4
HLA-DR
CD34
DNA
Cluster 44
CD34+
HLA-DR+
Cluster 3
CD3+
CD4+
B
Non-tumour
Cluster 9-44
Tumour
CD8A
HLA-DR
CD34
DNA
Cluster 44
CD34+
HLA-DR+
Cluster 9
CD8A+
C
Cluster 3
Cluster 9
Total cells
CD3-170Er
CD4-173Yb
CD8A-146Nd
CD45-154Sm
CD45RO-149Sm
CD69-150Nd
PD-L1-152Sm
Tbet-158Gd
D
Non-tumour
Cluster 8-44
Tumour
CD11c
HLA-DR
CD34
DNA
Cluster 44
CD34+
HLA-DR+
Cluster 8
CD11c+
HLA-DR+
E
Non-tumour
Cluster 35-44
Tumour
FXIIIA
CD68
HLA-DR
CD34
DNA
Cluster 44
CD34+
HLA-DR+
Cluster 35
CD68+
F
Cluster 8
Cluster 35
Total cells
CD11c-152Nd
CD14-160Gd
CD16-148Nd
CD45-154Sm
CD68-153Eu
CD206-172Yb
FXIIIA-161Dy
HLA-DR-174Yb

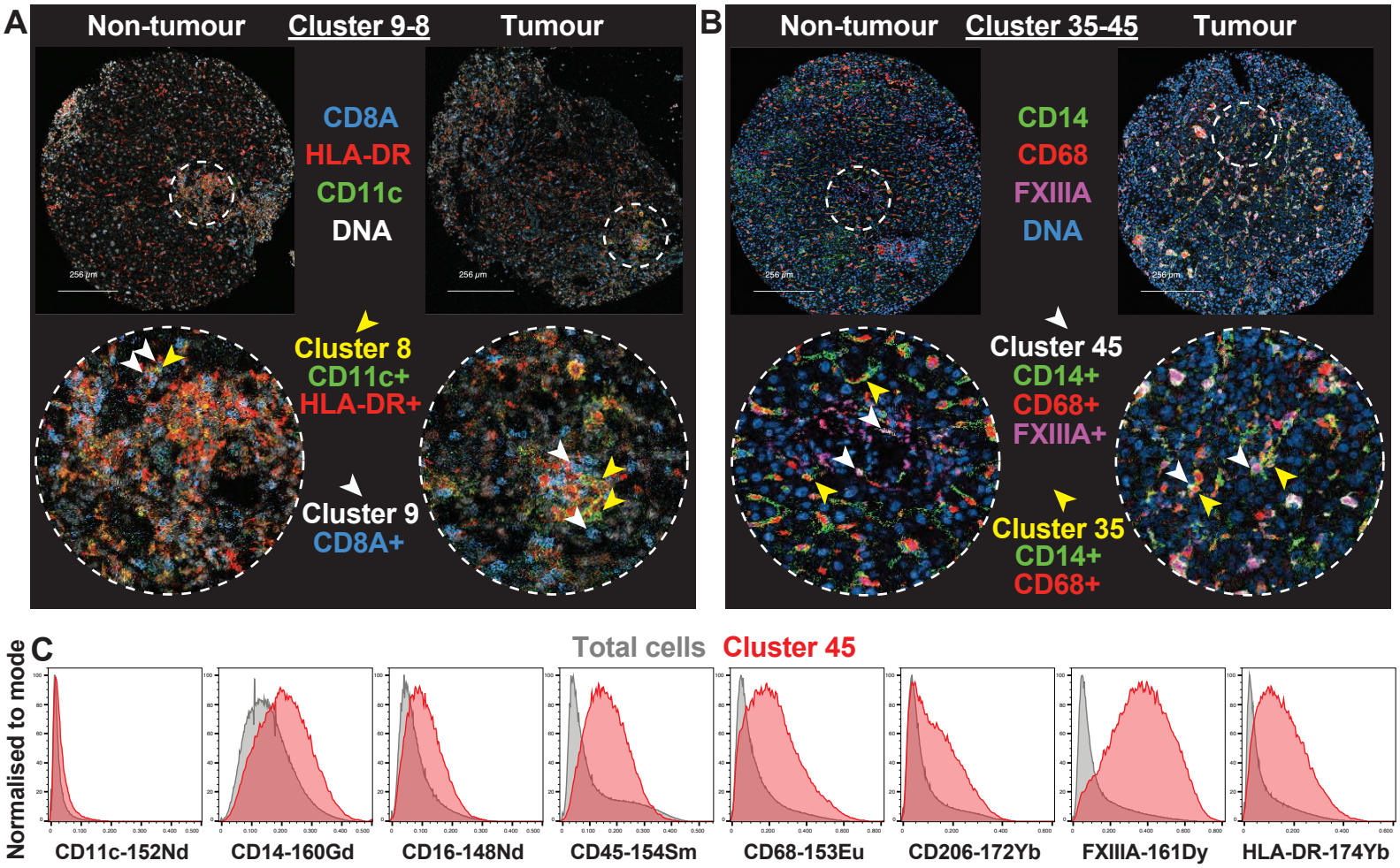
A
Non-tumour
Cluster 9-8
Tumour
CD8A
HLA-DR
CD11c
DNA
256 µm
Cluster 8
CD11c+
HLA-DR+
Cluster 9
CD8A+
B
Non-tumour
Cluster 35-45
Tumour
CD14
CD68
FXIIIA
DNA
Cluster 45
CD14+
CD68+
FXIIIA+
Cluster 35
CD14+
CD68+
C
Total cells
Cluster 45
Normalised to mode
CD11c-152Nd
CD14-160Gd
CD16-148Nd
CD45-154Sm
CD68-153Eu
CD206-172Yb
FXIIIA-161Dy
HLA-DR-174Yb

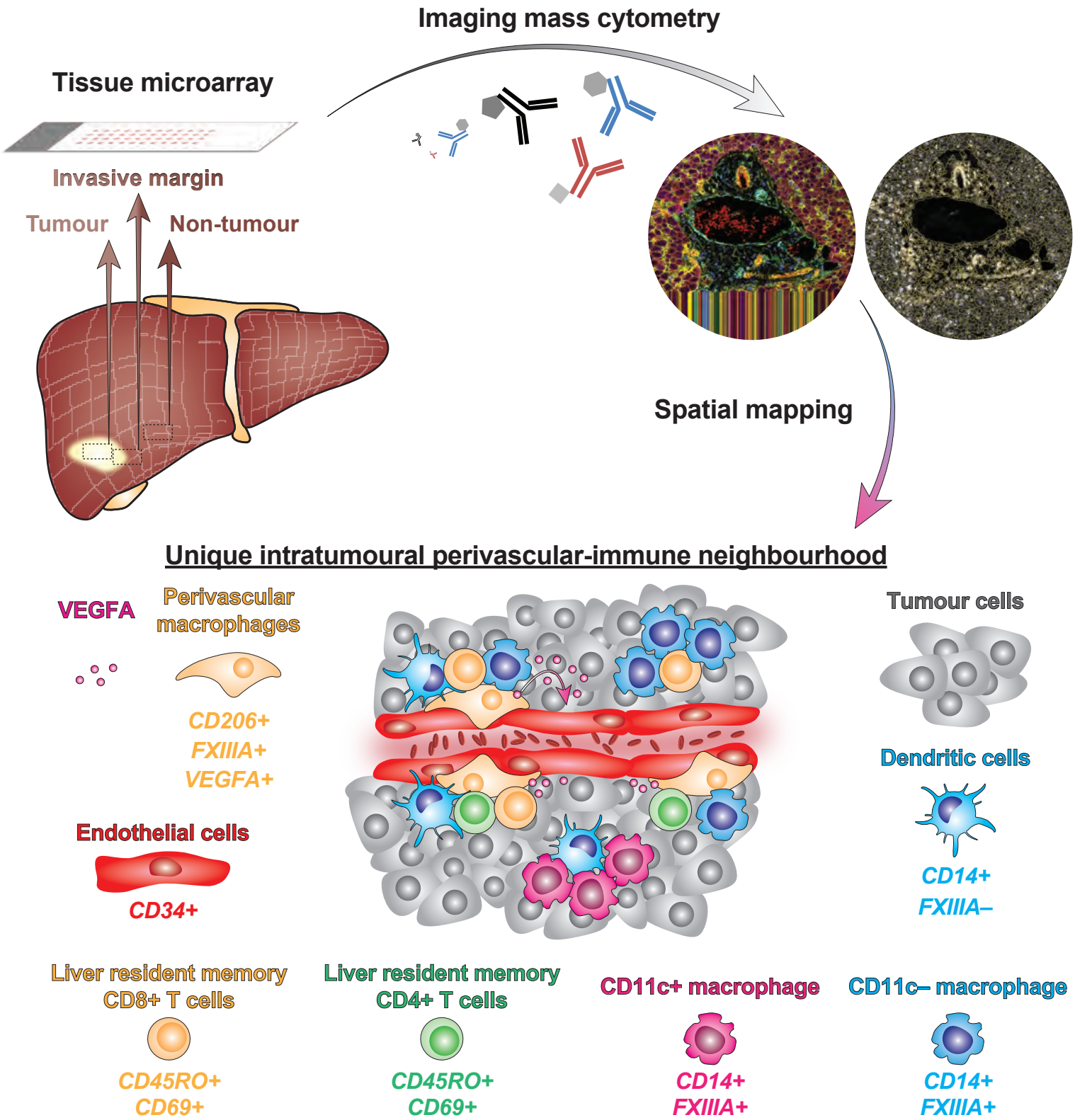
Imaging mass cytometry
Tissue microarray
Invasive margin
Tumour
Non-tumour
Spatial mapping
Unique intratumoural perivascular-immune neighbourhood
VEGFA
Perivascular macrophages
CD206+
FXIIIA+
VEGFA+
Endothelial cells
CD34+
Tumour cells
Dendritic cells
CD14+
FXIIIA–
Liver resident memory CD8+ T cells
CD45RO+
CD69+
Liver resident memory CD4+ T cells
CD45RO+
CD69+
CD11c+ macrophage
CD14+
FXIIIA+
CD11c– macrophage
CD14+
FXIIIA+

Supplementary figure legends

Supplementary Figure 1 – Single marker IMC staining. Representative images for individual IMC antibodies.

Supplementary Figure 2 – Single marker OPAL staining. Representative images for individual OPAL antibodies.

Supplementary Figure 3 – Manual gating strategy of immune cell subsets. Representative gating strategy identifying immune cell subsets.

Supplementary Figure 4 – Clustering of single cells. A) Total cells were clustered using X-shift. B) The median signal intensity of CD45 was calculated for each cluster before running z-score normalisation. Red vertical line is at zero, whereby a negative cluster indicates no CD45 expression, whilst a positive value indicates CD45 expression. The blue line represents the absolute value of the smallest value, used to differentiate between $CD45^{low}$ and $CD45^{hi}$ populations. C) Cells then underwent X-shift clustering within each of the three groups ($CD45^{-}$, $CD45^{low}$, $CD45^{hi}$) resulting in 91, 36, and 18 clusters respectively. Similar clusters were then combined using the function simprof as part of the 'clustsig' R package, generating 47 clusters (20 $CD45^{+}$ clusters and 27 $CD45^{-}$ clusters). D) The number of $CD45^{+}$ clusters with ≥5 cells in each region were calculated. Clusters with <5 cells across less than a third of total regions were excluded, which removed six clusters. Heatmaps show the scaled median signal expression of each marker (columns) across each cluster (rows).

Supplementary Figure 5 – scANVI cluster annotation transfer. Cluster annotations were transferred from initial single-cell RNA-sequencing (scRNA-seq) dataset (GSE149614) to a second scRNA-seq dataset (https://data.mendeley.com/datasets/skrx2fz79n/1). A) UMAP visualising the integrated original reference dataset (orange) with the second dataset (blue). B) UMAP of predicted annotated clusters.

Supplementary Figure 6 – T cell and myeloid cell subset levels across regions. A) Densities of T cell subsets across regions. B) Densities of $CD4^+$ T cell subsets. Friedman test with Dunn's multiple comparison corrections was done. C) Densities of $CD14^-$ non-monocyte-derived macrophages across regions. D) Density and proportions (% of $CD45^+$ cells or total cells) across myeloid cell subsets. Wilcoxon test was used.

Supplementary Figure 7 – Phenotypically similar clusters were combined. $CD45^+$ clusters that were phenotypically similar were combined. Representative images show each cluster (red) compared to total cells (grey).

Supplementary Figure 8 – Representative images of parameters that contributed to differences between non-tumour and tumour regions. Representative images of cluster results on segmented data (green, dark blue, dark red dots). Images of imaging mass cytometry with markers and clusters as indicated.

Supplementary Figure 9 –T cell marker expression. A) Representative image of CD4 (red) and CD8A (green) staining. B) Plot showing cluster 3 (blue, $CD4^+$ T cells), cluster 9 (red, $CD8^+$ T cells), and total cells (grey) against CD4 and CD8 staining. C) Plots showing cluster 3 (blue, $CD4^+$ T cells), cluster 9 (red, $CD8^+$ T cells), and total cells (grey) for PD-L1 and T-bet expression.

Supplementary Figure 10 – No association between clinical parameters and tumour neighbourhood interaction. Tumour neighbourhood interactions were correlated with A) cirrhosis, B) early recurrence (<2 years), C) microvascular invasion (MVI), and D) viral-associated HCC. Permutation student's t-test.

Supplementary Figure 1 (page 1/5)

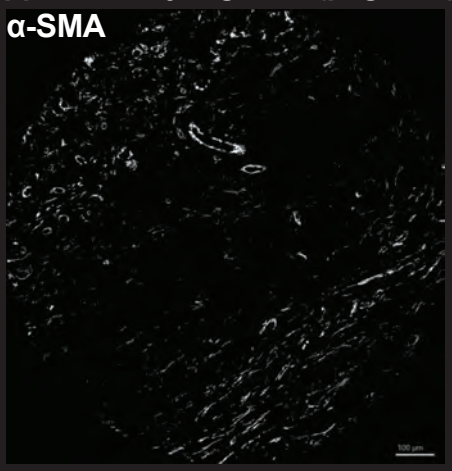

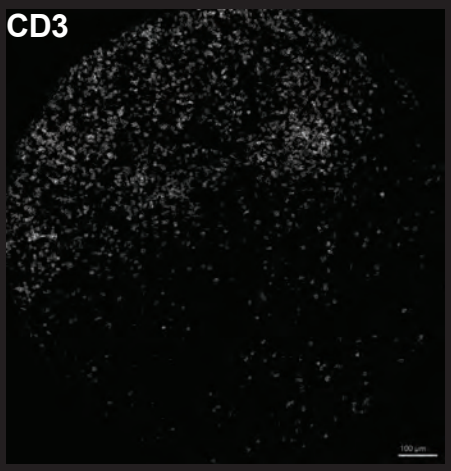

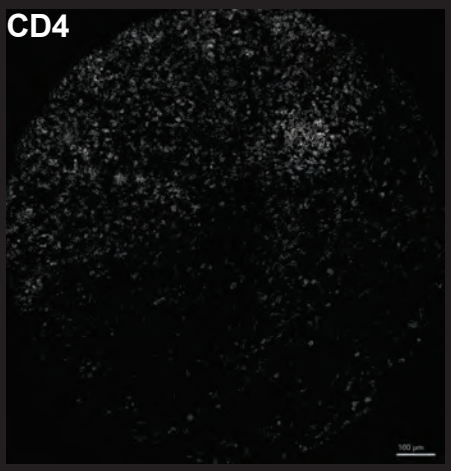

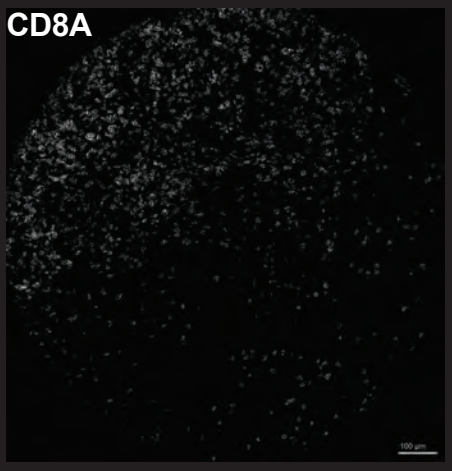

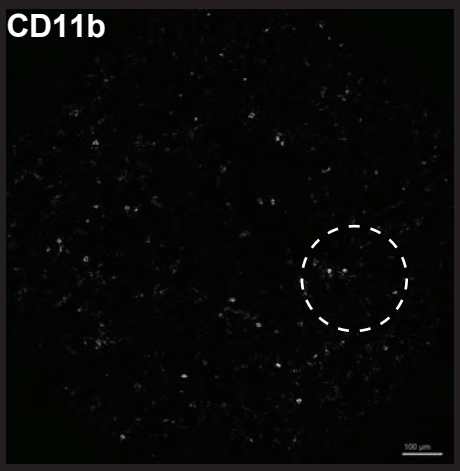

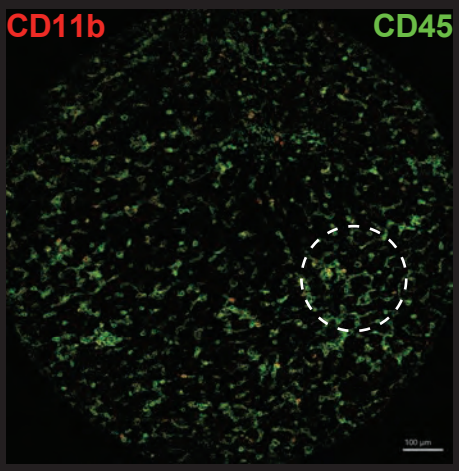

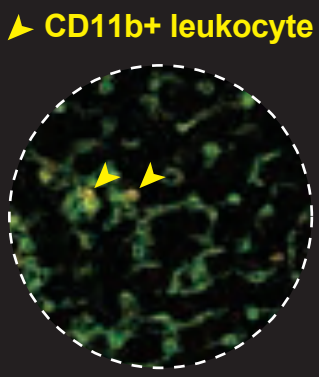

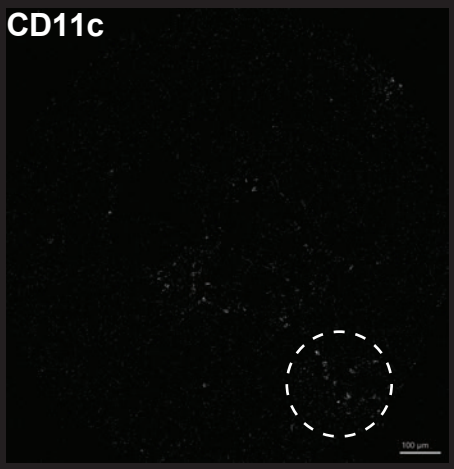

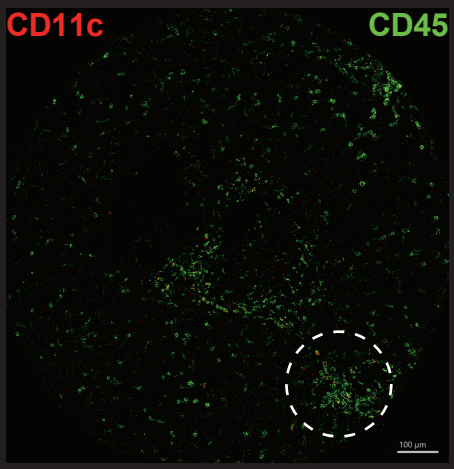

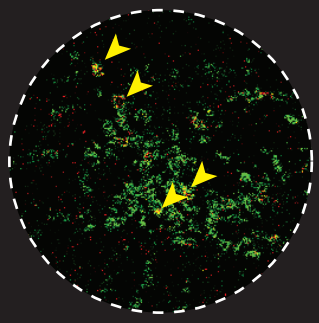

Supplementary Figure 1 (page 2/5)

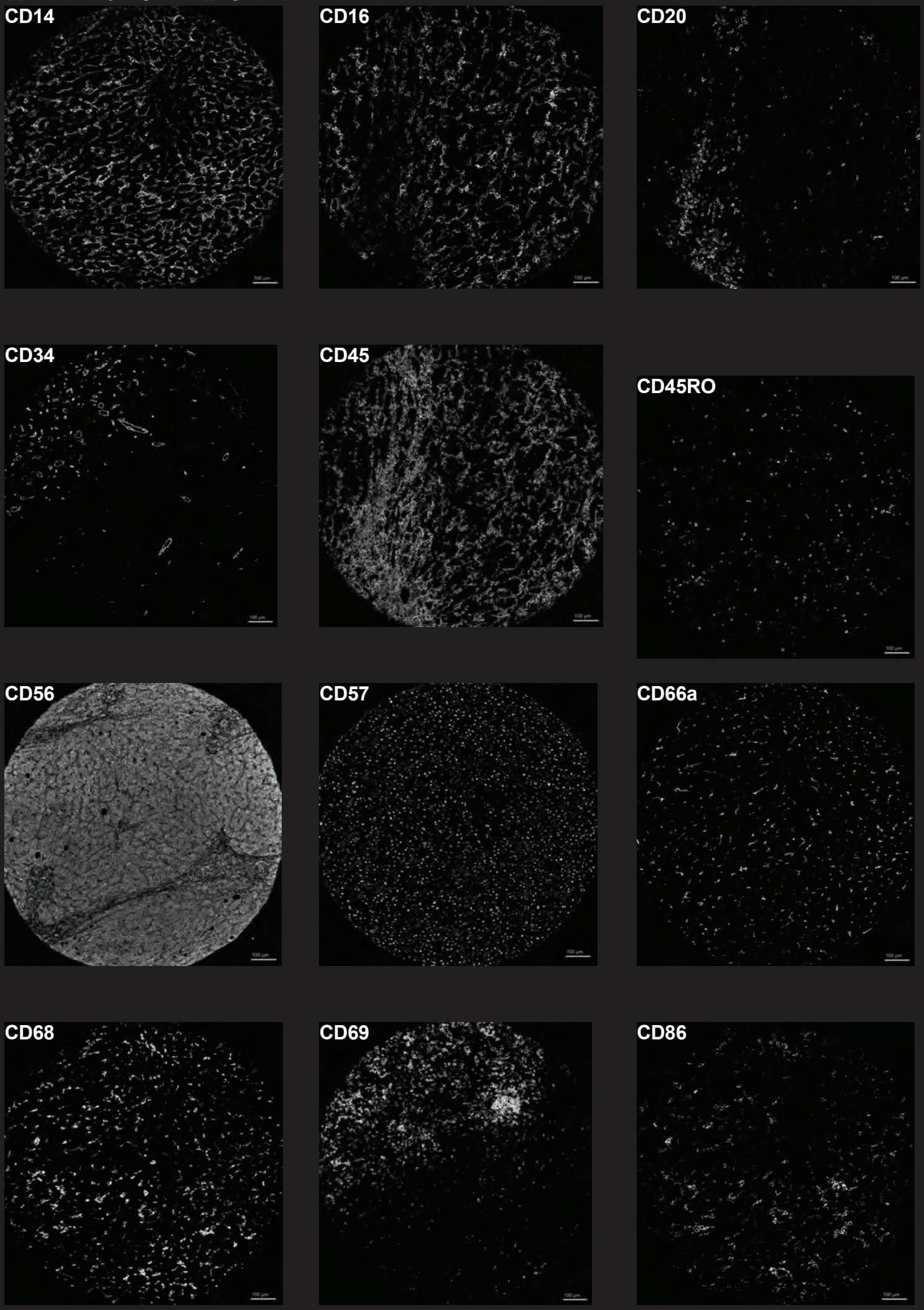

Supplementary Figure 1 (page 3/5)

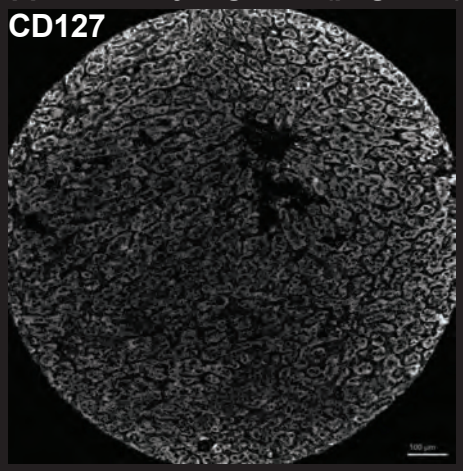

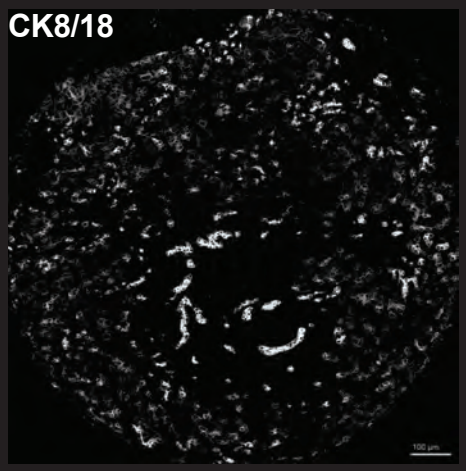

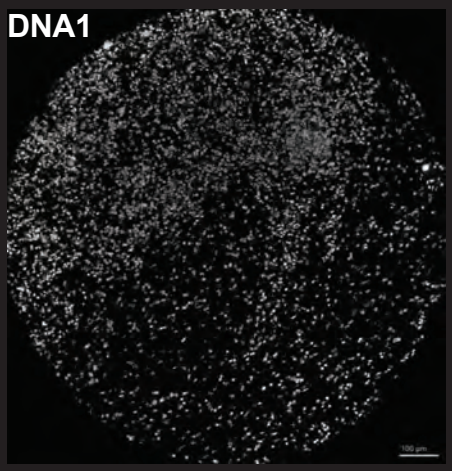

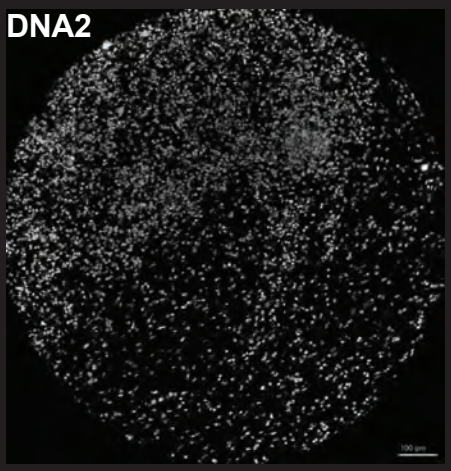

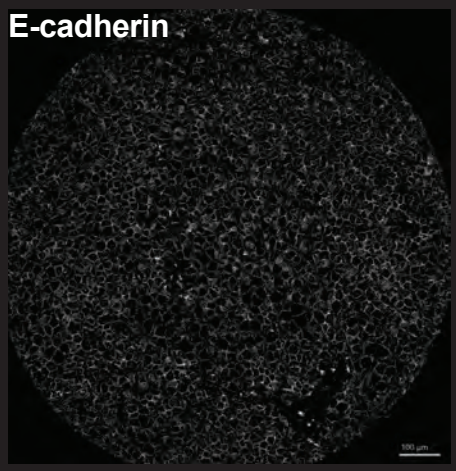

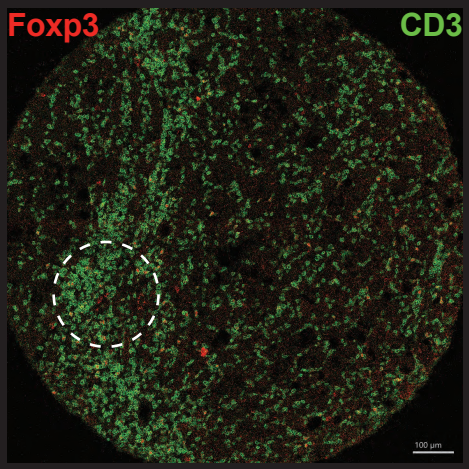

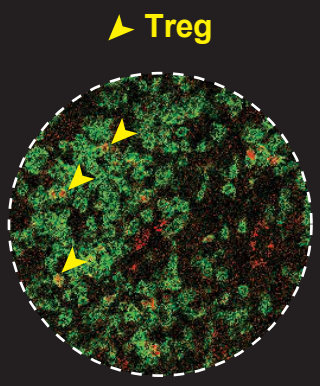

Supplementary Figure 1 (page 4/5)

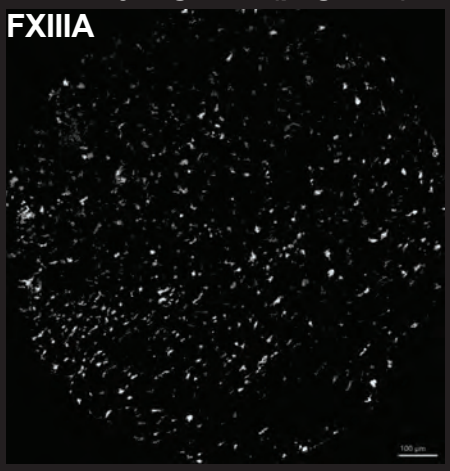

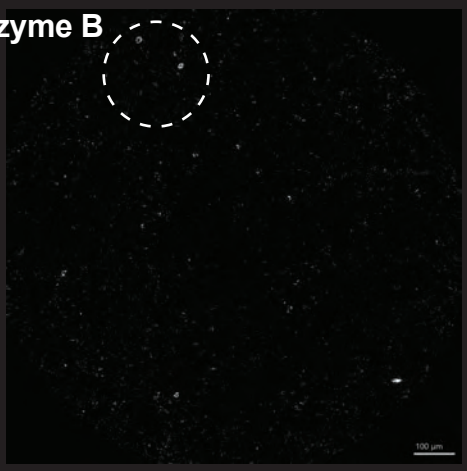

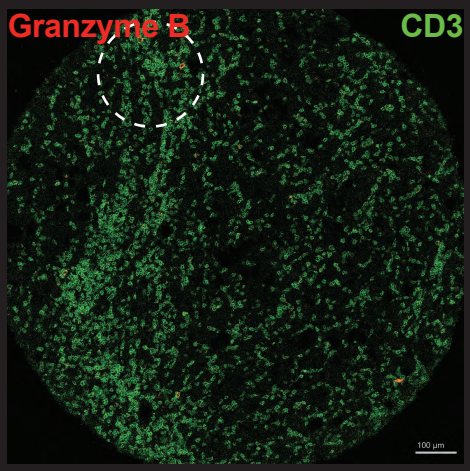

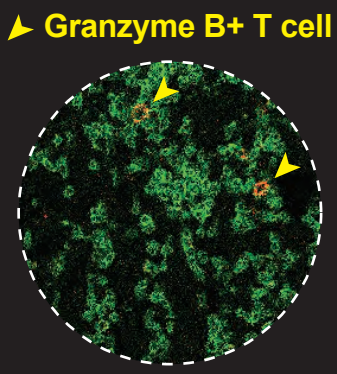

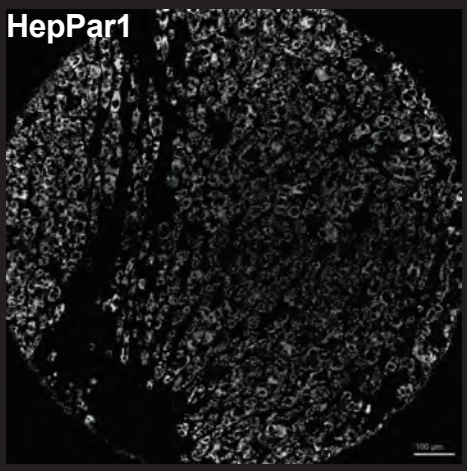

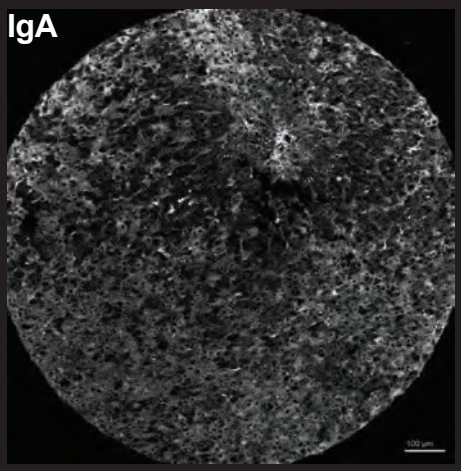

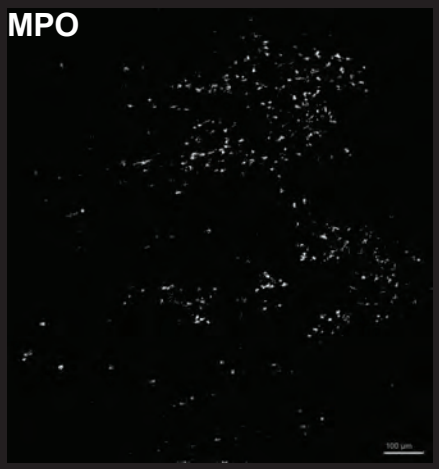

Supplementary Figure 1 (page 5/5)

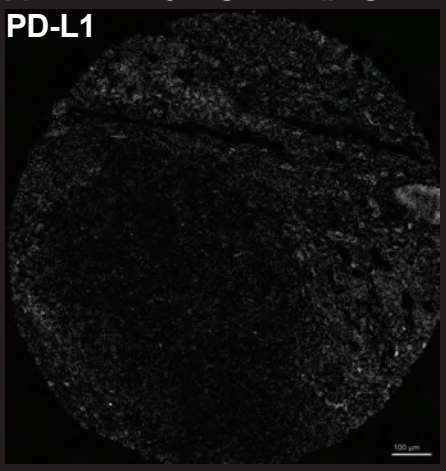

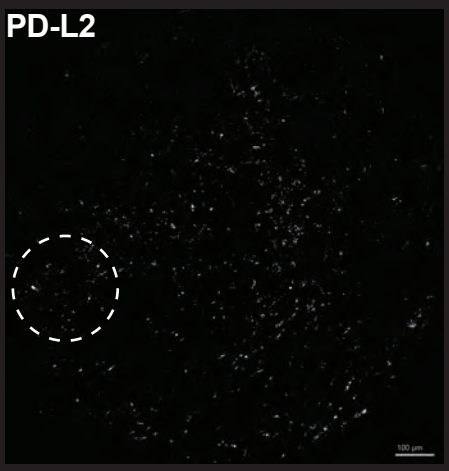

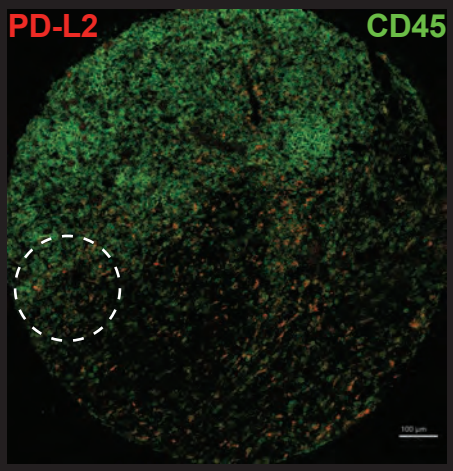

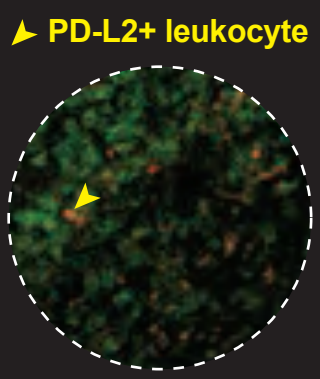

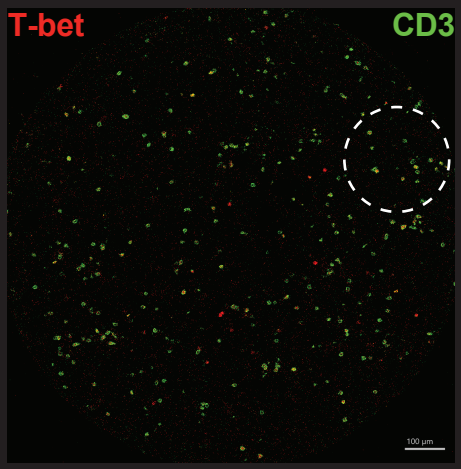

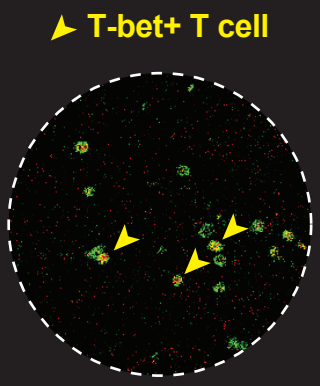

Supplementary Figure 2

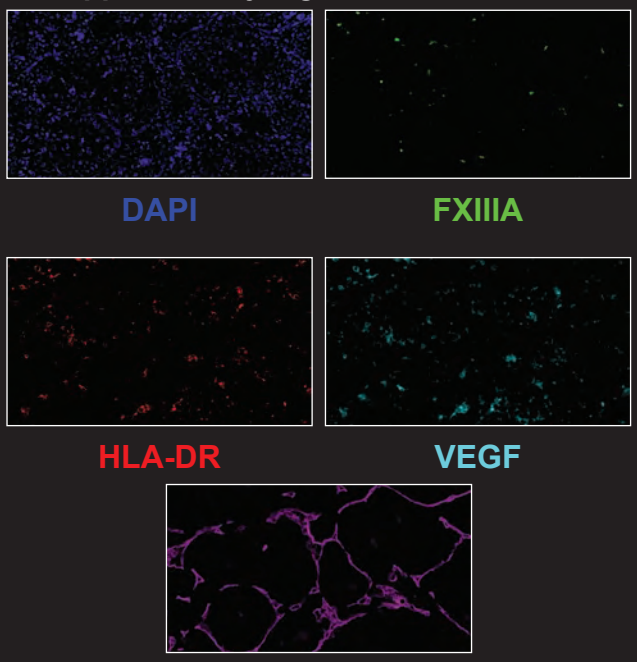

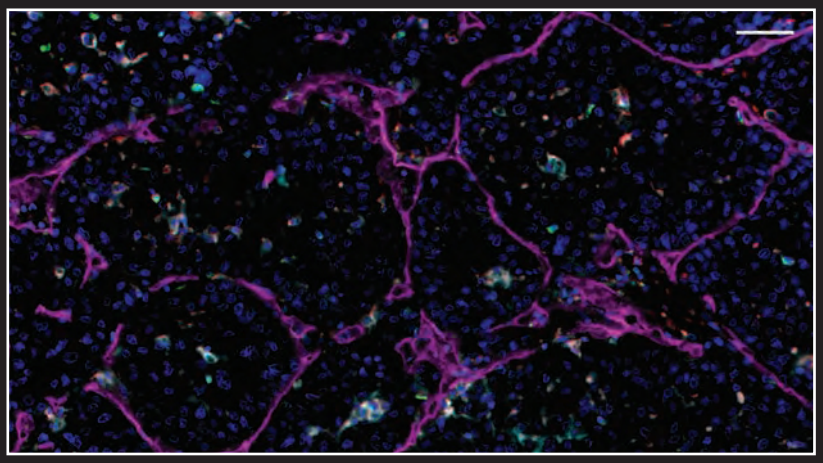

Supplementary Figure 3

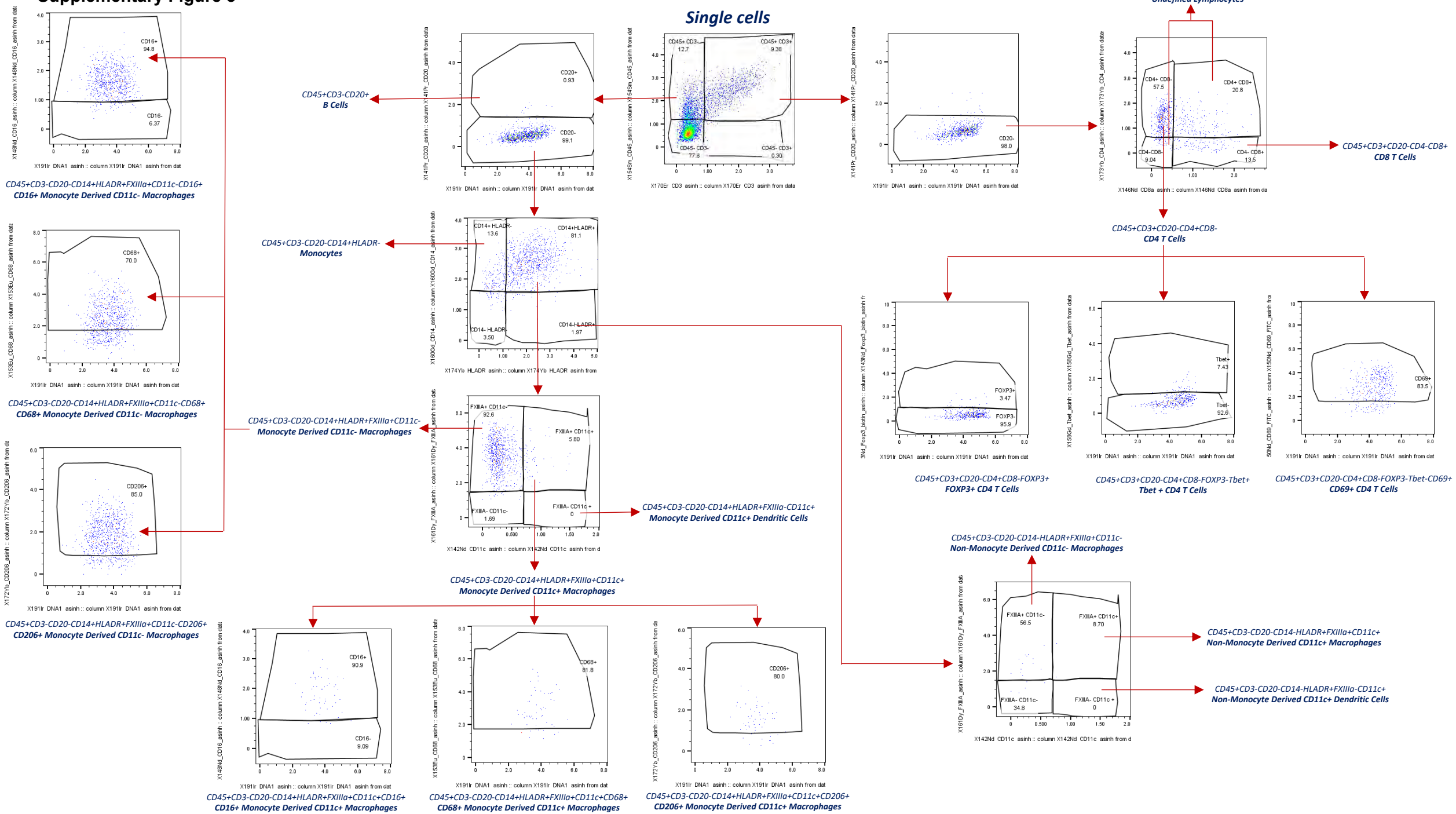

Supplementary Figure 4

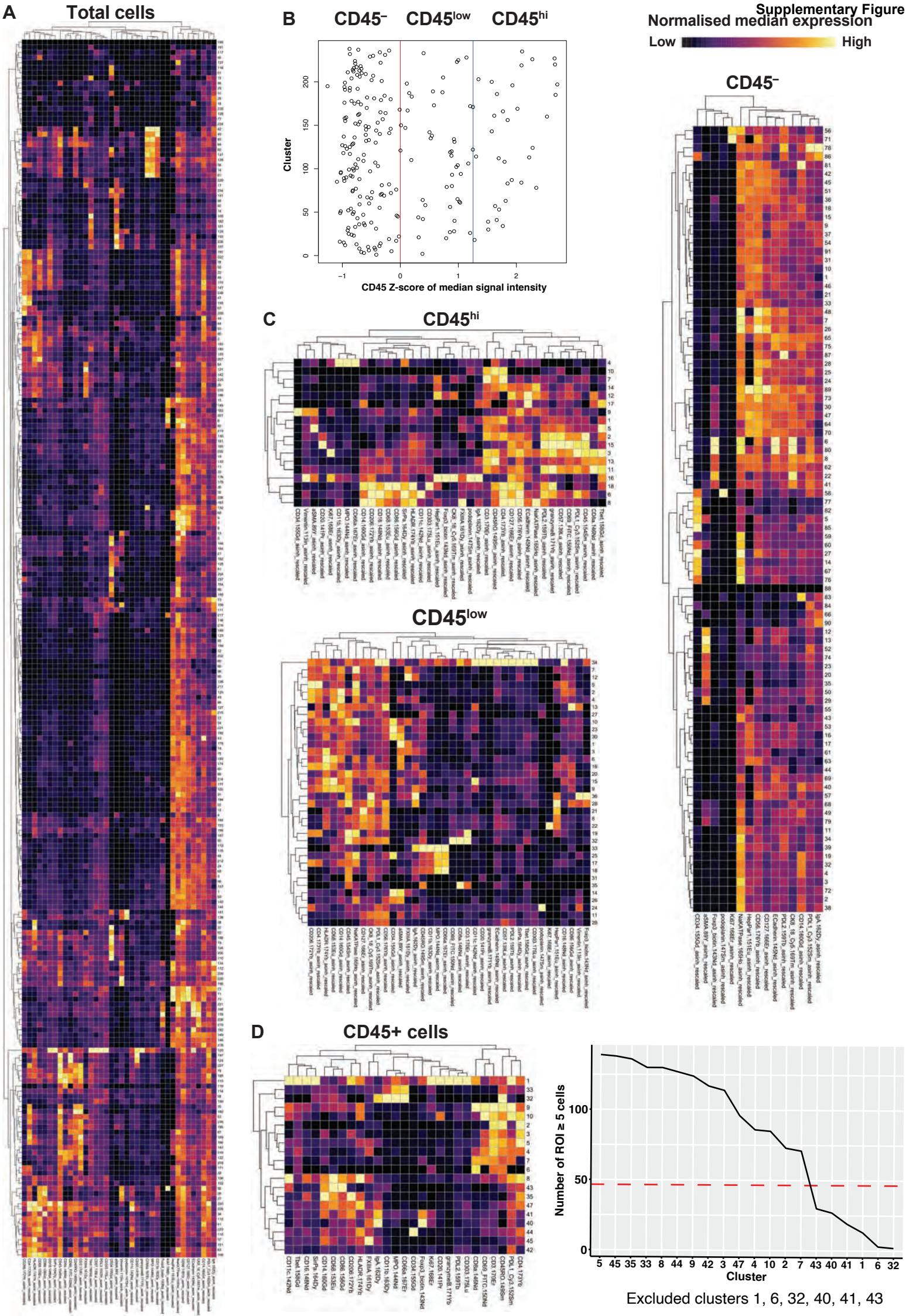

Supplementary Figure 5

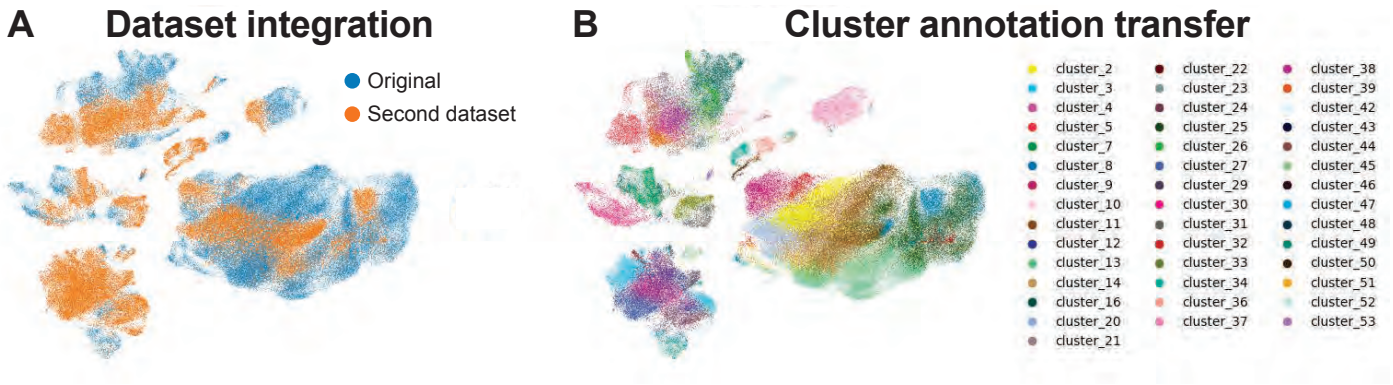

Supplementary Figure 6

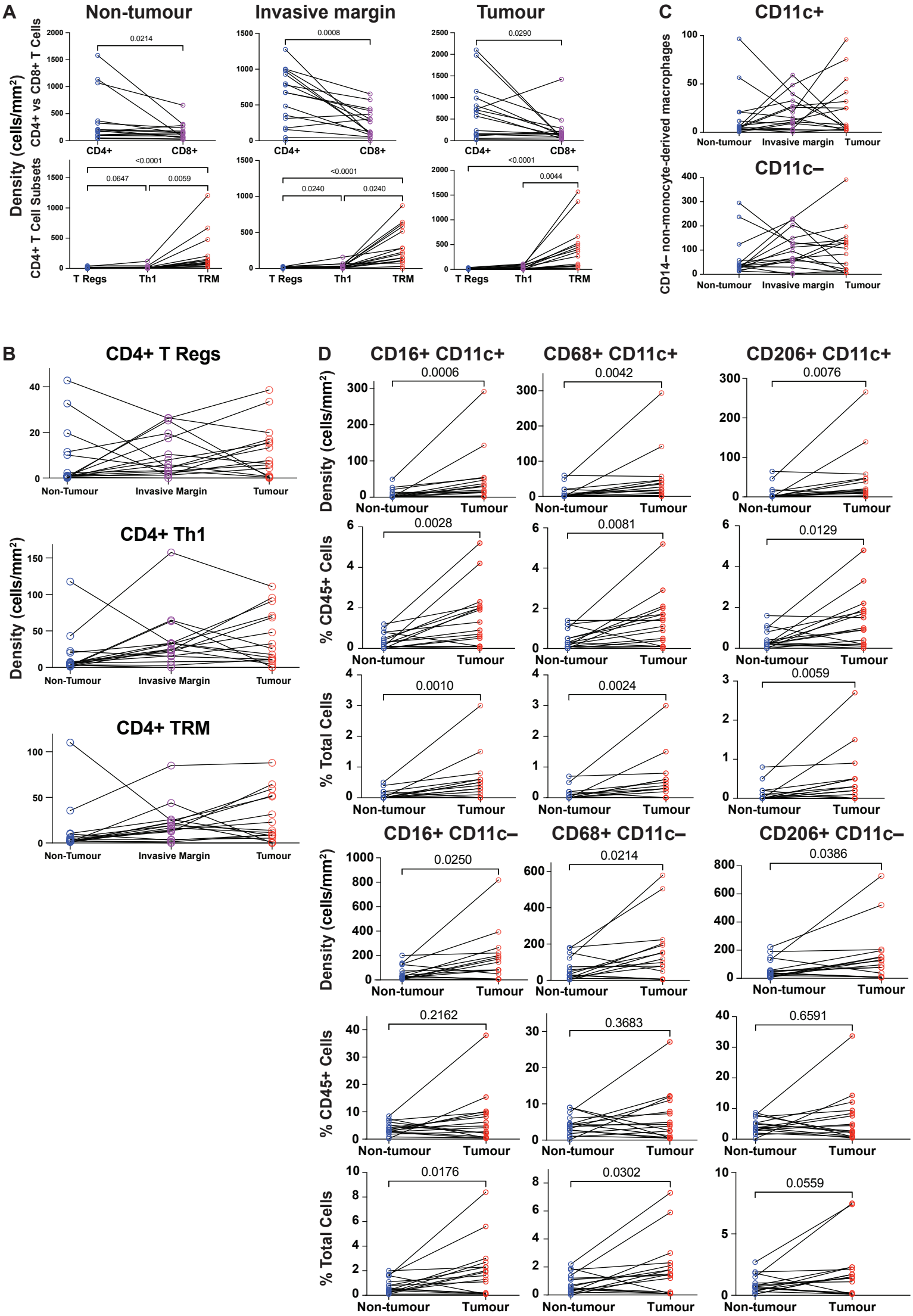

Supplementary Figure 7

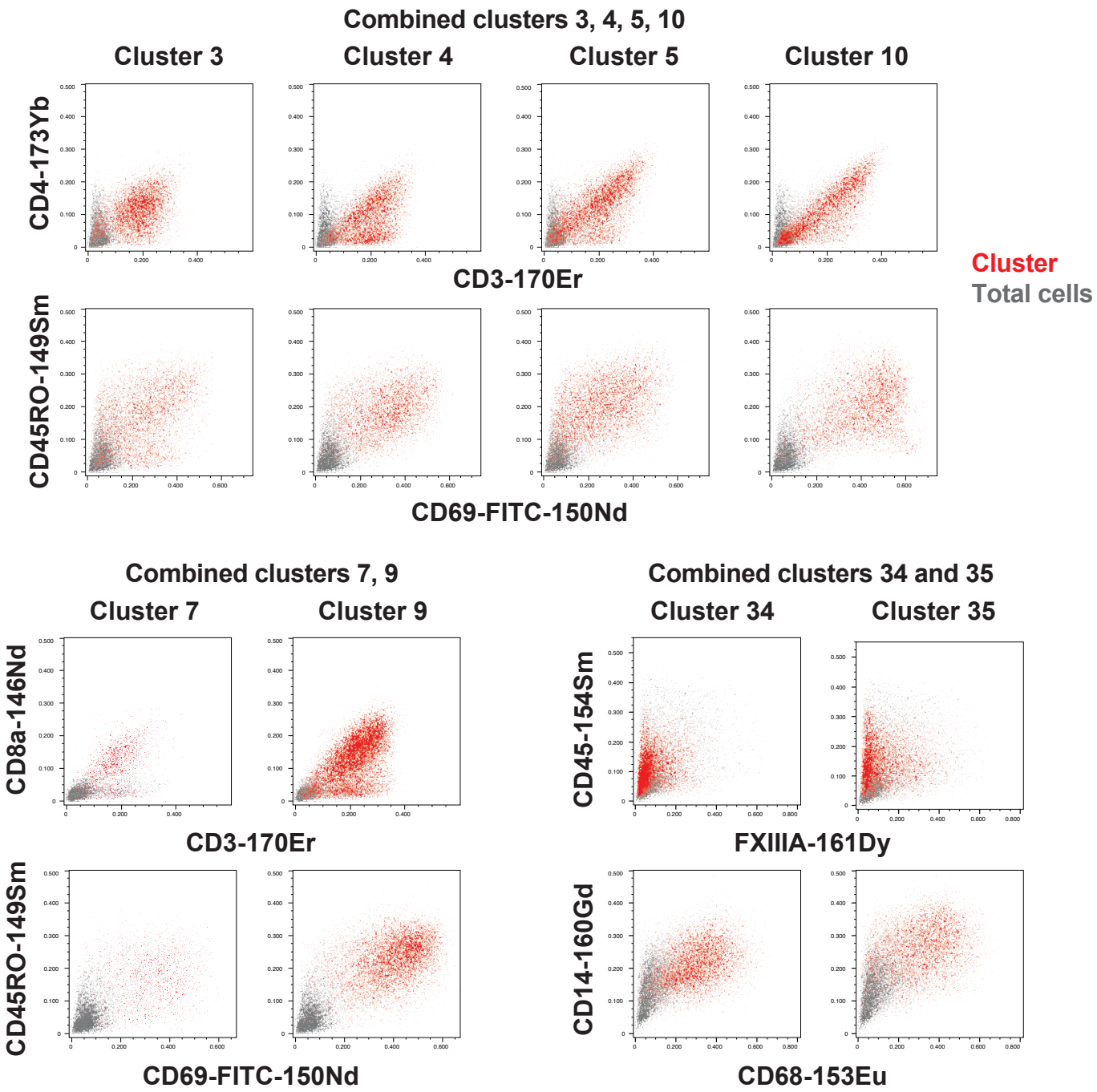

Supplementary Figure 5 (page 1/7)

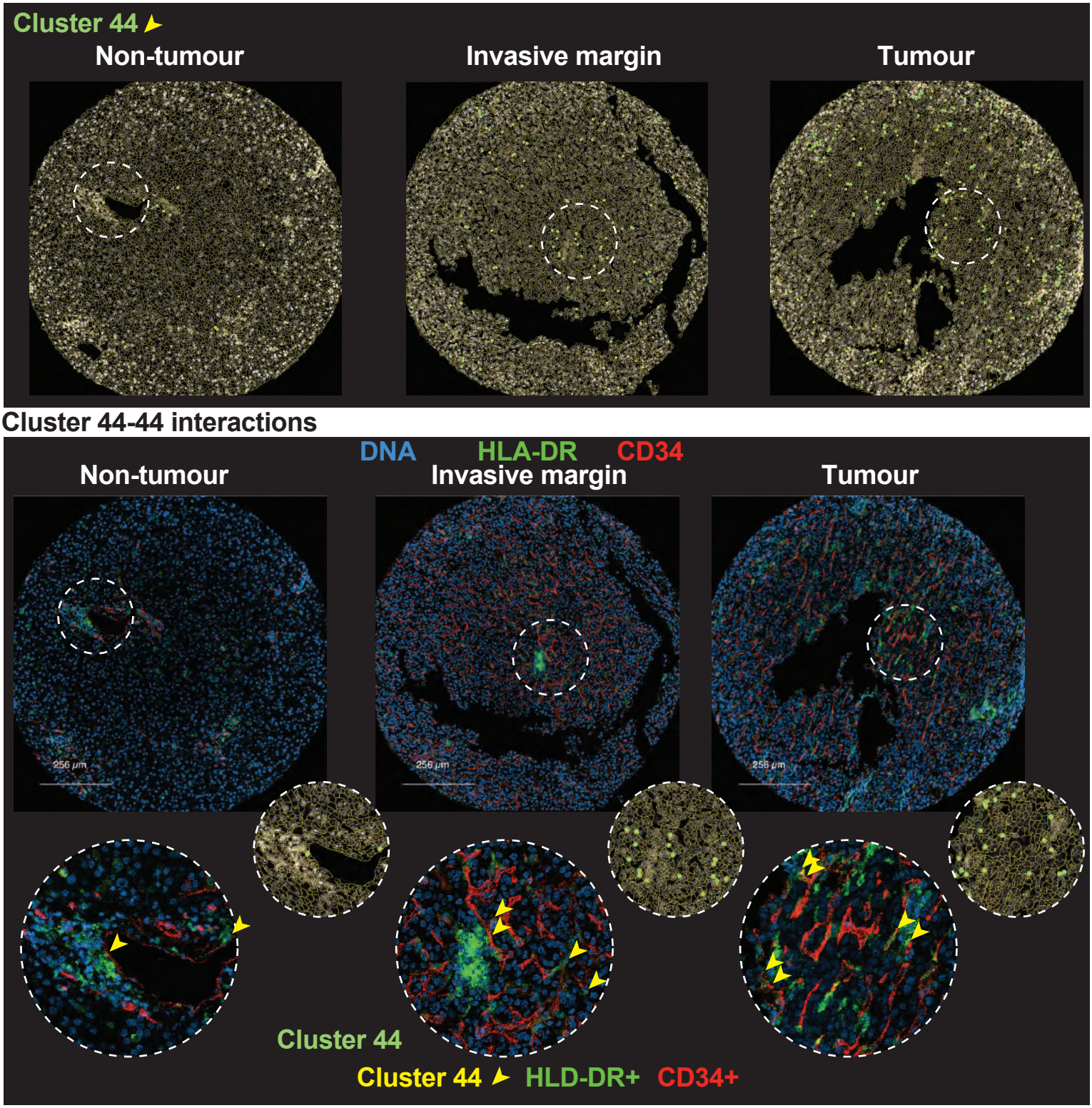

Supplementary Figure 5 (page 2/7)

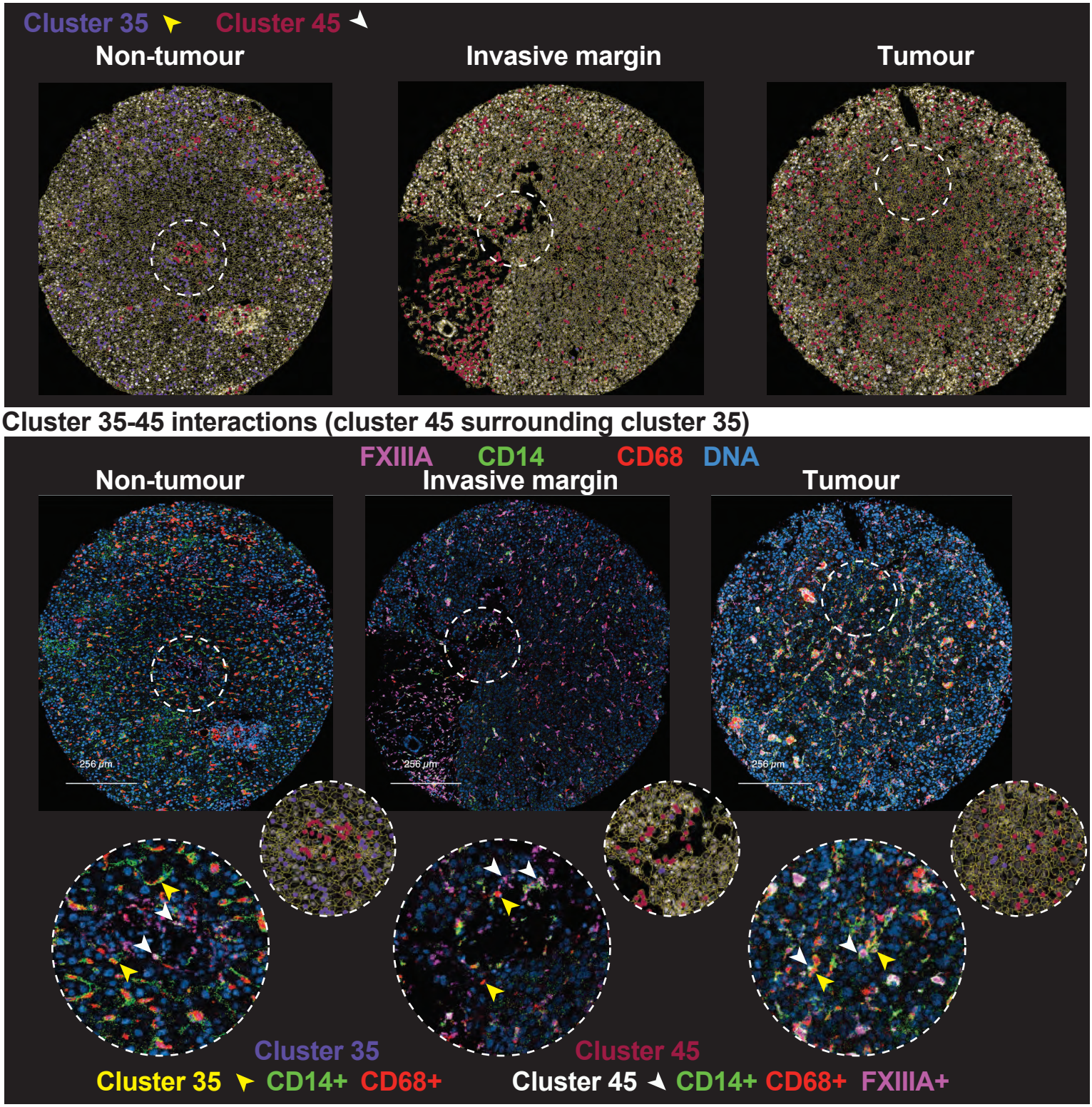

Supplementary Figure 5 (page 3/7)

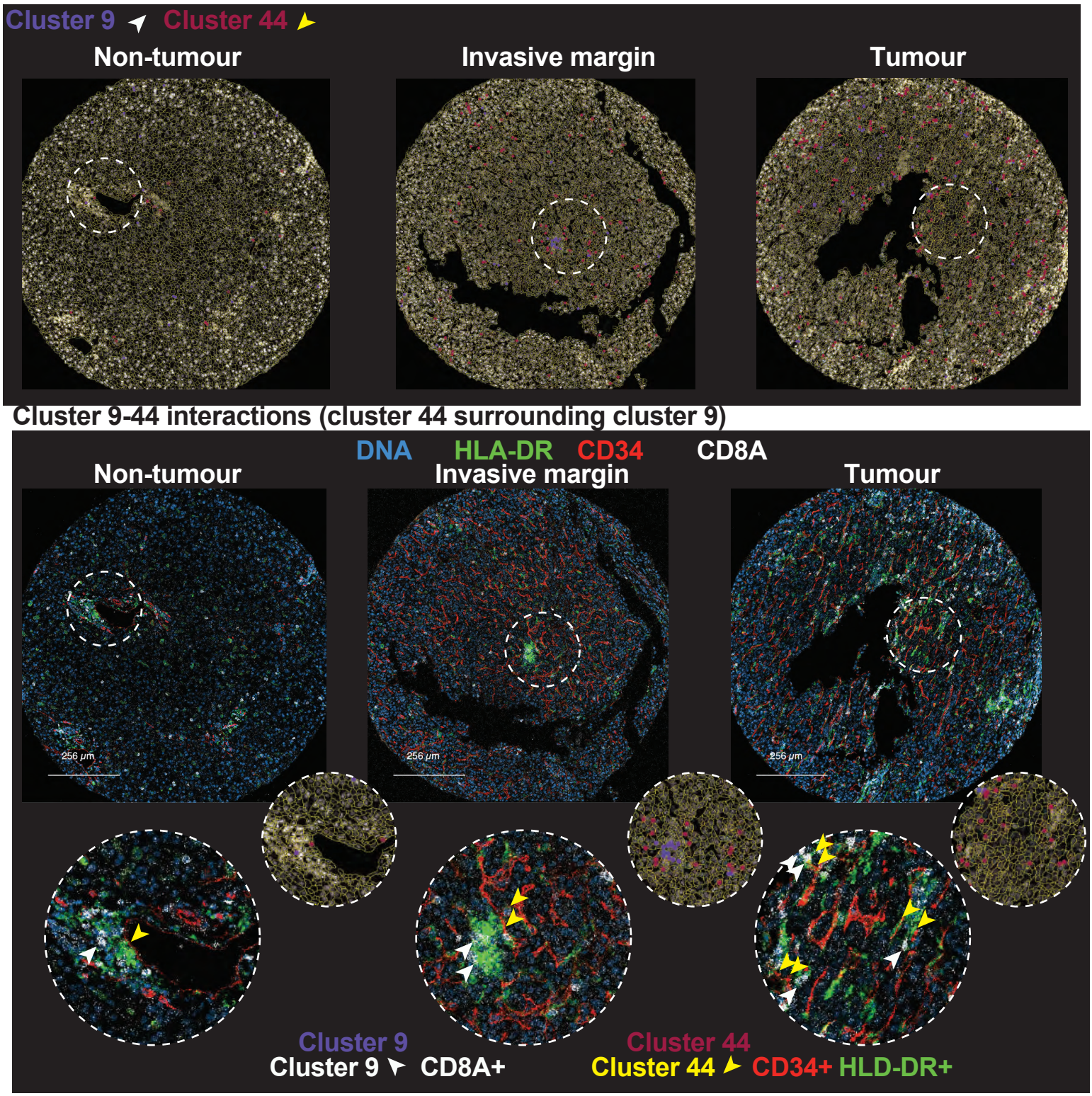

Supplementary Figure 5 (page 4/7)

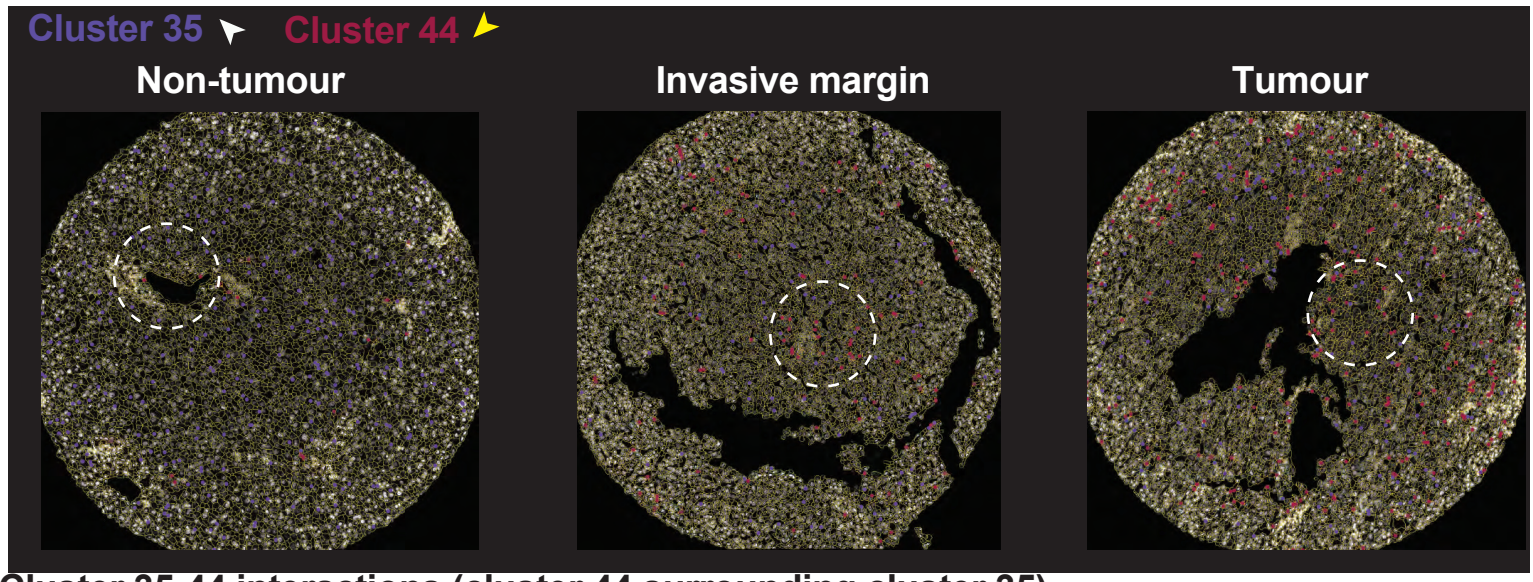

Cluster 35-44 interactions (cluster 44 surrounding cluster 35)

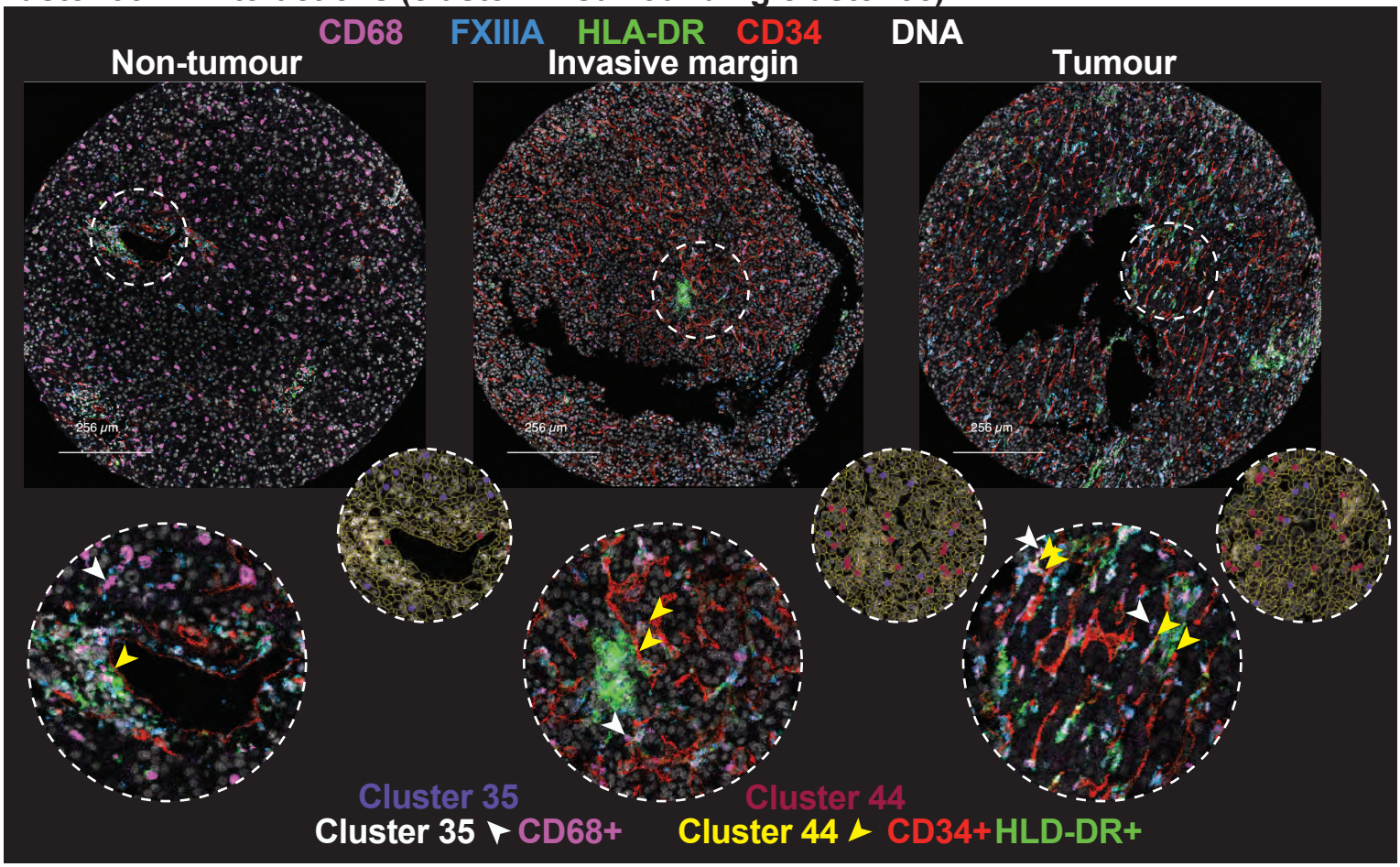

Supplementary Figure 5 (page 5/7)

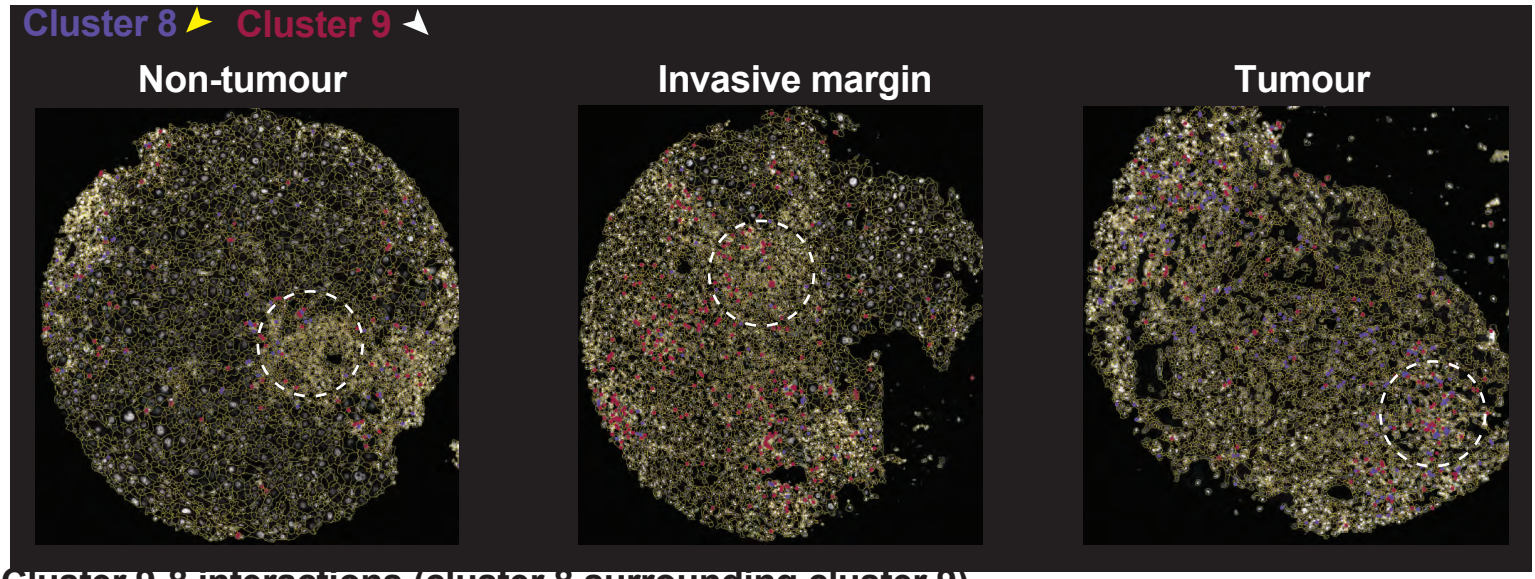

Cluster 9-8 interactions (cluster 8 surrounding cluster 9)

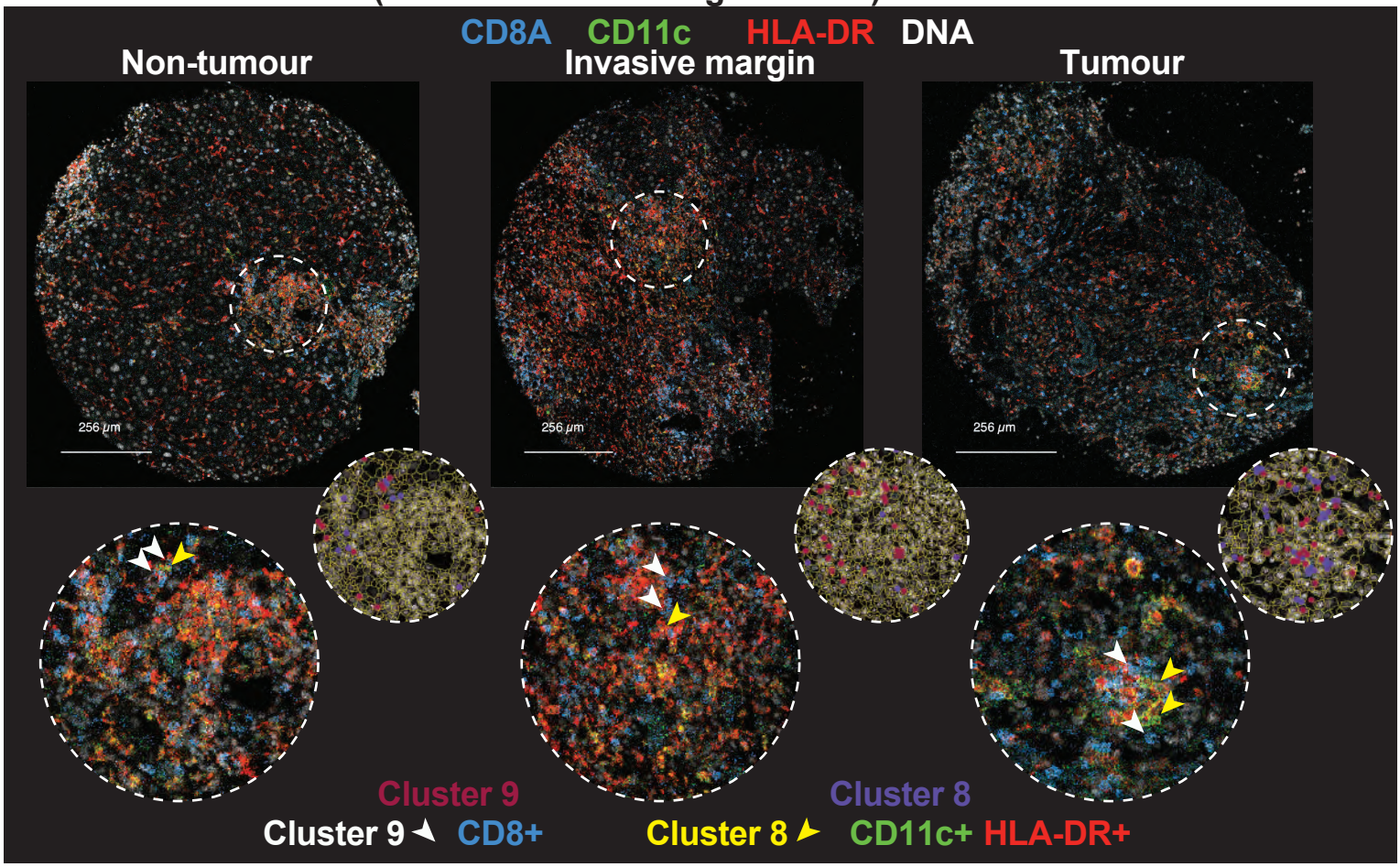

Supplementary Figure 5 (page 6/7)

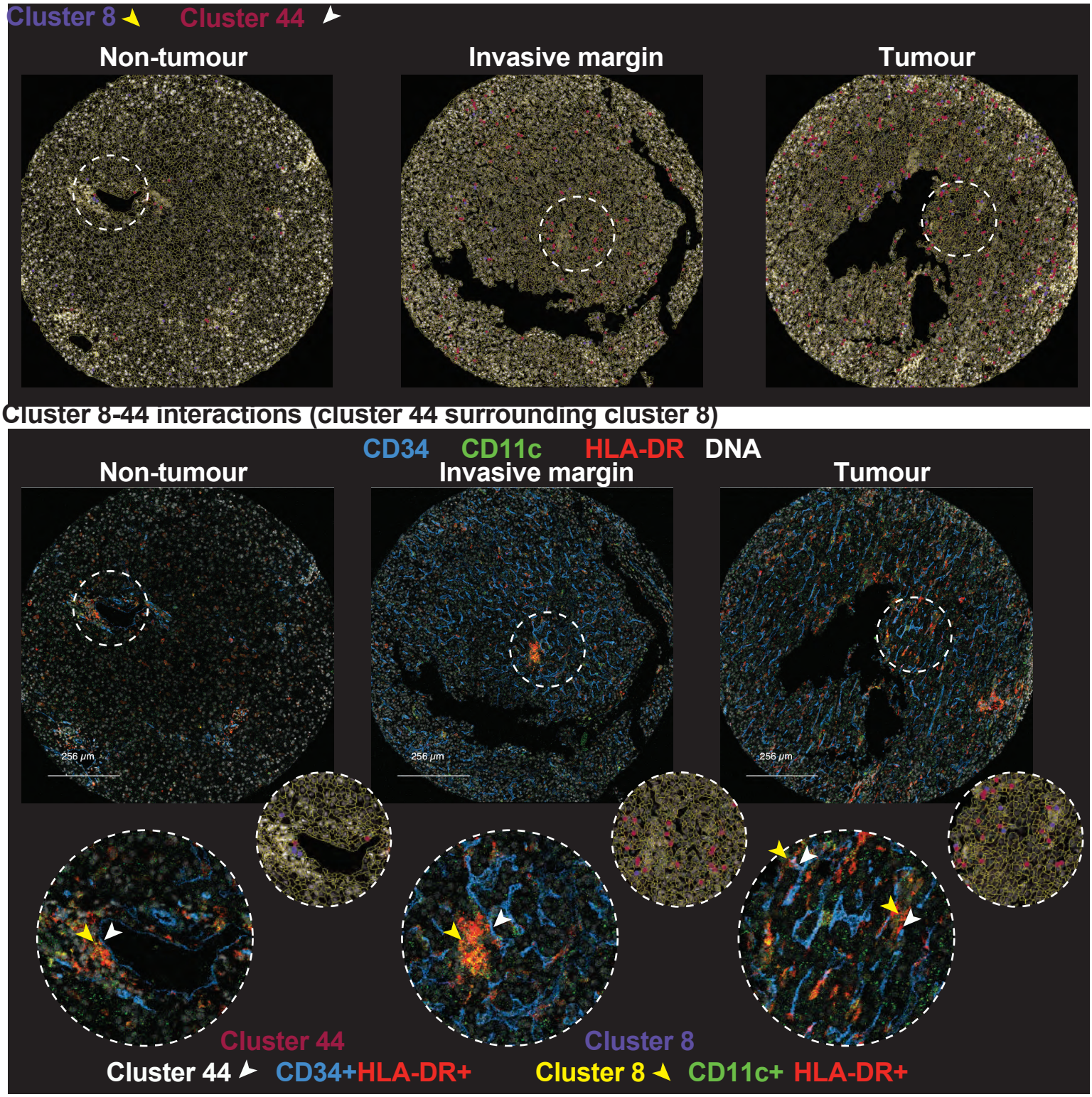

Supplementary Figure 5 (page 7/7)

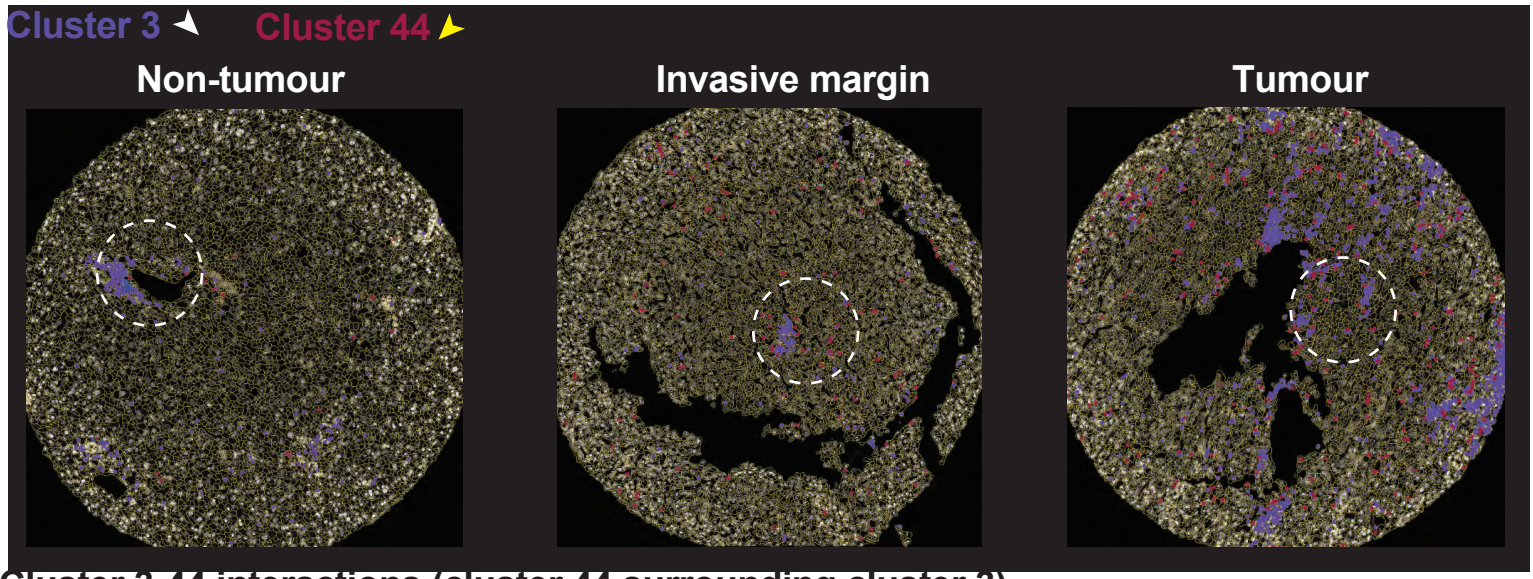

Cluster 3-44 interactions (cluster 44 surrounding cluster 3)

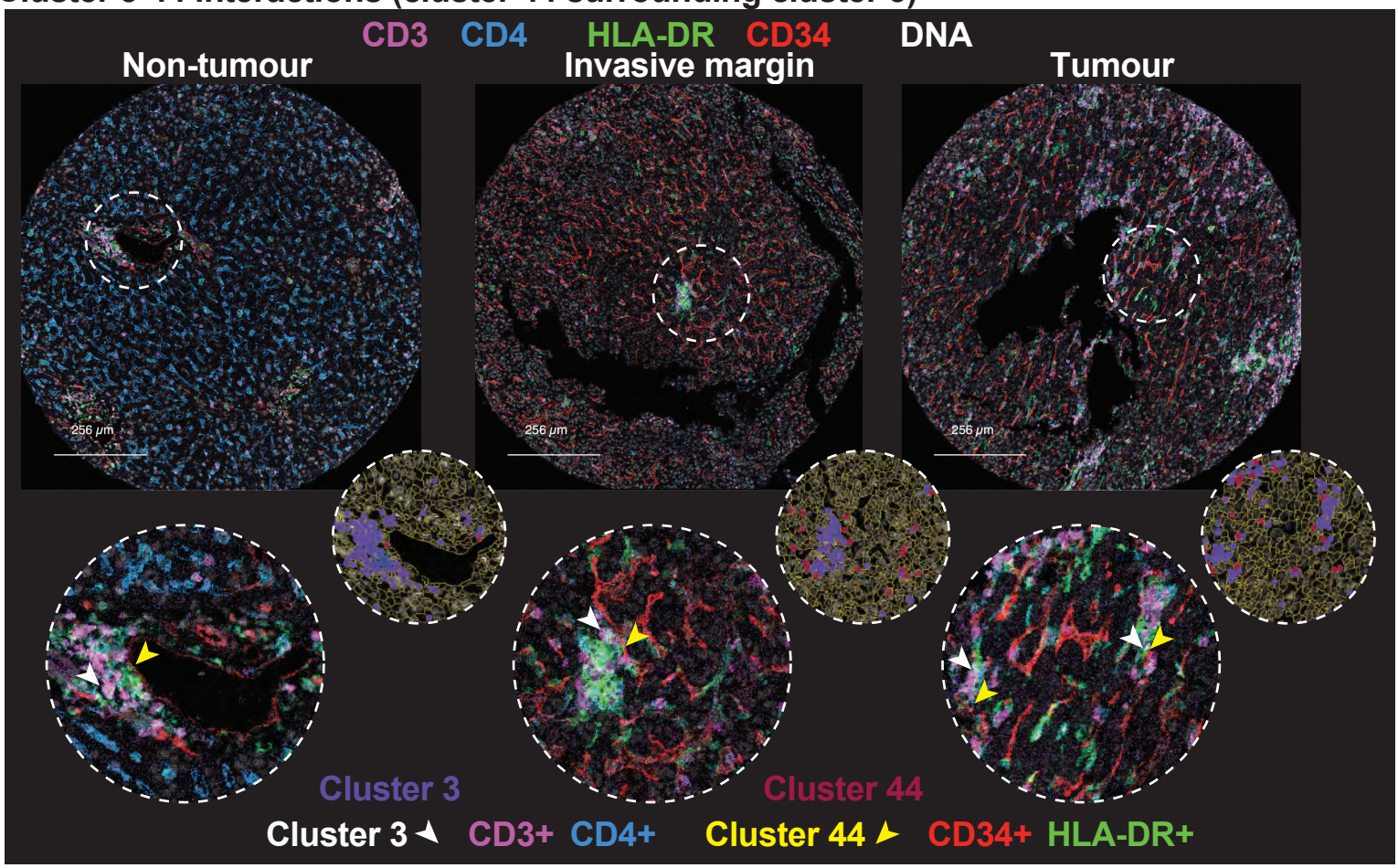

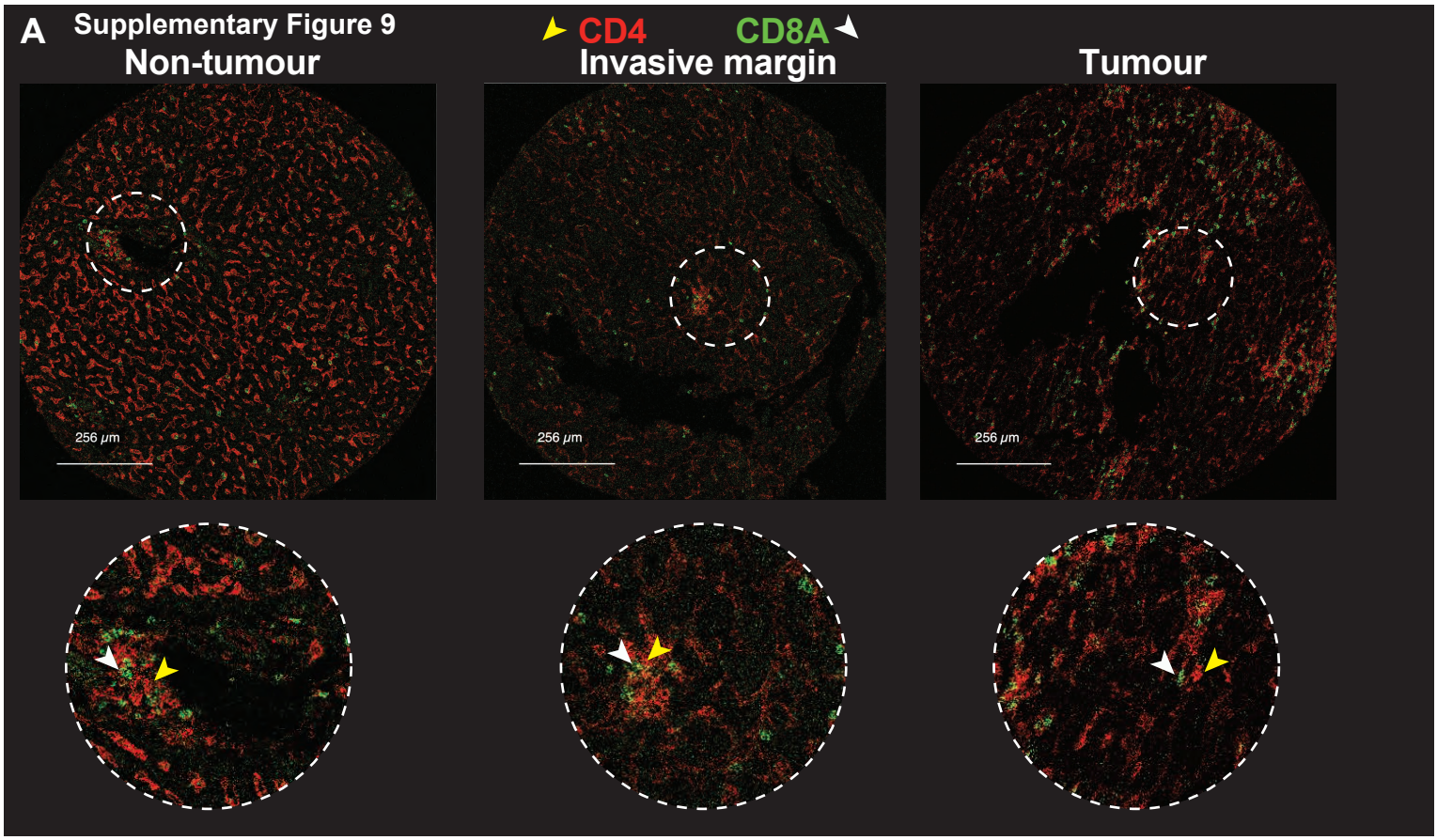

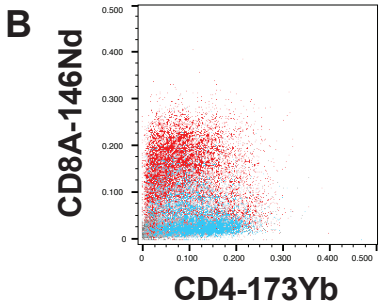

Cluster 3 (CD4+ T cells) Cluster 9 (CD8+ T cells) Total cells

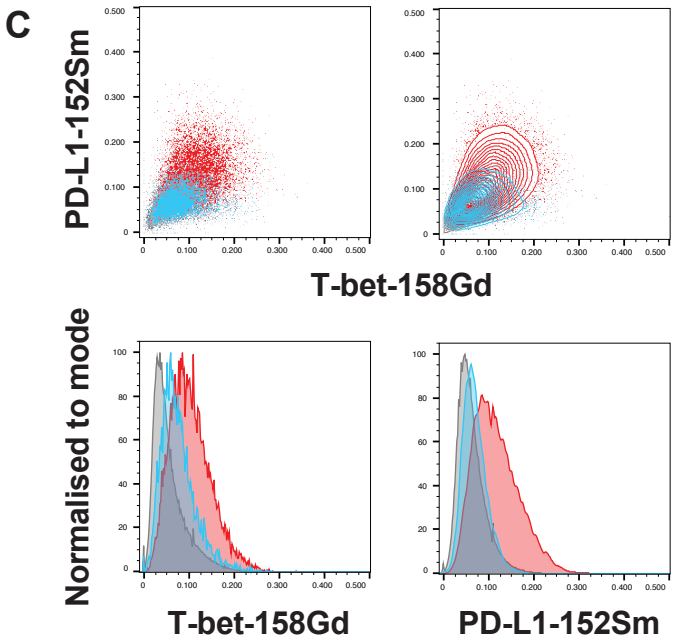

Supplementary Figure 10

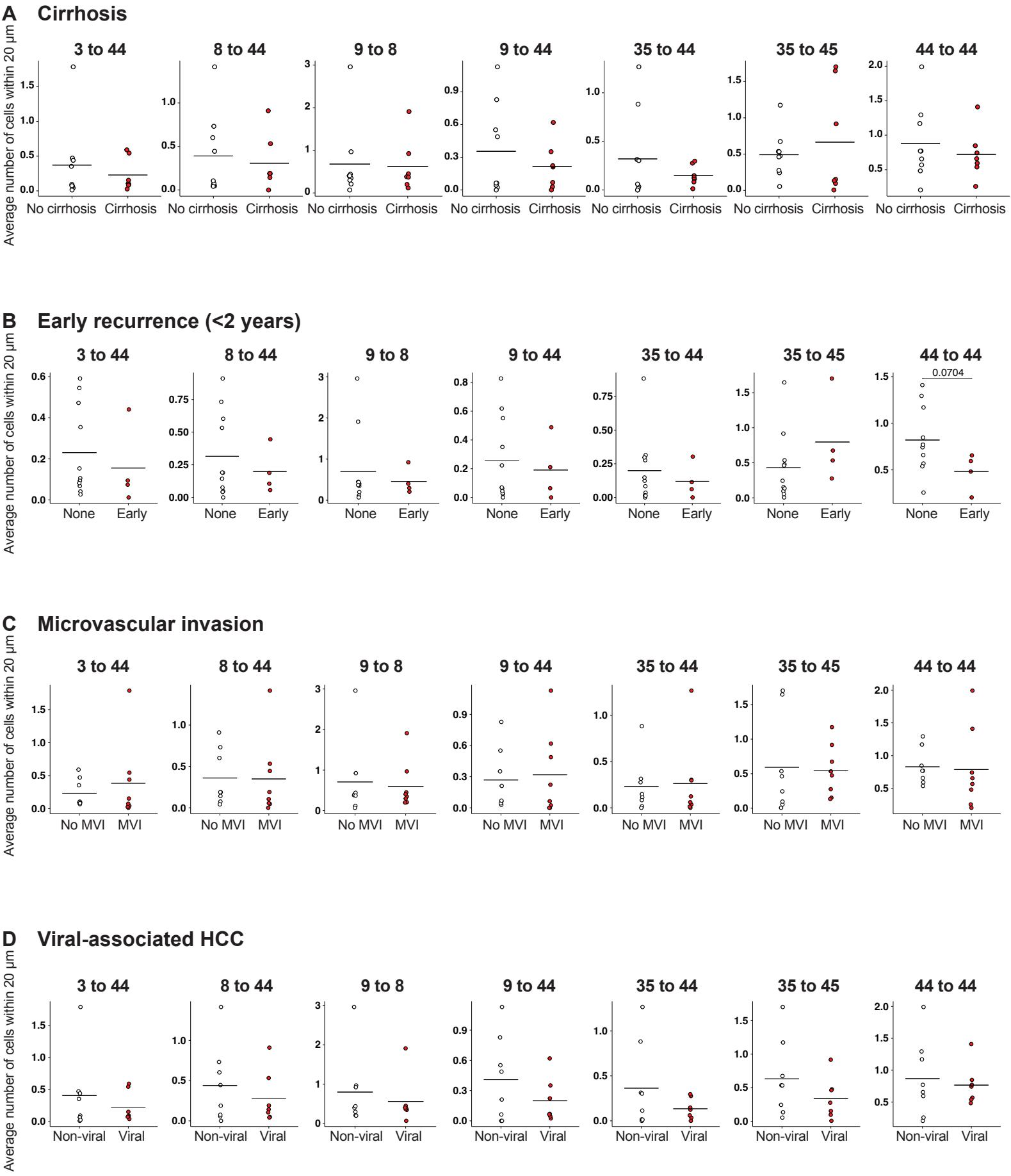

Supplemenary Table 1: Patient cohort

ID	Experiment	Aetiology	Cirrhotic	BCLC	TNM	Largest tumour size (mm)	Tumour number	MVI	Differentiation	Previous Tx
1	IMC (TMA1)	HBV	Y	A	pT2	17	2	Y	Moderate	N
2	IMC (TMA1)	MASH	N	A	pT2	165	1	Y	Moderate	N
3	IMC (TMA1)	HBV	Y	A	pT1	40	2	N	Well	N
4	IMC (TMA1)	HCV, MASH	Y	A	pT1b	32	1	N	Poor	N
5	IMC (TMA1)	ALD	Y	A	T1bN0MX	35	1	N	Moderate	N
6	IMC (TMA1)	MASH	N	A	pT1b	37	1	N	Moderate	N
7	IMC (TMA1)	MASH	N	A	pT3	270	1	Y	Moderate	N
8	IMC (TMA1)	HBV	N	A	pT2	117	1	Y	Well to moderate	N
9	IMC (TMA2)	HCV	Y	A	pT2	30	1	Y	Moderate	N
10	IMC (TMA2)	HCV	N	A	pT2 Nx	170	1	Y	Moderate	N
11	IMC (TMA2)	ALD	Y	A	pT2	25	1	Y	Well to moderate	N
12	IMC (TMA2)	Unknown	N	B	T3 N0 M0	110	>3	Y	Moderate	N
13	IMC (TMA2)	HCV	Y	A	pT2	21	1	N	Well to moderate	N
14	IMC (TMA2)	HBV	N	A	pT1a	16	1	N	Moderate	N
15	IMC (TMA2)	MASH, ALD	N	A	pT1a	9	1	N	Well	N
16	IMC (TMA2)	Unknown	N	A	pT1b N0	140	1	N	Poor	N
17	OPAL	HBV	N	A	pT1b N0M0	150	1	Y	Moderate	N
18	OPAL	Unknown	Y	A	pT1b N0M0	120	1	N	Well	TACE
19	OPAL	ALD	N	A	pT2 N0M0	130	1	Y	Moderate	N
20	OPAL	HCV, ALD	Y	B	pT2 N0M0	45 + 18	2	N	Moderate	N
21	OPAL	Unknown	N	A	pT2 N0M0	160	1	Y	Poor	Atezolizumab
22	OPAL	HCV	N	A	pT4 N1 M0	45	1	Y	Poor	N
23	OPAL	Unknown	N	A	pT2 N0M0	180	1	Y	Moderate	N
24	OPAL	HBV	N	A	pT1b N0M0	71	1	N	Moderate	N

Supplementary Table 2: Imaging mass cytometry antibody panel

Metal	Marker	Clone	Species isotype	Company	Concentration
89Y	a-SMA	1A4	Mouse IgG2a	R&D Systems	1 μg mL^{-1}
113In	Vimentin	D21H3	Rabbit IgG	CST	1 μg mL^{-1}
139La	CD57	HNK-1	Mouse IgM	BD Biosciences	2 μg mL^{-1}
141Pr	CD20	H1	Mouse IgG2a	BD Biosciences	4 μg mL^{-1}
142Nd	CD11c	EP1347Y	Rabbit IgG	Abcam	2 μg mL^{-1}
143Nd	Foxp3-biotin	236A/E7	Mouse IgG1	eBioscience	10 μg mL^{-1}
	Anti-biotin	1D4-C5	Mouse IgG2a	DVS	1/100 dilution
144Nd	MPO	E1E7l	Rabbit IgG	CST	8 μg mL^{-1}
145Nd	E-cadherin	36/E-cadherin	Mouse IgG2a	BD Biosciences	4 μg mL^{-1}
146Nd	CD8a	D8A8Y	Rabbit IgG	CST	1.98 μg mL^{-1}
147Sm	Podoplanin	polyclonal (cat #AF3670, batch #XXO0219081)	Sheep IgG	R&D Systems	2 μg mL^{-1}
148Nd	CD16	EPR16784	Rabbit IgG	Abcam	8 μg mL^{-1}
149Sm	CD45RO	UCHL1	Mouse IgG2a	BioLegend	4 μg mL^{-1}
150Nd	CD69	EPR21814	Rabbit IgG	Abcam	0.986 μg mL^{-1}
	Anti-FITC	FIT-22	Mouse IgG1	BioLegend	4 μg mL^{-1}
151Eu	HepPar1*	OCH1E5	Mouse IgG1	Santa Cruz	2 μg mL^{-1}
152Sm	PD-L1	E1L3N	Rabbit IgG	CST	1/2000 dilution
	Cy3-donkey anti-rabbit	polyclonal (code 711-166-152, lot 122096)	Donkey IgG	Jackson ImmunResearch Laboratories	1/100 dilution
	Anti-Cy3	A-6	Mouse IgG1	Santa Cruz	4 μg mL^{-1}
153Eu	CD68	KP1	Mouse IgG1	BioLegend	2 μg mL^{-1}
154Sm	CD45	D9M8I	Rabbit IgG	Cell Signalling	3 μg mL^{-1}
155Gd	CD34*	QBend10	Mouse IgG1	Novus Biologicals	2 μg mL^{-1}
156Gd	CD86	polyclonal (cat #AF141NA)	Goat IgG	R&D Systems	2 μg mL^{-1}

158Gd	T-bet	D6N8B	Rabbit IgG	CST	6 μg mL^{-1}
159Tb	PD-L2*	D7U8C	Rabbit IgG	CST	50 μg mL^{-1}
160Gd	CD14	EPR3653	Rabbit IgG	Abcam	1 μg mL^{-1}
161Dy	FXIIIa	polyclonal (cat #SAF13A-AP, batch #AP1625-AR1)	Sheep IgG	Affinity Biologicals	2 μg mL^{-1}
162Dy	IgA*	3A5A5	Mouse IgG1	Proteintech	0.2 μg mL^{-1}
163Dy	CD11b	EPR1344	Rabbit IgG	Abcam	4 μg mL^{-1}
164Dy	SirPa	D6I3M	Rabbit IgG	Cell Signalling	4 μg mL^{-1}
165Ho	NaKATPase	EP1845Y	Rabbit IgG	Abcam	6 μg mL^{-1}
166Er	CD127	EPR2955(2)	Rabbit IgG	Abcam	4 μg mL^{-1}
167Er	CD66a	YTH71.3	Rat IgG2a	Abcam	4 μg mL^{-1}
168Er	Ki67	B56	Mouse IgG1	BD Biosciences	4 μg mL^{-1}
169Tm	CK8/18	5D3	Mouse IgG1	Leica	1/200 dilution
	AF647-donkey anti-mouse	polyclonal (code 715-606-150, lot 121469)	Donkey $F(ab')_2$ fragment	Jackson ImmunResearch Laboratories	1/100 dilution
	Anti-AF647/Cy5	CY5-15	Mouse IgG1	Sigma	4 μg mL^{-1}
170Er	CD3	polyclonal (cat #A045229-2)	Rabbit	Dako	4 μg mL^{-1}
171Yb	granzyme B	EPR8260	Rabbit IgG	Abcam	8 μg mL^{-1}
172Yb	CD206	685645	Mouse IgG2b	R&D Systems	4 μg mL^{-1}
173Yb	CD4	EPR6855	Rabbit IgG	Abcam	1 μg mL^{-1}
174Yb	HLA-DR	EPR3692	Rabbit IgG	Abcam	1 μg mL^{-1}
175Lu	CD303/BDCA2	polyclonal (cat #55427-1-AP)	Goat IgG	R&D Systems	4 μg mL^{-1}
176Yb	CD56	EPR2566	Rabbit IgG	Abcam	4 μg mL^{-1}
209Bi	DC-SIGN	polyclonal (cat # ab5715)	Rabbit IgG	Abcam	1.05 μg mL^{-1}

*Antibodies conjugated and titrated by our group. All others were conjugated by Sydney Cytometry or bought directly conjugated from Standard BioTools.